AD-A094 422 PENNSYLVANIA STATE UNIV UNIVERSITY PARK APPLIED RESE--ETC F/G 20/4
EXPERIMENTAL VERIFICATION OF THE STREAMLINE CURVATURE NUMERICAL--ETC(U)
MAY 80 M J PIERZGA N00024-79-C-6043
UNCLASSIFIED ARL/PSU/TM-80-181 NL

1 OF 3
AD A
094422

LEVEL

AD A094422

EXPERIMENTAL VERIFICATION OF THE STREAMLINE CURVATURE NUMERICAL ANALYSIS METHOD APPLIED TO THE FLOW THROUGH AN AXIAL FLOW FAN

M. J. Pierzga

Technical Memorandum
File No. 80-181
May 28, 1980
Contract No. N00024-79-C-6043

Copy No. 10

The Pennsylvania State University
APPLIED RESEARCH LABORATORY
Post Office Box 30
State College, PA 16801

NAVY DEPARTMENT

NAVAL SEA SYSTEMS COMMAND

SECURITY CLASSIFICATION OF THIS PAGE (When Data Entered)

REPORT DOCUMENTATION PAGE	READ INSTRUCTIONS BEFORE COMPLETING FORM
1. REPORT NUMBER: 80-181 / 2. GOVT ACCESSION NO.: AD A094422	3. RECIPIENT'S CATALOG NUMBER:
4. TITLE (and Subtitle): EXPERIMENTAL VERIFICATION OF THE STREAMLINE CURVATURE NUMERICAL ANALYSIS METHOD APPLIED TO THE FLOW THROUGH AN AXIAL FLOW FAN	5. TYPE OF REPORT & PERIOD COVERED: Technical Memorandum 6. PERFORMING ORG. REPORT NUMBER:
7. AUTHOR(s): M. J. Pierzga	8. CONTRACT OR GRANT NUMBER(s): N00024-79-C-6043
9. PERFORMING ORGANIZATION NAME AND ADDRESS: Applied Research Laboratory, Post Office Box 30, State College, PA 16801	10. PROGRAM ELEMENT, PROJECT, TASK AREA & WORK UNIT NUMBERS:
11. CONTROLLING OFFICE NAME AND ADDRESS: Naval Sea Systems Command, Department of the Navy, Washington, DC 20362	12. REPORT DATE: May 28, 1980 13. NUMBER OF PAGES: 234
14. MONITORING AGENCY NAME & ADDRESS (if different from Controlling Office)	15. SECURITY CLASS. (of this report): UNCLASSIFIED 15a. DECLASSIFICATION/DOWNGRADING SCHEDULE:

16. DISTRIBUTION STATEMENT (of this Report)

Approved for public release. Distribution unlimited. Per NAVSEA - Oct. 2, 1980.

Accession For	
NTIS GRA&I	☒
DTIC TAB	☐
Unannounced	☐
Justification	
By	
Distribution/	
Availability Codes	
Dist	Avail and/or Special
A	

17. DISTRIBUTION STATEMENT (of the abstract entered in Block 20, if different from Report)

18. SUPPLEMENTARY NOTES

19. KEY WORDS (Continue on reverse side if necessary and identify by block number)

thesis, axial flow fan, streamline, curvature, numerical, analysis

20. ABSTRACT (Continue on reverse side if necessary and identify by block number)

To verify the results of a streamline curvature numerical analysis method, an investigation has been conducted in which comparisons are made between analytical and experimental data of an axial flow fan. Using loss model calculations to determine the proper outlet flow deviation angles, the flow field in the hub-to-tip plane of the turbomachine was calculated. These deviation angle calculations allow the inviscid streamline curvature (SLC) analysis to model a real fluid with viscous losses. The verification of this calculated flow field is the primary objective of the investigation; however,

DD FORM 1 JAN 73 1473 EDITION OF 1 NOV 65 IS OBSOLETE

SECURITY CLASSIFICATION OF THIS PAGE (When Data Entered)

in addition to the hub-to-tip flow field, the numerical analysis of the blade-to-blade flow field was also investigated in some detail.

To verify the accuracy of the numerical results, detailed flow surveys were conducted upstream and downstream of the test rotor of the axial flow fan. To obtain the necessary data to verify the blade-to-blade solutions, internal blade row data were also collected. The internal blade row measurements were obtained by using a rotating circumferential traversing mechanism which was designed and implemented during this investigation. Along with these two sets of survey data, the static pressure distributions on the pressure and suction surfaces of the test rotor were also obtained. The combination of these experimental data defines the flow field throughout the entire machine which was investigated.

Comparison of the SLC hub-to-tip solution with test data shows that, for the test rotor operating at its design mass flow condition, the numerical analysis predicts the outlet flow field to within a few percent of the measured data. The analyses performed to obtain the surface static pressure distributions on the rotor blades also agree quite well with measured profiles.

ABSTRACT

To verify the results of a streamline curvature numerical analysis method, an investigation has been conducted in which comparisons are made between analytical and experimental data of an axial flow fan. Using loss model calculations to determine the proper outlet flow deviation angles, the flow field in the hub-to-tip plane of the turbomachine was calculated. These deviation angle calculations allow the inviscid streamline curvature (SLC) analysis to model a real fluid with viscous losses. The verification of this calculated flow field is the primary objective of the investigation; however, in addition to the hub-to-tip flow field, the numerical analysis of the blade-to-blade flow field was also investigated in some detail.

To verify the accuracy of the numerical results, detailed flow surveys were conducted upstream and downstream of the test rotor of the axial flow fan. To obtain the necessary data to verify the blade-to-blade solutions, internal blade row data were also collected. The internal blade row measurements were obtained by using a rotating circumferential traversing mechanism which was designed and implemented during this investigation. Along with these two sets of survey data, the static pressure distributions on the pressure and suction surfaces of the test rotor were also obtained. The combination of these experimental data defines the flow field throughout the entire machine which was investigated.

Comparison of the SLC hub-to-tip solution with test data shows that, for the test rotor operating at its design mass flow condition,

the numerical analysis predicts the outlet flow field to within a few percent of the measured data. The analyses performed to obtain the surface static pressure distributions on the rotor blades also agree quite well with measured profiles.

TABLE OF CONTENTS

TABLE OF CONTENTS (Continued)

LIST OF TABLES

LIST OF FIGURES

LIST OF FIGURES (Continued)

LIST OF FIGURES (Continued)

LIST OF FIGURES (Continued)

LIST OF FIGURES (Continued)

LIST OF FIGURES (Continued)

LIST OF FIGURES (Continued)

LIST OF SYMBOLS

Symbol	Definition
a	distance from leading edge to point of maximum camber along chord line
ar	tip vortex core radius
AVR	axial velocity ratio (V_{X_2}/V_{X_1})
c	chord length
C_{L_T}	tip lift coefficient
CP	static pressure coefficient $\left\{1 - \left(\frac{V_{LOCAL}}{V_\infty}\right)^2\right\}$
CP_P	pitch coefficient
CP_S	static pressure coefficient
CP_T	total pressure coefficient
CP_Y	yaw coefficient
d	longitudinal distance from leading edge to tip vortex calculation point
G	distance from chord line to maximum camber point
K	cascade influence coefficient
$(K_\delta)_{sh}$	correction for blade shapes with different thickness distributions than 65-series
$(K_\delta)_t$	correction of blade thickness other than 10 percent
m	slope factor
M_R	radial momentum
P	static pressure
P_{MEAS}	measured static pressure on blade surface
$P_{ROTATION}$	correction for static pressure readings due to rotational effects
P_{TRUE}	corrected static pressure on blade surface

LIST OF SYMBOLS (Continued)

Symbol	Definition
R	radial position of flow boundary
r	local tip vortex radius
R_C	radius of curvature
Re	Reynolds number $\left(\rho \frac{V_\infty D_{probe}}{\mu}\right)$
R_{TIP}	radius of rotor tip
S	blade spacing
S_1	blade-to-blade streamsurface
S_2	hub-to-tip streamsurface
t	blade maximum thickness
U	rotor wheel speed (ωr)
U_m	rotor wheel speed at mean radius
U_{TIP}	rotor wheel speed at rotor tip
V	total velocity
V_M	meridional velocity
V_R	radial velocity
V_θ	tangential velocity
V_x	axial velocity
W_1	relative inlet velocity
W_2	relative exit velocity
x	axial position
y	distance from outer casing
α	angle of attack ($\beta_1 - \lambda$), also indicates pitch angle
α_2	exit absolute flow angle

LIST OF SYMBOLS (Continued)

Symbol	Definition
β	yaw angle
β_1	inlet relative flow angle
β_2	ideal relative exit flow angle (exit blade angle)
β_2^*	actual relative exit flow angle
β_m	mean flow angle $\{(\beta_1 + \beta_2)/2\}$
γ	streamline angle
δ	primary deviation angle
δ'	deviation angle due to axial acceleration effects
δ_H	Howell's deviation angle
δ_0	deviation angle due to camber effects
δ_S	deviation angle due to secondary flow effects
δ_T	deviation angle due to tip leakage effects
δ_{TOT}	total deviation angle
δ^*	deviation angle due to thickness effects
$(\delta_0{}^0)_{10}$	deviation angle for 10 percent thick 65-series thickness distribution
$\Delta\beta$	total turning angle $(\beta_2 - \beta_1)$
ΔR	change in radial position of flow boundary due to periodicity calculation
ΔV_R	change in radial velocity based on periodicity calculation
λ	stagger angle
Φ	angle formed by station line and streamline
Φ'	angle formed by station line and new flow boundaries after periodicity calculation
ϕ	flow coefficient (V_∞/U_{TIP})

LIST OF SYMBOLS (Continued)

Symbol	Definition
ρ	density
θ_c	camber angle
τ	tip clearance
μ	dynamic viscosity
ω_n	normal inlet vorticity
ψ	pressure rise coefficient $\left(\frac{\Delta p}{\frac{1}{2}\rho U^2}\right)$

Direction Vectors

n	normal to streamwise direction
r	radial direction
s	streamwise direction

Subscripts

i	denotes innermost streamline
o	denotes outermost streamline
η	denotes arbitrary station
∞	denotes upstream reference conditions
REF	denotes conditions at reference station

ACKNOWLEDGMENTS

The author wishes to express his sincere thanks and deep felt gratitude to Dr. Robert E. Henderson for his helpful advice and inspiration throughout the course of this investigation. The author would also like to show his appreciation to the many members of the staff of the Applied Research Laboratory at The Pennsylvania State University for their technical assistance and support of this program. Special thanks are extended to Dr. Michael L. Billet for his helpful suggestions and guidance and to Mr. Mark W. McBride for his patience and help with the necessary Streamline Curvature Program modifications.

This investigation was sponsored by the U.S. Naval Sea Systems Command, Code 063R.

1. INTRODUCTION

1.1 Origin of the Investigation

The ever increasing demand for quieter and more efficient aircraft propulsion systems has become an important design consideration in the turbomachinery field. Improvements in the design of a turbomachine, such as an aircraft turbine or compressor stage, will depend heavily on the ability of the design engineer to predict accurately the design and off-design performances of the final machine. This ability to "see" on paper, rather than in a test rig, how a particular machine will perform at various inflow conditions provides both the insight and opportunity necessary to modify the design and obtain the best possible hardware configuration. This process, however, can only be used successfully when the numerical analysis technique used to predict the machine performance has been tested and its accuracy range and computational limitations verified.

The fundamental purpose of any useful numerical analysis method is to calculate a physically correct exit flow field when one is supplied with a specific inlet flow field. This simple "black box" approach calculates the overall machine performance but yields no constructive insight into the complex flow phenomena which occur within the rotating blade row. When the design as well as off-design performance data are required, this type of analysis is not sufficient and some additional information of the intra-blade flow field is necessary. Exact numerical modeling of all the three-dimensional, viscous flow phenomena that occur within the blade row is not computationally possible at the present time. However, through the use of two-dimensional cascade data and

empirical correlations for the major viscous flow effects, it is possible to develop numerical techniques which are capable of calculating the turbomachinery flow field to within an acceptable degree of accuracy. Such an analysis method also allows for the off-design operating conditions to be studied and is thus a most useful tool to the turbomachinery designer.

The manner in which the viscous flow effects are incorporated into a numerical technique, as well as the particular numerical scheme, may differ dramatically between designers. Because each designer uses a somewhat unique method, it is important that the accuracy and dependability of the particular analytic procedure be verified by means of an experimental investigation. Such an investigation consists of numerically modeling a specific turbomachine and comparing the results with detailed flow field measurements. It is only after such an investigation that the accuracy and computational limitations of the procedure are determined and documented. The technique can then play a useful role in the design process.

1.2 Previous Investigations

There has been a considerable amount of work published regarding the development and documentation of turbomachinery through-flow analysis techniques. One of the earlier methods theoretically replaces the rotating blade row by a disk of infinitesimal thickness which models the influence of the blade row by sudden discontinuities in the flow properties. The Actuator Disk theory, as is known and described by Horlock [1],* can be used for a wide variety of turbomachinery flow

*Numbers in brackets indicate References.

field problems including axisymmetric and three-dimensional cases. However, most analyses performed using the actuator disk model are one-dimensional or two-dimensional solutions. When the complexity of the problem requires more detailed descriptions of the flow field, other techniques are generally employed.

In 1952, Wu [2] presented his general theory in which the governing inviscid flow equations on two intersecting stream surfaces, the S_1 and S_2, (Figure 1) were derived. These stream surfaces are more commonly known as the blade-to-blade, S_1, and the hub-to-tip, S_2, surfaces, respectively. This general theory couples the two-dimensional flow field equations for the two surfaces and allows their solutions to interact. This interaction distorts the surface shapes as a function of the overall calculated flow field. Computational techniques and computer storage capacities have only recently progressed to the point where such a fully three-dimensional theory may even be attempted. Using Wu's general theory however, the two-dimensional flow field solutions on both the S_1 and S_2 surfaces can be computed and matched up independently to form quasi-three-dimensional flow field solutions.

The numerical technique most often used to solve Wu's flow field equations is a variation of the finite difference technique and the formulation of the resulting equations into a matrix equation containing the stream function. Marsh [3] has used an irregular finite difference grid pattern to generate a set of nonlinear equations for the S_2 (hub-to-tip) surface. This irregular grid, unlike the conventional rectangular grid, allows the nodal points at which the calculations are conducted to fall on the physical boundaries of the machine. This procedure provides a more detailed solution near the walls of the

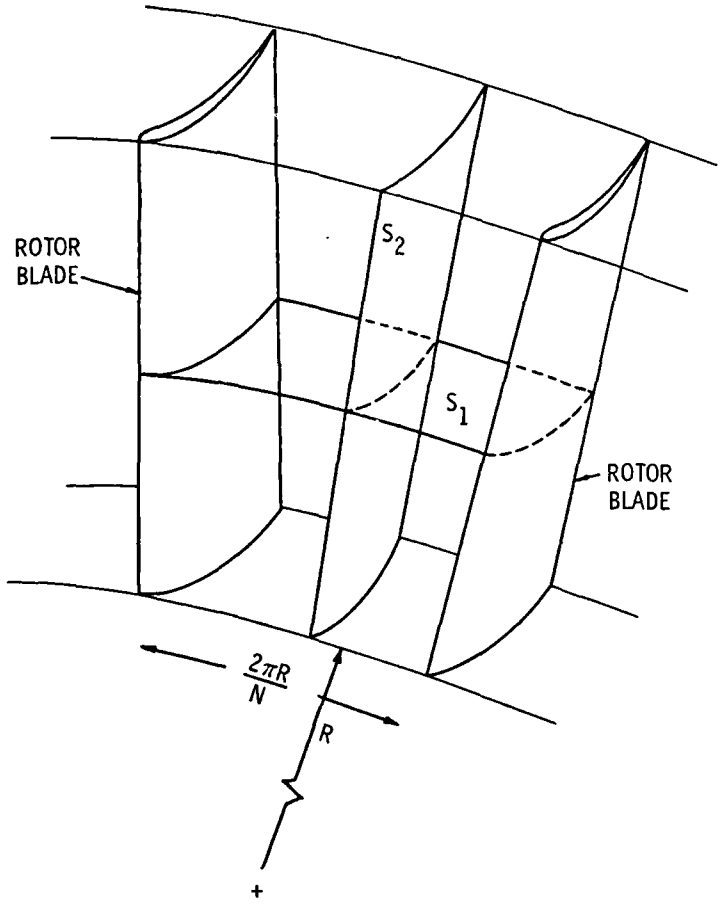

Figure 1. Wu's S_1 and S_2 Calculating Stream Surfaces

curved flow path of a real turbomachine than was previously obtainable with the conventional rectangular grid pattern. The equations are then used to form a matrix equation whose solution uses an iterative technique to determine the stream function.

The flow field solution on the S_1 (blade-to-blade) surface has been investigated by Smith and Frost [4]. Like Marsh, Smith and Frost used an irregular finite difference grid and a matrix equation solution. This solution differs slightly from the hub-to-tip solution in that extreme care must be taken when specifying the upstream and downstream flow boundaries. The resulting solution depends strongly on the chosen inlet and exit flow angles and the manner in which those angles change as the boundaries approach the blade surfaces. Davis [5] has also investigated this Matrix Through-Flow method, as it is known, on both the S_1 and S_2 surfaces for various finite difference grid patterns.

A different approach to the two-dimensional, inviscid, axisymmetric turbomachinery flow field problem is the Streamline Curvature (SLC) method. The SLC was developed independently by Novak [6], Smith [7], and Silvester and Hetherington [8]. This numerical technique expresses the radial component of the inviscid Navier-Stokes equation in terms of the streamline geometry and fluid properties. The meridional velocity is computed using the continuity and energy equations along calculating station lines positioned throughout the flow field. From these velocity distributions, streamline positions can be determined from continuity calculations. The method uses two iterative loops: an outer loop relocates the streamlines based on the calculated velocity distributions at each station; while an inner loop computes a new velocity profile for each station that satisfies the conservation laws

of mass, momentum, and total energy. The iteration cycle is completed when the flow field solution simultaneously satisfies these conservation laws. Although the streamline curvature method does not deal directly with the stream function, it can be shown that the governing equations can be derived from Wu's general theory.

These major axisymmetric through-flow analysis methods, the Matrix Through-Flow and the Streamline Curvature, have been comparatively studied by Davis and Millar [9] and Marsh [10]. These studies focus on computational speed, stability, storage requirements, and numerical limitations, but fail to indicate how accurately these techniques predict the true flow field. The question of accuracy is intentionally not addressed in these studies because the degree of accuracy in the final solution is not as much a function of the particular numerical technique as it is of the manner in which real fluid phenomena are modeled in the overall analysis. This modeling falls outside the basic numerical technique and may vary from user to user or even problem to problem. Thus, the only information which can realistically be provided concerning the accuracy of the final predicted flow field must be from comparisons between the predictions and the actual flow field.

1.3 Objectives of the Investigation

The experimental verification of the inviscid, incompressible, axisymmetric streamline curvature computer program developed by McBride [11] is the objective of this investigation. Independent numerical analyses are conducted on the S_1 (blade-to-blade) and S_2 (hub-to-tip) surfaces using a modified version of McBride's indirect computer code. Modifications were necessary to allow the solution of the direct problem, provide a viscous loss model and handle the necessary boundary

conditions for the S_1 surface solution. The blade-to-blade solution does not include a viscous loss model, as does the hub-to-tip solution, and is compared to a potential flow solution using the Douglas-Neumann [12] cascade computer program. The solutions of the flow field on the two surfaces yield a quasi-three-dimensional map of the turbomachine which is compared to detailed flow field measurements.

The specific turbomachine used in this investigation was the Axial Flow Research Fan (AFRF). This is a research facility housed at the Garfield Thomas Water Tunnel, of the Applied Research Laboratory at The Pennsylvania State Unive ity. The facility consists of an annular flow passage and an instrumented test rotor located approximately six feet from the bellmouth inlet. The test rotor is a nine-bladed, free vortex, cambered rotor with a hub-to-tip ratio of 0.442. Experimental measurements were made at various spanwise locations upstream and downstream of the test rotor, as well as circumferential positions through the blade row. The rotating flow field data were obtained using a rotating mechanism which permitted the traversing of five-hole pressure sensing probes in the S_1 plane. Static pressures on the blade suction and pressure surfaces were obtained through a number of static pressure taps distributed in the spanwise and chordwise directions.

This investigation is primarily directed towards the development and implementation of the procedures and experimental hardware necessary to conduct extensive intra-blade flow field measurements through a rotating blade row. The resulting blade-to-blade flow data allow the verification of existing modeling techniques, as well as providing basic information about the flow physics in this highly three-dimensional complex flow region. Due to time limitations, the accuracy of the SLC

analysis is verified only for the design conditions of the AFRF test rotor. Further studies of the off-design capabilities of the SLC analysis method are a relatively straightforward extension of the work presented in this investigation and should be examined before the worthiness of this analysis method is concluded. Comparisons of experimental and numerical data provide the only verification as to how accurately the numerical analysis can predict the real flow field.

2. NUMERICAL INVESTIGATION OF FLOW FIELD

2.1 Basic Concepts

As previously stated, the inviscid, axisymmetric streamline curvature method expresses the radial component of the inviscid Navier-Stokes equation in terms of streamline geometry and fluid properties. The solution of this radial equilibrium equation, as it is known, and the adherence to the conservation laws of mass, angular momentum and total energy, constitute the major computational foundations of this numerical technique. This analysis method assumes a condition of axisymmetry of the flow field, as well as treating the working fluid as incompressible and inviscid. The governing equations are thus derived with these assumptions in mind. A more detailed description than is provided here of the governing equations and their derivations can be found in Reference [11].

For the axisymmetric through-flow analysis, it is convenient to divide the total velocity vector (V) into its components in the meridional (V_M) and circumferential (V_θ) directions. The meridional velocity is the component of total velocity which is tangent to a streamline at a point and projected into the meridional plane. This velocity component in the meridional plane is the vector sum of the axial velocity (V_x) and the radial velocity (V_R) vectors. Thus, given the meridional velocity and the streamline angle (γ), these components can be computed from,

$$V_x = V_M \cos(\gamma) \tag{1}$$

and

$$V_R = V_M \sin(\gamma) \, . \tag{2}$$

The tangential velocity component is defined in the direction normal to the meridional velocity and is positive in the direction of the blade row rotation. The relationship between the total velocity and its components is given by

$$V^2 = V_M^2 + V_\theta^2 \ . \tag{3}$$

The graphical relationships between all the velocity components are shown in Figures 2 and 3.

To simplify the numerical computations, an intrinsic coordinate system is used throughout the SLC analysis method. This system moves with the fluid particles along the streamlines and is defined by the three unit vectors shown in Figure 4. These direction vectors consist of the two orthogonal vectors in the streamwise and normal directions and a fixed vector in the radial direction. This $\vec{s}$, $\vec{n}$, $\vec{r}$ coordinate system allows the solution of the flow field equations to be carried out along straight or curved calculating station lines without loss of accuracy or an increase in computation time.

2.2 SLC Governing Equations

Meridional curvature of the streamlines throughout a turbomachine tends to disrupt the equilibrium condition in the flow. To satisfy the conservation of momentum principle, a radial static pressure gradient develops as defined by the radial equilibrium equation, Equation (4). The first term of this equation is a function of the local meridional radius of curvature (R_c) of the streamlines. The second term relates directly to the centrifugal force exerted on the fluid particle as it moves in the circumferential direction. Such a rotation occurs whenever a tangential velocity component is present and as the fluid passes

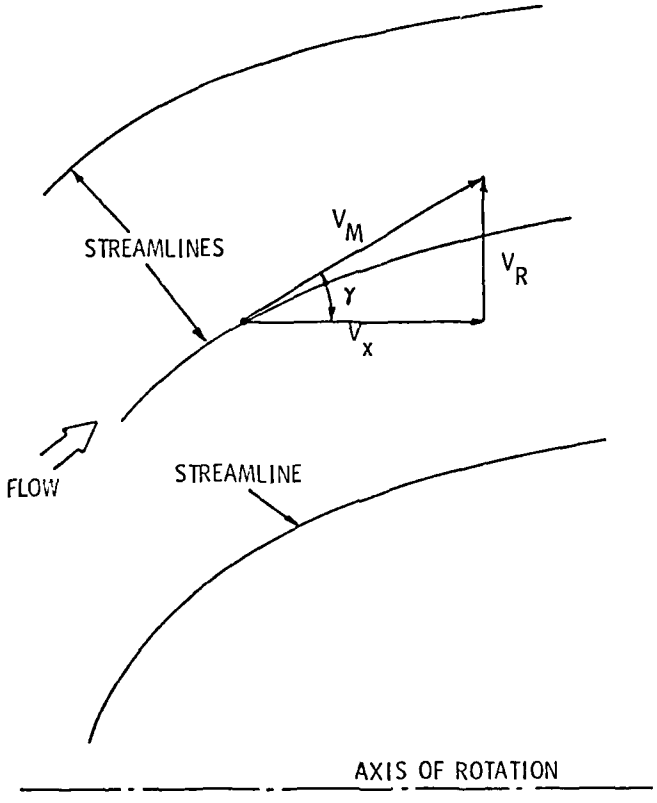

Figure 2. Velocity Vector Relationships in Meridional Plane

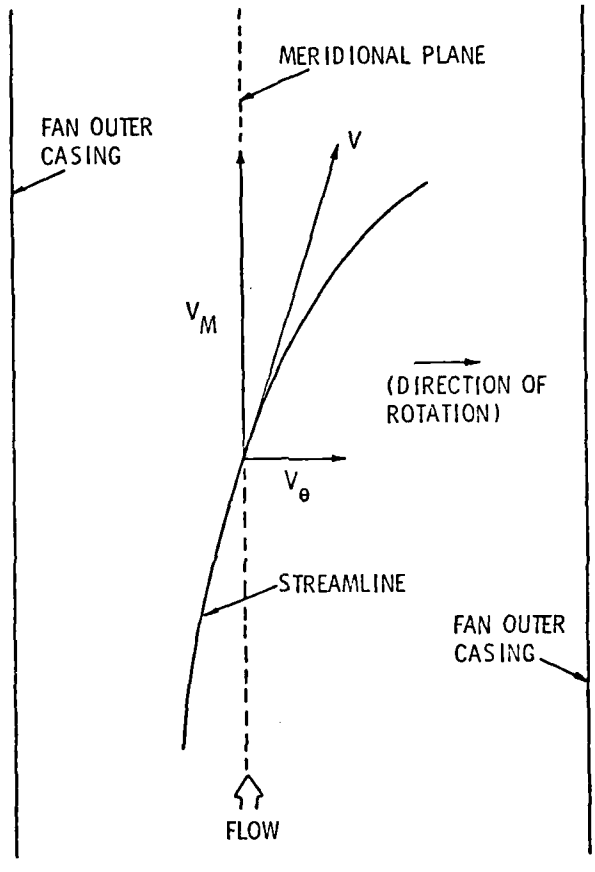

Figure 3. Total Velocity Vector Component Relationships

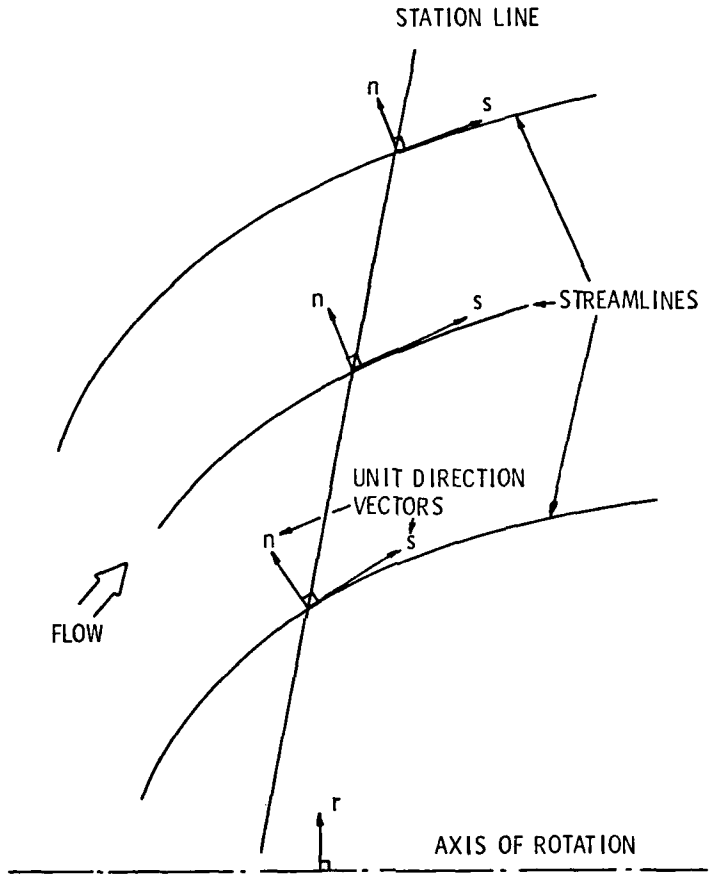

Figure 4. Streamline Curvature Intrinsic Coordinate System

through the rotor. The final term of this radial equilibrium equation reflects the convective acceleration of the fluid particle as the streamtube area either converges or diverges. The combination of these three terms yields the form of the radial equilibrium equation which is used in the streamline curvature analysis method. The differential form of this equation is expressed as

$$\frac{dP}{\rho} = \frac{V_M^2}{R_c}\, dn + \frac{V_\theta^2}{r}\, dr - V_M \frac{\partial V_M}{\partial s}\, ds \ . \tag{4}$$

Since the SLC analysis is an axisymmetric, incompressible, inviscid method, the total energy along a streamline must be conserved until it is changed by some energy transferring device such as a rotor or stator. The rotor changes the angular momentum of the fluid as well as producing some energy losses while a nonrotating blade row, a stator, will only cause losses in energy. These changes which occur through a blade row, whether stationary or rotating, must remain constant in the downstream blade-free region until other blade rows are encountered. Thus, between any two points along the same streamline in the blade-free region the total pressures can be related by

$$P_\infty + \frac{1}{2}\rho V_\infty^2 = P_\eta + \frac{1}{2}\rho V_\eta^2 \ , \tag{5}$$

where the subscript (∞) indicates a calculating station of known static pressure and total velocity and the subscript (η) indicates an arbitrary station within the blade-free region.

Using the relationship for the total velocity developed in Equation (3), the right-hand side of Equation (5) can be written as

$$P_\infty + \frac{1}{2}\rho V_\infty^2 = P_\eta + \frac{1}{2}\rho (V_M^2)_\eta + \frac{1}{2}\rho (V_\theta^2)_\eta \ . \tag{6}$$

This expression can be expanded further if the following relationship is considered:

$$P_\eta = (P_i)_\eta + \int_i^0 (dP)_\eta \ , \tag{7}$$

where $(P_i)_\eta$ is the static pressure on the innermost streamline at the arbitrary station (η) and the integration limits are from the inner (i) to the outer streamline ($_0$).

Integration of the radial equilibrium equation, Equation (4), yields the static pressure difference between the inner and outer streamlines. Thus, it is possible to combine Equations (5) through (7) and obtain an expression for the meridional velocity at station (η):

$$\frac{1}{2}\rho\,(V_M^2)_\eta = P_\infty + \frac{1}{2}\rho\,V_\infty^2 - (P_i)_\eta - \int_i^0 (dP)_\eta - \frac{1}{2}\rho\,(V_\theta^2)_\eta \ . \tag{8}$$

The static pressure on the inner streamline (P_i) is not directly known, and so Equation (8) cannot be solved as it stands. Instead, the integral form of the continuity equation given by

$$2\pi\,\rho \int_i^0 (V_M)_\eta \, dn = \text{CONSTANT} \tag{9}$$

is combined with Equation (8) to produce the relationship

$$2\pi\,\rho \int_i^0 \left\{ \frac{P_\infty}{\frac{1}{2}\rho} + V_\infty^2 - \frac{(P_i)_\eta}{\frac{1}{2}\rho} - \int_i^0 \frac{(dP)_\eta}{\frac{1}{2}\rho} - (V_\theta^2)_\eta \right\}^{1/2} dn = 2\pi\,\rho \int_i^0 (V_M)_\eta \, dn \ . \tag{10}$$

Since $(P_i)_\eta$ is a constant for each station, it may be removed from inside the integration limits and solved for directly. Once $(P_i)_\eta$ is known, a meridional velocity profile for each station can be computed that satisfies radial equilibrium and total energy conservation.

To complete the flow field calculations, the tangential velocity profiles must be computed for each station. The law of conservation of angular momentum states that the angular momentum is constant along a streamline in the blade-free regions with a change occurring only through a rotating blade row. This momentum change is associated with the energy supplied by the rotor and is reflected by the change in tangential velocity from leading to trailing edges. Thus, by knowing the tangential velocity profile at some upstream reference station, as well as knowing the change in tangential velocity across the rotor (i.e., the work done by the rotor), the tangential velocity profiles at all other stations can be calculated based on angular momentum conservation.

2.3 SLC Computational Procedure

The SLC analysis method uses an iterative procedure which involves the equations of radial equilibrium, total energy, and continuity. Once an initial approximation of the flow field is obtained based on the upstream reference velocity profiles, the conditions of constant mass flow rate and angular momentum are satisfied. The integration of the radial equilibrium equation together with the values of the static pressure on the inner streamline allows new meridional velocity profiles to be computed for each calculating station via the energy equation. Given these updated velocity distributions, the positions of all the streamlines are adjusted to satisfy the continuity equation. Due to the

realignment of the streamlines, however, the constant angular momentum condition must be rechecked and the redistribution of tangential velocity is then applied throughout the flow field. At this point the radial static pressure gradient at each station is computed and is used once again in the energy equation to yield new meridional velocity profiles. These profiles are then used to reposition the streamlines for the second time and the entire iteration cycle is repeated until the values of velocity, and thus streamline positions, do not change within prescribed limits from one iteration pass to the next. At this point the solution is considered to be the correct converged flow field solution which simultaneously satisfies the physical conservation laws of mass, total energy, and momentum.

The computational steps and the required direct problem boundary conditions are shown in Figure 5. The first step of this process is to obtain some reasonable approximation of the flow field so that through successive iteration, the converged solution can be obtained. The initial flow field is determined based on the specified distributions of meridional and tangential velocity along an arbitrary upstream station line. These velocity distributions determine the total energy of the fluid and are therefore the first necessary boundary condition which must be supplied. By specifying the percentage of total mass flow rate to be enclosed within each streamtube and by conserving angular momentum throughout the blade-free regions of the flow field, the initial streamline positions and velocity profiles can be computed for each station. The flow field downstream of the rotating blade row requires additional information prior to its initial computation. The information which is needed is directly related to the amount of energy

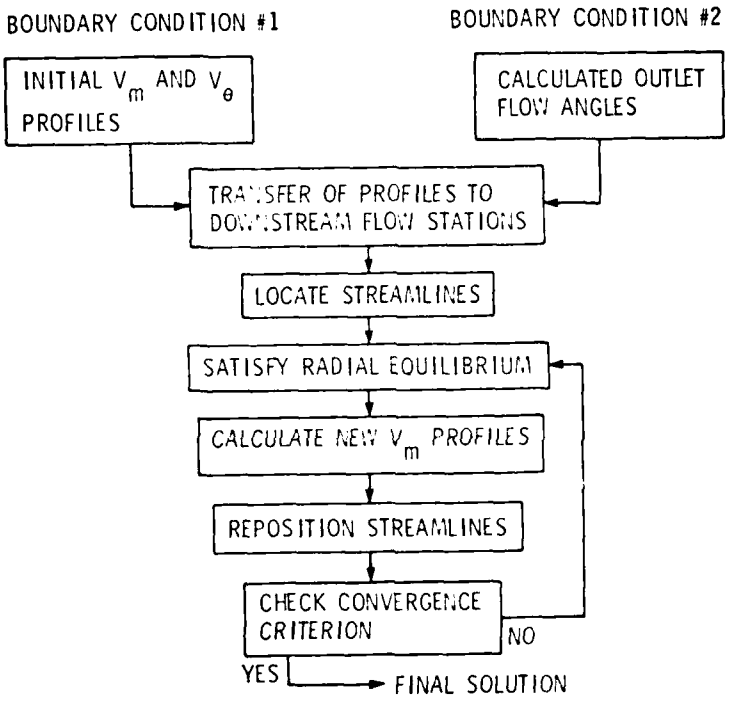

Figure 5. Flow Diagram of Streamline Curvature Axisymmetric Analysis Method

that the rotor adds to the fluid and is supplied in terms of a tangential velocity profile at the blade row trailing-edge. This velocity profile, which allows the downstream profiles to be determined from the angular momentum equation, is computed from the second boundary condition.

The designer of a rotating machine will determine the energy change across the rotating blade row by specifying (the design or indirect problem) the tangential velocity distribution at the blade row trailing-edge. The analysis of the very same machine (the direct problem), on the other hand, requires the calculation of the existing tangential velocity profile based on the physical geometry of the blade row. Figure 6 shows a typical axial flow fan rotor blade section and its inlet and exit velocity diagrams. From the exit velocity triangles, it is possible to calculate the tangential velocity if the section geometric properties are known. Once the exit velocity profiles are computed for each blade section, the downstream flow field parameters can be established and the iteration procedure is initiated until a converged solution results.

2.4 Calculation of Exit Flow Angles

The calculation of the proper exit spanwise flow angularity distribution is an important step in the overall hub-to-tip SLC flow field solution. The difficulty in calculating this distribution centers around the fact that the ideal relative outlet flow angle (β_2), shown in Figure 6, is not the angle at which a real, viscous fluid will exit from a blade section. The actual fluid will not experience as much turning (energy addition) from the leading to trailing-edge as this angle would lead one to believe. For this reason, a deviation angle

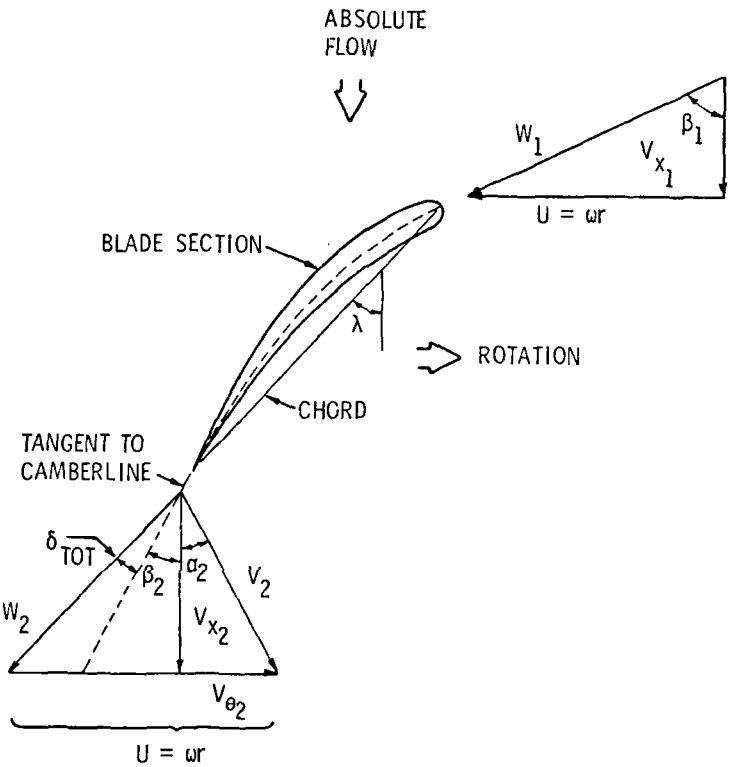

Figure 6. Typical Axial Flow Fan Blade Section Geometry

(δ_{TOT}) must be calculated to include the reduction in turning which is primarily due to viscous flow phenomena. The computation of this deviation angle for each radial blade section is the only loss model which is incorporated into this direct hub-to-tip streamline curvature analysis.

Once the total deviation angularity distribution is known, the actual exit flow angles are calculated from

$$\beta_2^* = \beta_2 + \delta_{TOT} \tag{11}$$

for each radial section. This actual flow angle (β_2^*) can then be used to calculate the exit tangential velocity profile from

$$V_{\theta_2} = U - V_{x_2} \tan (\beta_2^*) \quad . \tag{12}$$

This loss model based on blade section deviation angles allows the inviscid SLC analysis program to model the flow field of a turbomachine with real viscous and secondary flow effects.

2.5 Calculation of Deviation Angles

The blade section relative flow angle (β_2) is defined as the angle formed by a line which is tangent to the section camberline at the trailing-edge and the axial velocity vector. This angle, sometimes known as the metal angle, is the angle at which the relative flow would exit from the blade row if the working fluid perfectly followed the camberline from leading to trailing edge. However, due to several viscous and secondary flow phenomena, the working fluid will deviate from this ideal path and thereby exit at some angle other than the metal angle. The difference between the actual relative flow angle

and the metal angle is called the deviation angle. The accurate determination of the deviation angle at each spanwise location allows the modeling of the viscous and secondary flow phenomena by the inviscid SLC analysis of the axisymmetric turbomachine.

The procedure which is used to calculate the final deviation angularity distribution involves a three-part interaction with the streamline curvature analysis. This procedure was selected so that, as more complex terms are added to the deviation angle computation, the flow field necessary to compute the deviation is the best available approximation. The initial flow field solution incorporates the measured blade section metal angles and a spanwise deviation distribution based on the development by Howell [13]. Howell's two-dimensional cascade correlation is based on nominal conditions which he defines as those pertaining to a cascade deflection which is 80 percent of the maximum stalling deflection. Howell's modification of a rule formulated by Constant [14] is a first order correction to the ideal flow angle based on section camber angle (θ_c), space-to-chord ratio and outlet metal angle. This correlation is given as

$$\delta_H = \frac{\beta_2 + 0.23\ \theta_c\ (S/C)^{1/2}(2a/c)^2}{1.0 - 0.002\ \theta_c\ (S/C)^{1/2}} - \beta_2\ , \qquad (13)$$

where a/c is the fraction of the chord at the point of maximum camber. A derivation of Equation (13) is shown in Appendix A. Using the blade row exit angularity profile generated from Howell's correlation equation and the given upstream velocity profiles, the SLC analysis yields a converged flow field solution which satisfies these input boundary

conditions. The computed velocity profiles at the blade row leading- and trailing-edges are then used to calculate three separate deviation terms based on primary flow phenomena.

Lakshminarayana [15] has developed a deviation formula based on the change in circulation due to the axial acceleration of the flow through the blade row, This deviation term is expressed as

$$\delta' = \frac{AVR - 1.0}{AVR} \cos^2(\beta_2) \left\{ \tan(\beta_2) + \frac{\left\{ \frac{\pi K(c/s)[(G/c) + (\alpha/4)]\cos(\beta_m)[(AVR + 1.0)^2 - 4]}{(AVR - 1.0)} - \frac{2\pi K(c/s)\tan(\beta_1)}{AVR\cos(\beta_m)\sec^2(\beta_1)} \right\}}{8 + \pi K(c/s)[(G/c) + (\alpha/4)]\cos(\beta_m)[(AVR + 1.0)\tan(\beta_2) + 2\tan(\beta_1)]} \right\}, \quad (14)$$

where AVR is the axial velocity ratio (V_{X_2}/V_{X_1}), K is the cascade influence coefficient [16], G is the distance from the chord line to the point of maximum camber, β_m is the mean flow angle [$1/2(\beta_1 + \beta_2)$], and α is the difference between the inlet flow angle and the stagger angle ($\beta_1 - \lambda$).

Howell's deviation formula assumes that the thickness of the blade section is zero or very small; thus, the effects of a finite thickness distribution must be included in the formulation of the final deviation angle profile. Empirical cascade data has been collected by the National Aeronautics and Space Administration (NASA) and correlated by Lieblein [17]. Based on these data, Lieblein developed a deviation

calculation as a function of blade section solidity and inlet flow angle. The deviation of the flow due to the blade thickness is given by

$$\delta^* = (\delta_0{}^0)_{10} \cdot (K_\delta)_{sh} \cdot (K_\delta)_t \ , \tag{15}$$

where $(\delta_0{}^0)_{10}$ represents the deviation angle of a 10 percent thick NACA 65-series thickness distribution obtained from the experimental data. The remaining terms of Equation (15) are corrections to the basic deviation angle for thickness distributions other than NACA 65-series, and maximum thickness-to-chord ratios of other than 10 percent, respectively.

Also presented in Lieblein's development of the primary flow deviation angle is a better approximation of the effects of blade camber. This camber induced term replaces the previous deviation based on Howell's correlation. This improved camber term is given by

$$\delta_0 = m \cdot \theta_c \ , \tag{16}$$

where the value of m, known as the slope factor, is based on empirical cascade data as a function of blade solidity and inlet flow angle. Having calculated the deviation angle terms from Equations (14) through (16) for each blade section, the cumulative effect of the viscous phenomena is reflected in the primary deviation angle given as

$$\delta = \delta^* + \delta_0 - \delta' \ . \tag{17}$$

This second order correction for the viscous flow effects is then used to generate an improved flow field solution from the SLC analysis which reflects some of the major losses which occur through the blade row.

The effects of secondary flows are most influential in those regions of large inlet velocity gradients. For the axial flow fan problem, such gradients exist near the outer casing and inner hub

surfaces. These secondary flows produce a streamwise component of vorticity which is not considered in the previous deviation angle computations. After obtaining an inlet normal vorticity profile from the rotor inlet axial velocity profile supplied by the SLC analysis, the secondary vorticity at the rotor exit station is calculated. From this secondary vorticity, a secondary stream function is defined in the exit plane. The solution of this stream function yields perturbation velocities which are then used to determine an additional deviation (δ_S) due to the secondary flow phenomenon. From this calculation, a new outlet flow angularity distribution is defined by

$$\beta_2^* = \beta_2 + \delta + \delta_S \quad . \tag{18}$$

A more complete description of the secondary flow phenomenon and the numerical solution of the necessary equations is provided by Billet [17].

The effects of tip leakage flows is also a major turbomachinery secondary flow phenomenon which must be addressed in this numerical analysis technique. Lakshminarayana [18] has investigated tip clearance effects in axial flow turbomachinery and derived a relationship for an additional deviation angle term. This calculation is based on a vortex model in the tip region. The induced velocity effects cause a change in the outlet flow angle given by

$$\delta_T = \tan^{-1} \left\{ \frac{(1 - K)\, C_{L_T}\, c}{4\pi\, ar} \left(\frac{r}{ar}\right) \right\} , \tag{19}$$

where C_{L_T} is the tip section lift coefficient, and r/ar is the local radius in the vortex core divided by the vortex core radius. The relationship

$$\frac{ar}{\tau} = 0.14 \left\{ \frac{d}{\tau} \sqrt{C_{L_T}} \right\}^{0.85} \tag{20}$$

yields the value of the vortex core (ar) for a given value of tip clearance (τ) and longitudinal distance (d) from the leading edge. The deviation angle also is a function of the distance from the end wall (y) and the local radius of the vortex core (r) given by

$$r = ar + \tau - y \, . \tag{21}$$

The value of the (1 - K) term in Equation (19) is obtained from experimental data and the equation

$$(1 - K) = 0.23 + 7.45 \, (\tau/S) \tag{22}$$

for values of tip clearance to blade spacing between 0.10 and 0.01.

The main purpose of considering this leakage flow deviation angle term is to obtain some feel for the magnitude of the leakage flow induced deviation angles at the blade tip. Since it was felt that the greatest deviation would occur inside the vortex core, only this region is considered and is reflected in the use of Equation (19). For the region outside of the vortex core, Equation (19) is no longer valid and additional relationships must be sought. This is perhaps the weakest link in the total deviation angle chain since the effect of leakage flow is not confined to only the tip section and must be distributed along the blade span. However, such a distribution is not considered in this investigation and the total effect is concentrated at the rotor tip.

The final flow field solution is computed based on the total deviation angle calculated at each radial location from the relationship

$$\delta_{TOT} = \delta_0 + \delta^* - \delta' + \delta_S + \delta_T \quad . \tag{23}$$

This total deviation angle distribution is added to the blade metal angles and used as the final boundary condition of the streamline curvature analysis. The resulting converged flow field solution includes the effects of blade camber, thickness, axial velocity accelerations, secondary vorticity, and tip leakage flows.

The final results obtained from the SLC procedure just outlined rely foremost on the ability of the deviation angle calculations to model the actual loss mechanisms which occur in the real flow field. Improvements and modifications of these models are always desirable as more accurate experimental data and correlations become available. However, at the present time, the loss models used in this analysis method are simple enough to use quickly and without major computational difficulties while still providing an acceptable degree of accuracy. It should also be noted that all the deviation angle calculations have unique limitations and are only valid for specific ranges of flow conditions and blade shapes. The limitations, therefore, of each calculation must be carefully examined and studied before these loss models can be expected to produce accurate flow field solutions.

2.6 The Blade-to-Blade Analysis

2.6.1 The SLC Method. The previous development of the axisymmetric streamline curvature method is only valid for solving the two-dimensional flow field on the S_2 stream surface. The solution of the S_1 stream surface requires a slight modification of the program coding. In addition to the nonannular flow passage, the blade-to-blade analysis requires somewhat different boundary conditions. The initial S_1

surface flow field energy is again established by specifying the upstream reference station velocity profiles, but the exit flow angle is not input directly as it was for the axisymmetric solution. Instead, the physical flow boundary of the problem defines the flow angularity for each blade section. This angularity, and thus the flow boundaries, must vary for each blade section that is to be considered. Figure 7 shows a typical cascade section which has been set up with the necessary flow boundary configuration.

In addition to the governing equations of motion, an important principle must also be satisfied before a converged blade-to-blade solution is acceptable. Figure 7 shows four points on the flow boundaries labeled ① and ② upstream of the blades and ③ and ④ downstream. These pairs of points are actually located at identical positions relative to the cascade since the upper streamline of one blade section would become the lower streamline of the adjacent blade section in the infinite cascade of blade sections. The key assumption throughout the SLC analysis has been one of axisymmetry; thus, the flow field at points ① and ② must be the same, and similarly, points ③ and ④ must show identical flow properties. This condition, known as periodicity, must be satisfied together with the previously mentioned conservation laws to yield a physically accurate solution.

The procedure which is used to calculate the final blade-to-blade flow field requires an additional iteration loop to be added to the analysis. Figure 8 represents the computational steps required for this S_1 surface solution. The first step of this procedure is to calculate the inlet and exit flow angles for each radial section based on the solution of the axisymmetric flow field on the S_2 surface. These flow

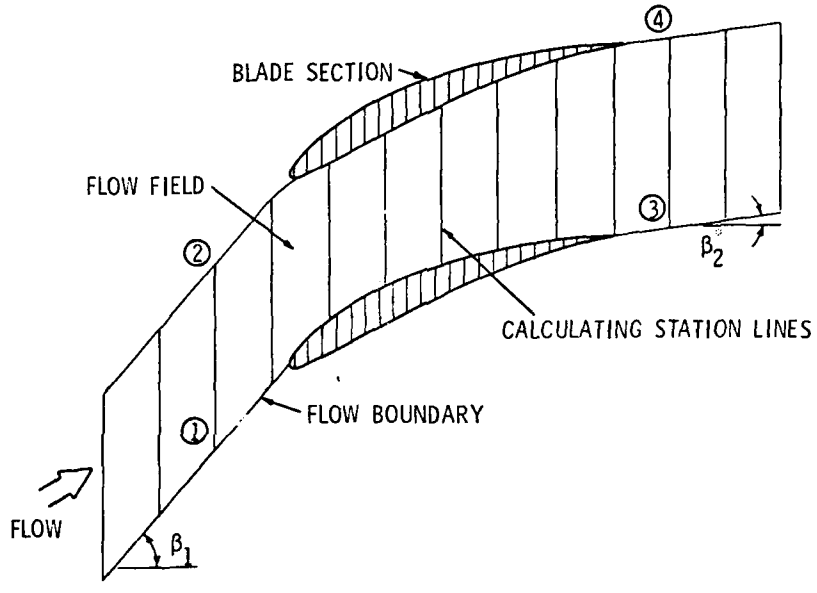

Figure 7. Streamline Curvature Blade-to-Blade Solution Problem Geometry

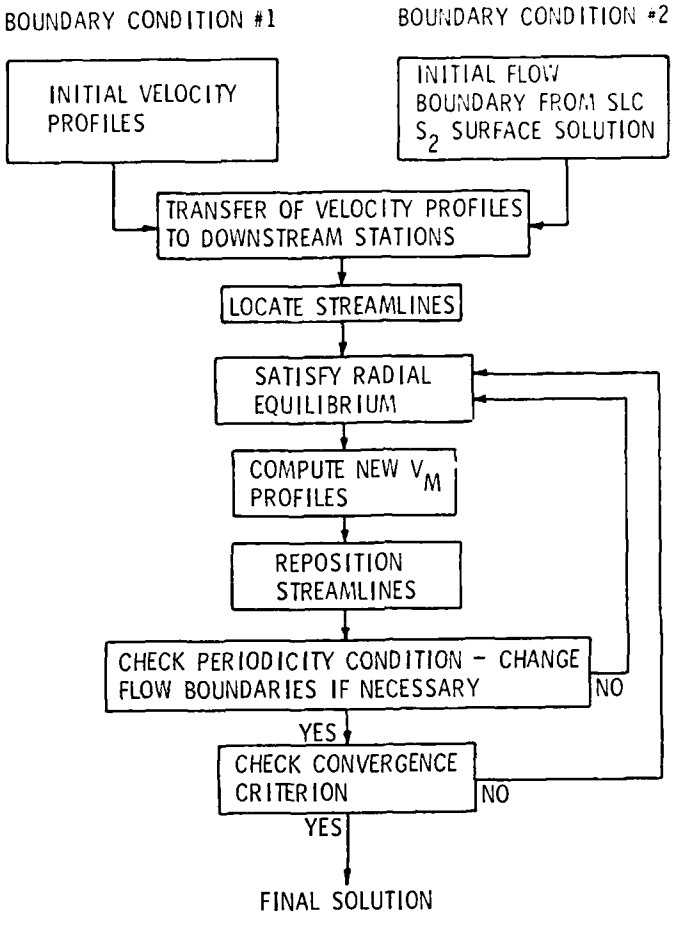

Figure 8. Streamline Curvature Blade-to-Blade Computational Flow Diagram

angles along with the individual blade section coordinates provide the preliminary flow field boundaries similar to those shown in Figure 7. Each time the flow field is recalculated, the periodicity condition is checked. If this condition is not met, the flow boundaries are adjusted slightly and the flow field is recalculated. The amount of adjustment and precisely which direction the adjustment is made is determined from a momentum consideration. It is first assumed that the integrated value of radial momentum along each station line upstream of the blade surface is constant. It is further assumed that the difference between this constant value and any other at a station is related to the streamline angle which is governed by the angle of the flow boundary. Thus, the periodicity condition is met when the integrated value of radial momentum for each upstream station is equal to that of the reference station, and the downstream stations are equal to the value at the trailing edge since radial momentum changes through the cascade. This radial momentum is computed for each station outside the blade surfaces from

$$(M_R)_\eta = \rho \int_i^0 (V_R\, V_M)_\eta \, dn \quad , \tag{24}$$

where

$$dn = dr \sin(\delta) \quad . \tag{25}$$

The integration limits and directions are shown in Figure 9 along with the definition of δ.

The upstream reference station is assumed to have the correct radial momentum since the velocity profiles are user-specified and do not change during the calculation procedure. The difference between

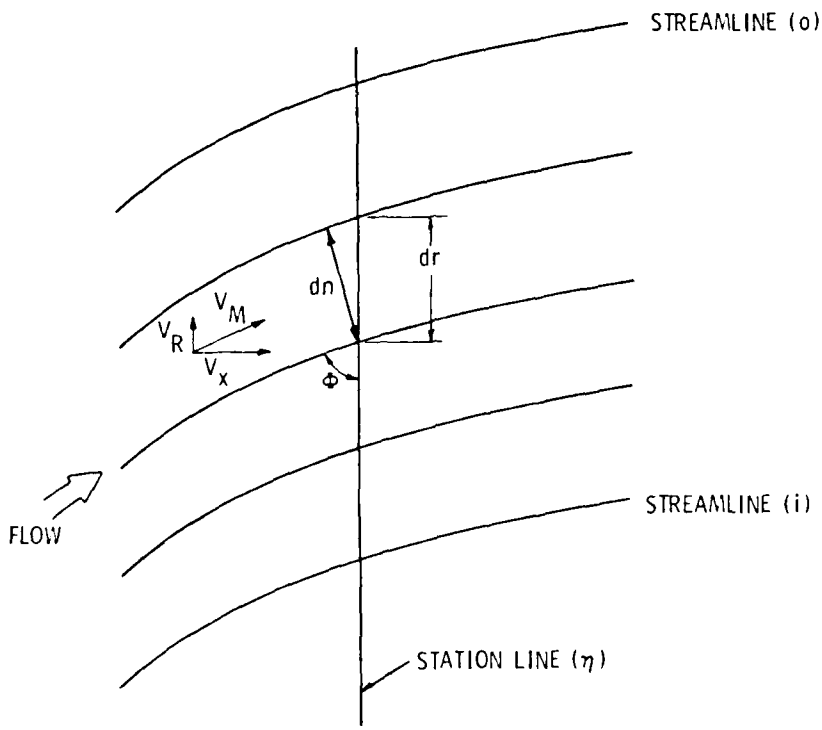

Figure 9. Streamline Curvature Integration Directions

this value of radial momentum and an arbitrary upstream station is related to an average change in radial velocity across the channel given by

$$(\Delta V_R)_\eta = \frac{(M_R)_{REF} - (M_R)_\eta}{\rho \int_1^0 (V_M)_\eta \, dn} . \tag{26}$$

This change in radial velocity is then used to adjust the radial location of the flow boundary coordinates by computing a new flow angle (Φ') based on the new velocity triangles:

$$(\Phi')_\eta = \tan^{-1} \left\{ \frac{V_X}{V_R + \Delta V_R} \right\}_\eta . \tag{27}$$

This new angle at station (η) creates a change in the boundary coordinates of all upstream stations by an amount equal to

$$(\Delta R)_{(\eta-1)} = \left[\frac{X_\eta - X_{(\eta-1)}}{\tan \Phi'} \right] - \left[R_\eta - R_{(\eta-1)} \right] . \tag{28}$$

This value of ΔR is used to adjust all the upstream stations before the same calculation is applied at station (η-1) and so on until the reference station is reached. Figure 10 shows graphically the change in radial coordinates based on the change in streamline angle of the downstream station. This entire procedure begins at the leading-edge station and marches upstream until all the upstream coordinates have been adjusted.

The flow field solution which is calculated within the blade passage satisfies the radial equilibrium equation, as well as total energy and momentum conservation. Since these interior stations can

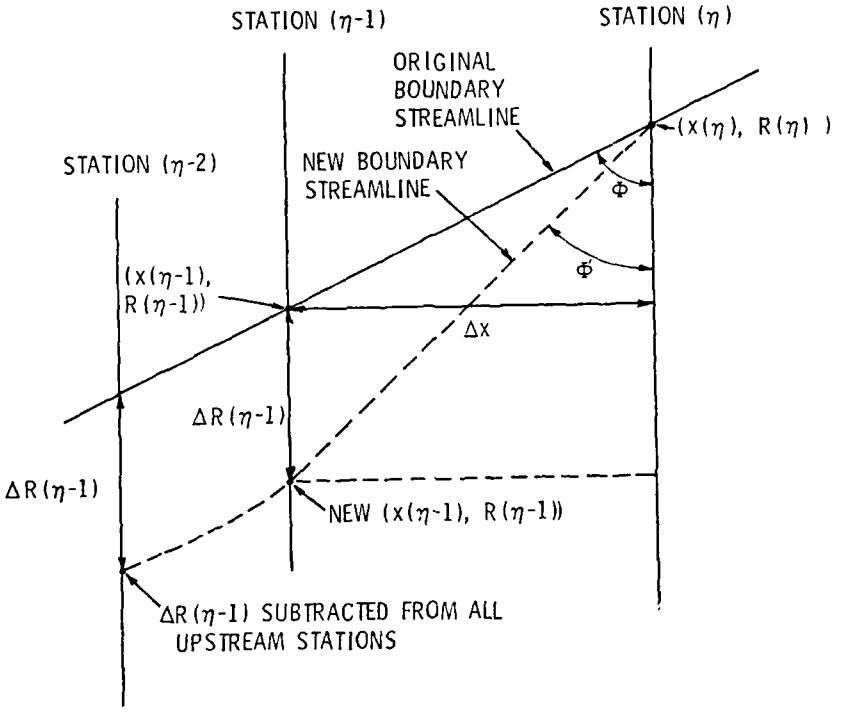

Figure 10. Adjustment of Flow Boundaries from Periodicity Condition

exhibit a change in flow properties across the channel which reflect the blade forces, there is no need for a periodicity condition in this region. It is therefore assumed that the calculated velocities at the trailing-edge station are correct and the periodicity computations are subsequently applied to the downstream stations based on the trailing-edge conditions. Once the entire upstream and downstream flow field boundaries have been adjusted, the SLC flow equations are solved and the iteration cycle is repeated until the periodicity condition is met and the governing equations are satisfied. Although the use of the radial momentum and the change in radial velocities is merely an approximation to the periodicity condition, it is clear that as the periodicity condition converges the approximation becomes better.

The SLC blade-to-blade solution does not incorporate any viscous or secondary flow loss model as does the hub-to-tip solution. Thus, the S_1 surface solution is purely an inviscid, incompressible, two-dimensional solution. An improvement to the analysis would involve calculating a displacement thickness along the blade from a boundary layer analysis and computing a modified flow boundary to account for the blockage effects of this phenomenon. Further, an iterative scheme could be used to solve the viscous-inviscid flow interactions between the boundary layer and the free-stream flow to improve computational accuracy. These types of modifications have been investigated by Gliebe [20] and others, but are not within the scope of this investigation.

2.6.2 The Douglas-Neumann Method. The development of the streamline curvature blade-to-blade computer code is a new and untested

modification of the direct SLC analysis program. For this reason, the Douglas-Neumann [12] cascade computer program is used as a secondary check of the SLC S_1 surface solution. The Douglas-Neumann (D-N) program yields the potential flow solution for a particular cascade geometry given the body coordinates and the inlet flow angle. The use of a distribution of various strength sources along the blade surface, such that the flow normal to the surface is zero, forms the basis of this inviscid analysis. The cascade vorticity distribution is obtained by using the same flow equations and simply rotating the source velocity vectors by 90 degrees. The strength of each source is constant along straight line segments connecting adjacent body points; however, the strength may vary between segments. This integral technique has the characteristic of approaching the exact potential flow solution as the distrance between sources approach zero.

The solution of a general infinite two-dimensional cascade problem is obtained by calculating the potential, inviscid flow for three basic conditions and then superpositioning the results. The three conditions include the zero angle of attack, 90-degree angle of attack, and purely circulatory flow. The combination of these solutions enables the velocity and static pressure to be calculated on the suction and pressure surfaces, as well as the total cascade turning angle. The final solution as well as the intermediate steps must also satisfy the Kutta condition at the trailing-edge.

3. NUMERICAL PROCEDURES AND RESULTS

3.1 The Axisymmetric Analysis

The first phase of the axisymmetric analysis of the AFRF nine-bladed cambered test rotor involves the solution of the flow field based on the rotor design parameters. This particular free-vortex rotor design assumed a uniform inlet axial velocity distribution with no swirl upstream of the leading edge. Using such an inlet velocity profile and the blade row geometric parameters given in Table 1, the SLC analysis of the AFRF test rotor was performed. The first approximation of the outlet flow angles was obtained through the use of Howell's correlation data. Table 2 provides the calculated parameters used as input to the SLC program. Figure 11 represents the converged flow field solution in a plot of velocity ratios as a function of radius at the blade row exit station. As the figure indicates, the solution of the flow field based on Howell's correlation over-predicts the rotor design performance by as much as 30 percent. This over-prediction is expected and with the addition of improved loss models, the comparison between prediction and design values should improve.

To further improve the solution accuracy, the primary flow deviation angles were computed and input to the next run of the SLC analysis code. Table 3 provides the results of the primary deviation angle calculations. With these improved angles, the SLC analysis technique produced a converged flow field solution shown in Figure 12. This plot of the velocity profiles at the blade row trailing-edge shows considerable improvement over the first prediction. At this

Table 1. Axial Flow Research Fan (AFRF) Rotor Geometric Parameters

SECTION NO.	R/R_{TIP}	STAGGER (DEG)	CHORD (cm) (c)	S/C	t/c	G/c	θ_c (DEG)	β_2 (DEG)
1	0.4419	23.140	15.24	0.5526	0.1	0.0792	39.8	4.340
2	0.4977	31.020	15.24	0.6225	0.1	0.0592	24.8	19.020
3	0.6093	42.438	15.24	0.7621	0.1	0.0396	17.5	33.738
4	0.7209	50.273	15.24	0.9017	0.1	0.0217	10.5	44.273
5	0.8326	55.784	15.24	1.0413	0.1	0.0158	6.2	52.784
6	0.9442	59.850	15.24	1.1810	0.1	0.0108	4.6	57.550
7	1.0000	61.589	15.24	1.2508	0.1	0.0104	3.5	60.089

R_{TIP} = 27.305 cm

a/c = 0.30

$\phi = \frac{V_\infty}{U_{TIP}} = 0.432$

$(K_\delta)_{sh}$ = 1.1

Table 2. Howell's Deviation Angle Calculation Results

SECTION NO.	β_2 (DEG)	δ_H (DEG)	β_2^* (DEG)	FRACTION OF BLADE SPAN
1	4.340	2.877	7.217	0.0
2	19.020	2.461	21.481	0.1
3	33.738	2.368	36.106	0.3
4	44.273	1.743	46.016	0.5
5	52.784	1.207	53.991	0.7
6	57.550	0.999	58.549	0.9
7	60.089	0.801	60.890	1.0

$$\delta_H = \frac{\beta_2 + 0.23\ \theta_c\ (S/C)^{1/2}\ (2\ a/c)^2}{1.0 - 0.002\ \theta_c\ (S/C)^{1/2}} - \beta_2$$

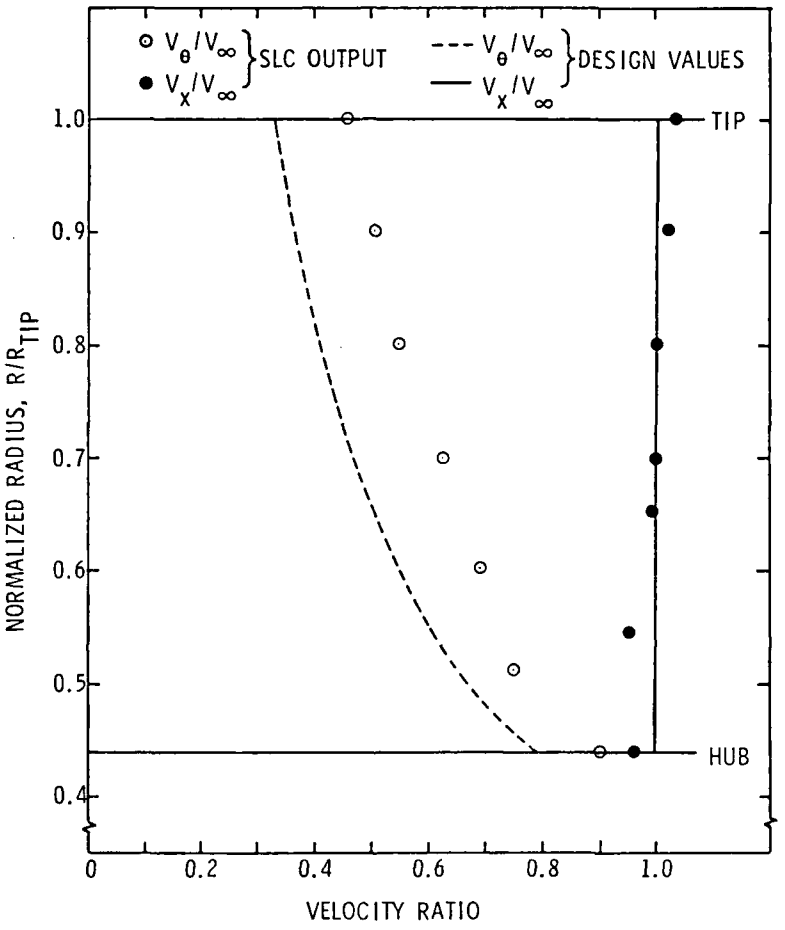

Figure 11. Streamline Curvature Exit Flow Field Based on Howell's Deviation and Uniform Inlet Axial Velocity

Table 3. Primary Flow Deviation Angle Calculations - Uniform Inlet Velocity Profile

SECTION NO.	β_2 (DEG)	$(K_\delta)_{sh}$	$(K_\delta)_t$	$(\delta_0{}^0)_{10}$ (DEG)	δ^* (DEG)	δ' (DEG)	m	δ_0 (DEG)	δ (DEG)	$\beta_2{}^*$ (DEG)
1	4.340	1.1	1.0	6.409	7.050	-0.132	0.177	1.559	8.741	13.081
2	19.020	1.1	1.0	4.582	5.040	-0.522	0.203	1.678	7.240	26.260
3	33.738	1.1	1.0	3.927	4.320	-0.205	0.247	1.860	6.385	40.123
4	44.273	1.1	1.0	2.745	3.020	0.144	0.237	1.912	4.788	49.061
5	52.784	1.1	1.0	1.854	2.040	0.057	0.329	1.884	3.867	56.651
6	57.550	1.1	1.0	1.527	1.680	0.471	0.365	1.824	3.033	60.583
7	60.089	1.1	1.0	1.209	1.330	0.399	0.330	1.795	2.726	62.815

$$\delta^* = (\delta_0{}^0)_{10} \cdot (K_\delta)_{sh} \cdot (K_\delta)_t$$

$$\delta_0 = m \cdot \theta_c$$

$$\delta = \delta^* + \delta_0 - \delta'$$

$$\beta_2{}^* = \beta_2 + \delta$$

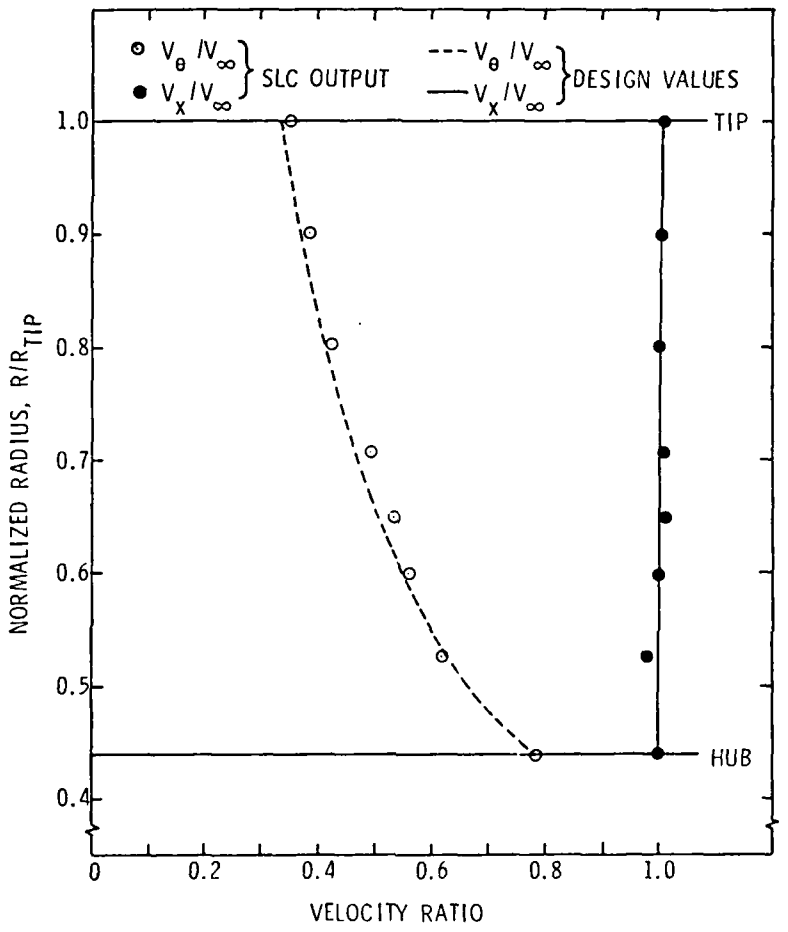

Figure 12. Streamline Curvature Exit Flow Field Based on Primary Flow Deviation Angles and Uniform Inlet Axial Velocity

point, the maximum error between the design and predicted values is less than four percent. There is no additional deviation angle calculation for secondary flow effects in this phase of the investigation due to the assumed uniform inlet velocity profile. The uniform profile does not produce a normal vorticity profile going into the rotor and thus there can be no secondary vorticity exiting from the rotor. The purpose of conducting this preliminary flow field analysis based on the rotor design parameters was to test the numerical data, as well as the SLC computer coding. Since this test rotor was designed by the method outlined by Lieblein [17], the results of an analysis using the same basic technique should result in good agreement. Based on the results shown in Figure 12, the geometric properties of the blade sections are accurate and the SLC program seems to function as expected.

The next phase of this analysis was to conduct the entire procedure over again using the actual inlet axial velocity profile which the rotor experiences in the AFRF facility. This inlet axial velocity profile, which was measured during the experimental phase of this investigation, is shown in Figure 13. The actual data points are not used directly in the SLC program, but rather a smooth spline curve through these points is used to define the inlet profile. This inlet velocity profile clearly indicates the existence of a boundary layer on both the inner and outer surfaces. The streamline curvature technique is now called upon to predict the actual flow field of the AFRF test facility based on the measured inlet flow field. The calculation of Howell's deviation angles is not a function of the inlet conditions, thus those angles computed previously are used in conjunction with the inlet

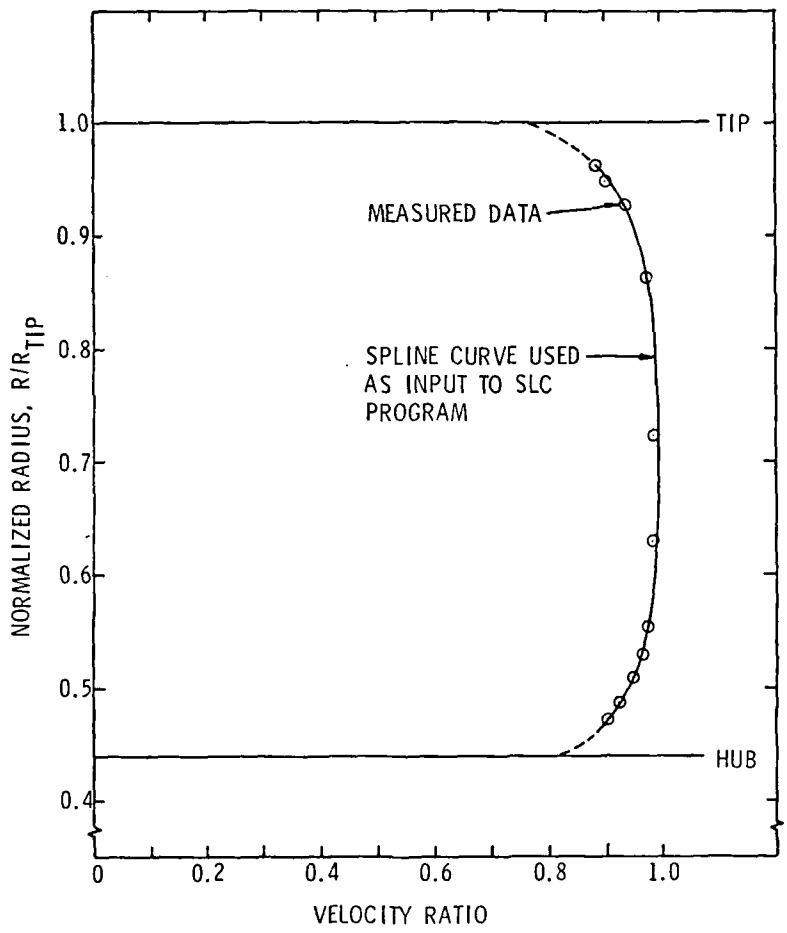

Figure 13. AFRF Measured Axial Velocity Profile at Rotor Inlet

boundary layer profile to obtain the first converged flow field solution. The rotor exit plane velocity ratios are plotted in Figure 14. Since this is merely an intermediate step in the complete analysis, little can be deduced from the information provided thus far. One important conclusion which can be drawn from Figure 14 is that the deviation angles computed from Howell's correlation method are not sufficient in themselves to yield an acceptable solution.

Once a converged flow field solution is obtained from Howell's correlation, the inlet and exit velocity distributions are used to calculate the primary flow deviation angles. The effects of blade camber, thickness, and axial accelerations are computed and tabulated in Table 4. Using these new relative flow angles, the SLC analysis code obtains a converged flow field solution which contains the losses due to the physical geometry of the test rotor. The results of this improved flow model are to lessen the over-prediction of the tangential component of total velocity that was observed in the previous solution. Because the tangential velocity profile is directly related to the rotor performance, it is desirable to predict this distribution as accurately as possible. It is true, however, that this profile is most difficult to obtain correctly due to its sensitivity to flow field changes. In comparison, the axial velocity distribution is much more docile and changes very little between successive runs. The results of including the primary flow deviation terms in the analysis are shown in Figure 15.

The next step toward obtaining the final flow field solution is the addition of the deviation term due to the generation of secondary vorticity. This calculation is based on the inlet normal vorticity

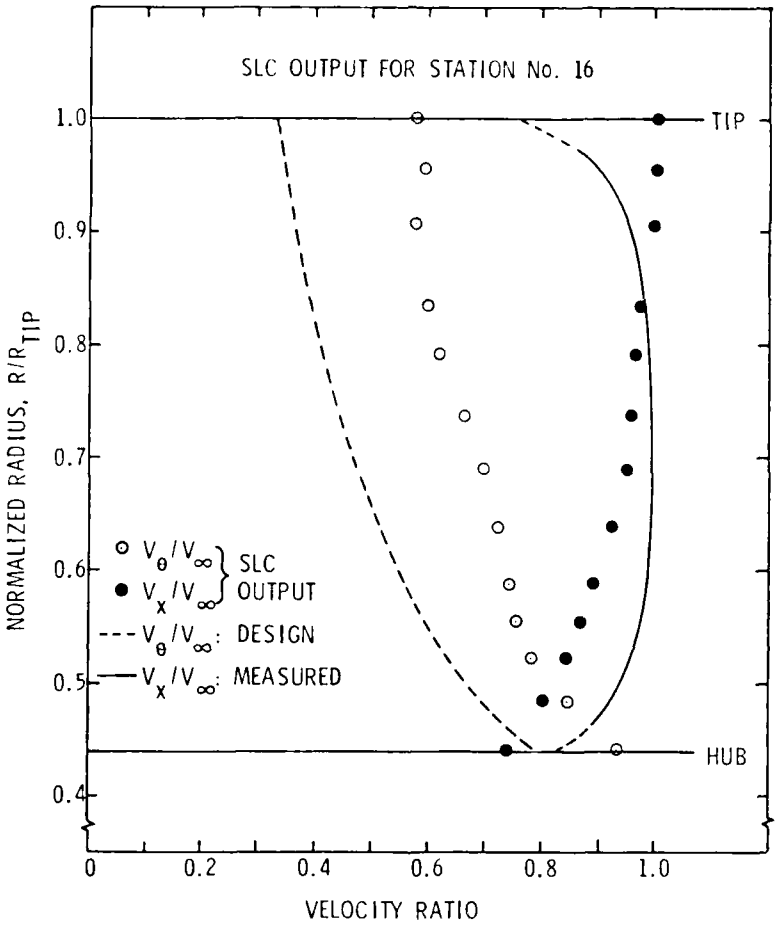

Figure 14. Streamline Curvature Exit Flow Field Based on Howell's Deviation Angles and Measured Inlet Axial Velocity Profile

Table 4. Primary Flow Deviation Angle Calculations - Measured Inlet Velocity Profile

SECTION NO.	β_2 (DEG)	$(K_\delta)_{sh}$	$(K_\delta)_t$	$(\delta_0{}^0)_{10}$ (DEG)	δ^* (DEG)	δ' (DEG)	m	ε_0 (DEG)	δ (DEG)	$\beta_2{}^*$ (DEG)
1	4.340	1.1	1.0	6.730	7.403	-0.550	0.186	1.933	9.886	14.226
2	19.020	1.1	1.0	4.699	5.169	-1.142	0.208	1.864	8.175	27.195
3	33.738	1.1	1.0	3.961	4.357	-0.641	0.249	1.930	6.928	40.666
4	44.273	1.1	1.0	2.765	3.042	-0.123	0.289	1.981	5.146	49.419
5	52.784	1.1	1.0	1.866	2.053	-0.135	0.331	1.926	4.114	56.898
6	57.550	1.1	1.0	1.551	1.706	1.560	0.371	1.978	2.124	59.674
7	60.089	1.1	1.0	1.234	1.358	1.872	0.388	2.010	1.496	61.585

$$\delta^* = (\delta_0{}^0)_{10} \cdot (K_\delta)_{sh} \cdot (K_\delta)_t$$

$$\delta_0 = m \cdot \theta_c$$

$$\delta = \delta_0 + \delta^* - \delta'$$

$$\beta_2{}^* = \beta_2 + \delta$$

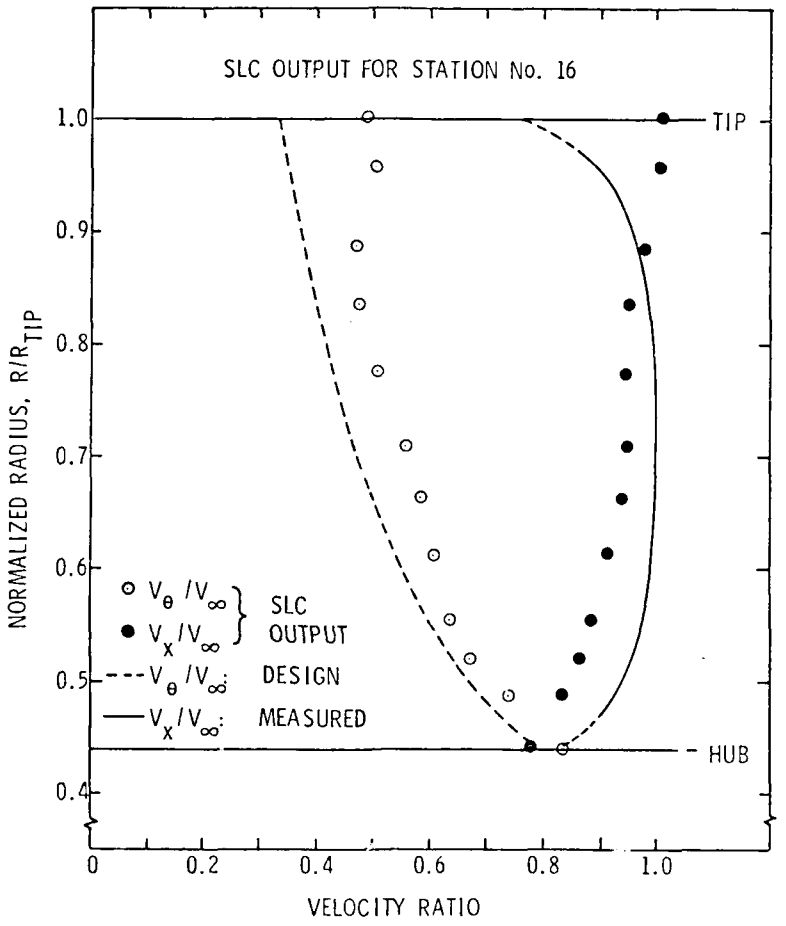

Figure 15. Streamline Curvature Exit Flow Field Based on Primary Flow Deviation Angles and Measured Inlet Axial Velocity Profile

profile which is computed from the inlet axial velocity distribution shown in Figure 13. This normal component of vorticity is defined as

$$\omega_n = \frac{d(V_x/V_\infty)}{d(R/R_{TIP})} \quad . \tag{29}$$

This normalized inlet vorticity profile and the resulting secondary flow deviation angles are provided in Table 5. The solution of the streamline curvature equations based on this new angularity distribution yields the exit velocity profiles found in Figure 16. From Equation (29), it can be seen that the uniform inlet velocity profile of the design case will not produce a normal vorticity component and hence, this step of the analysis was not included in the previous design analysis. Comparison of the three flow field solutions obtained thus far shows how, as better approximations of the flow losses are included in the analysis, the predicted velocity profiles approach the design and measured values.

The final correction term which is included in this hub-to-tip flow field analysis is due to the tip leakage flow phenomenon. If Equation (21) is substituted into Equation (19), the resulting equation clearly indicates two flow regions:

$$\delta_T = \tan^{-1}\left\{\frac{(1 - K)\, C_{L_T}\, c}{4\pi\, ar}\left[\frac{ar + \tau - y}{ar}\right]\right\}, \tag{30}$$

where the relationship between y and $ar + \tau$ is shown in Figure 17. From Figure 17 it can be seen that for a blade section at a distance from the casing of y_1, the deviation angle calculated from Equation (30) will add to the flow turning, while at a section of distance y_2 from

Table 5. Secondary Vorticity Deviation Angles - Measured Inlet Velocity Profile

SECTION NO.	β_2 (DEG)	δ_S (DEG)	δ (DEG)	β_2^* (DEG)	ω_n
1	4.340	-5.95	9.886	8.276	2.333
2	19.020	0.09	8.175	27.285	1.000
3	33.738	0.41	6.928	41.076	0.0
4	44.273	0.16	5.146	49.579	0.0
5	52.784	0.11	4.114	57.008	- 0.143
6	57.550	-0.26	2.124	59.414	- 1.313
7	60.089	-1.02	1.496	60.565	-13.000

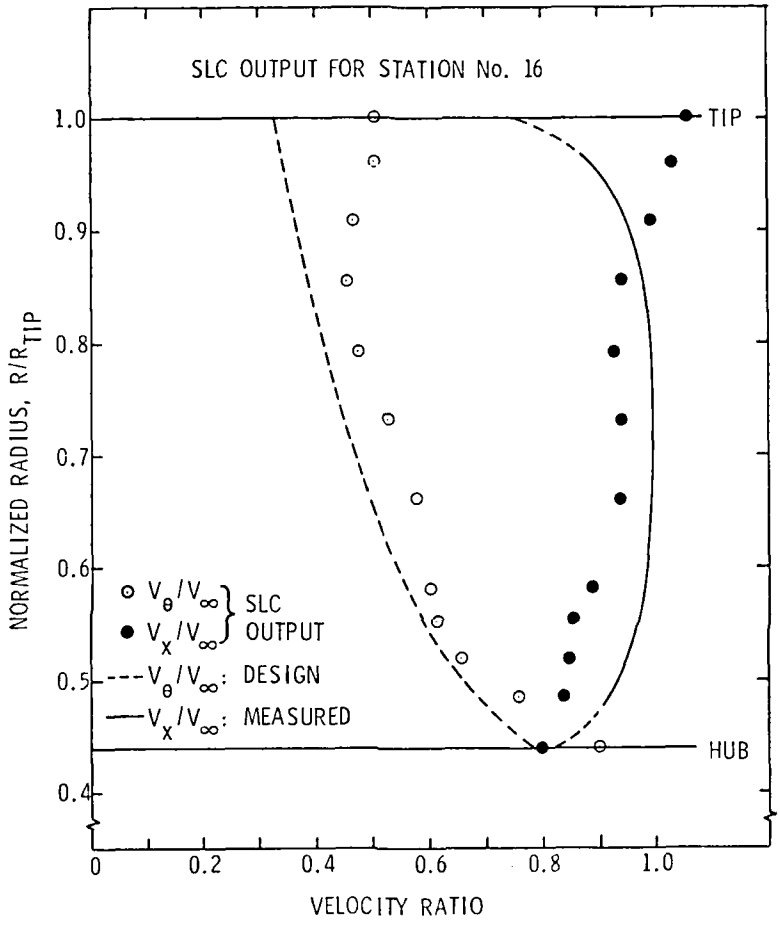

Figure 16. Streamline Curvature Exit Flow Field Based on Secondary Vorticity Deviation Angles and Measured Inlet Axial Velocity

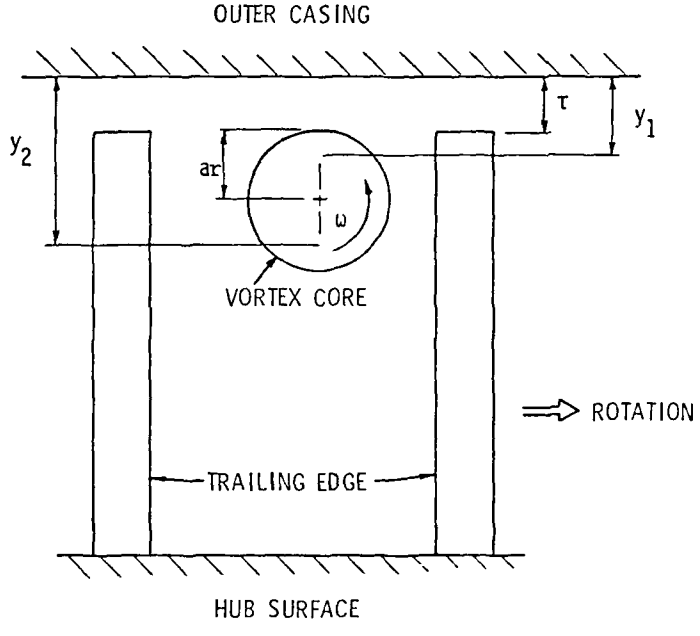

Figure 17. Tip Leakage Flow Vortex Model

the wall, the deviation will decrease the turning. Since only one blade section falls within the region of the vortex core, this is the only deviation angle which is modified by this calculation. The results as well as the specific values of the parameters used in Equation (30) are shown in Table 6.

The total deviation angle profile shown in Table 6 reflects the losses and effects of blade camber, thickness, axial accelerations, secondary vorticity, and tip leakage. This profile is used to obtain the final converged flow field solution from the SLC analysis program. The results of this final run are given in Figure 18. At first glance, Figure 18 appears to show that the SLC analysis method does not predict the flow field very well; this is not really the case. Figure 18 does not represent a comparison between predicted and measured velocity profiles. What it does represent is the comparison between predicted and design values of tangential velocity. In this respect, one would expect to see the test rotor perform very close to its design specification. The comparison of axial velocity, however, is not as straightforward. The profile which has been referred to as the "measured" axial velocity is not measured at the blade exit station. At this point, the assumption has been made that, for this free vortex loading distribution of the test rotor, there is no axial acceleration through the blade row. For this reason, and the lack of an exit axial velocity profile, the measured inlet axial velocity profile is used as a base of comparison. Thus, the SLC predictions are indicating that the trailing-edge axial velocity profile is somewhat different than the inlet profile. The comparison of SLC predictions and actual

Table 6. Tip Leakage Deviation Angles - Measured Inlet Axial Velocity Profile

SECTION NO.	β_2 (DEG)	δ_T (DEG)	δ_S (DEG)	δ (DEG)	δ_{TOT} (DEG)	β_2^* (DEG)
1	4.340	-	-5.95	9.886	3.936	8.276
2	19.020	-	0.09	8.175	8.265	27.286
3	33.738	-	0.41	6.928	7.332	41.076
4	44.273	-	0.16	5.146	5.306	49.579
5	52.784	-	0.11	4.114	4.324	57.008
6	57.550	-	-0.26	2.124	1.864	59.414
7	60.089	11.03	-1.02	1.496	12.176	71.600

C_{L_T} = 0.369

d = 15.24 cm

τ = 0.254 cm

S = 19.05 cm

y_6 = 1.524 cm (OUTSIDE VORTEX CORE)

y_7 = 0.254 cm

ar = 0.7557 cm

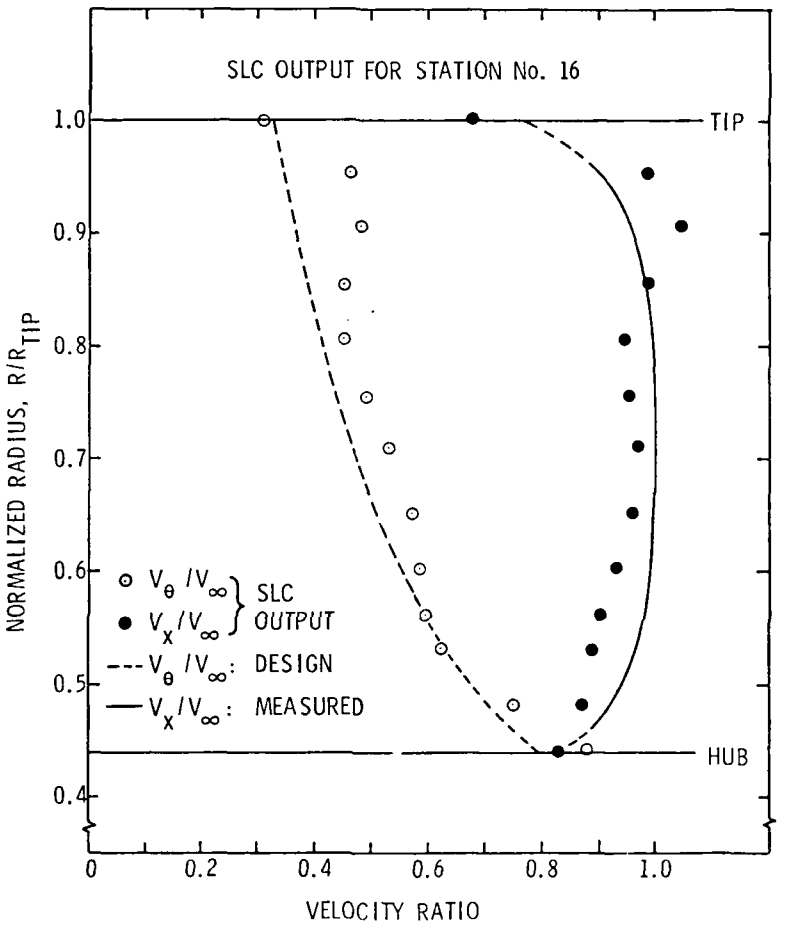

Figure 18. Streamline Curvature Exit Flow Field Based on Total Deviation Angles and Measured Inlet Axial Velocity

measured exit flow conditions are presented following the experimental phase of the investigation.

3.2 The Blade-to-Blade Analysis

The solution of the flow field on the S_1 surface involves the use of both the streamline curvature blade-to-blade computer program and the Douglas-Neumann (D-N) source analysis program. Both of these analytic methods require the blade section coordinates as input. Figure 19 is a computer-drawn representation of the seven cylindrical blade sections of the AFRF test rotor. The 82 points that are used to define each blade section are connected by straight line segments similar to the numerical scheme of the Douglas-Neumann analysis. This large number of body points provides a good definition of the section geometry, as well as increasing the accuracy of the integration technique used in the D-N analysis. The streamline curvature method requires not only the section coordinates, but also an initial approximation of the upstream and downstream flow angles. The flow field boundaries are calculated from the SLC hub-to-tip axisymmetric solution already obtained. The initial flow field boundaries for each of the seven sections are shown in Figures 20 through 26. These plots indicate the physical position of the blade section relative to the axial direction, as well as the calculation stations positioned throughout the flow field. These initial flow boundaries are adjusted, based on the periodicity condition as the SLC procedure converges to the correct solution. Tables 7 through 13 provide the actual coordinates of each station line in the problem, as well as the specific inlet and exit flow angles used for each section.

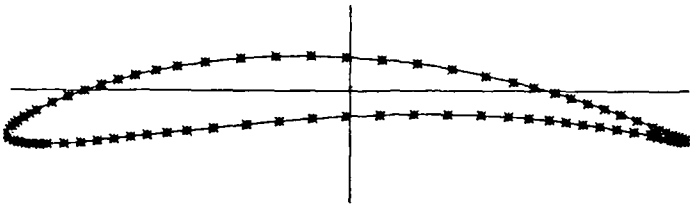

BLADE SECTION NO. 1

STAGGER ANGLE = 23.140 deg

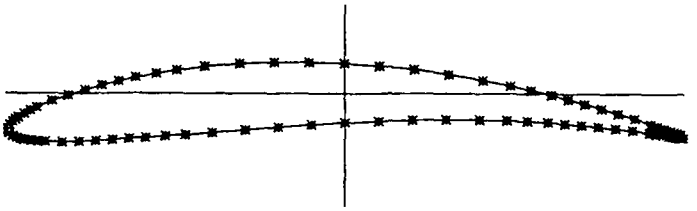

BLADE SECTION NO. 2

STAGGER ANGLE = 31.020 deg

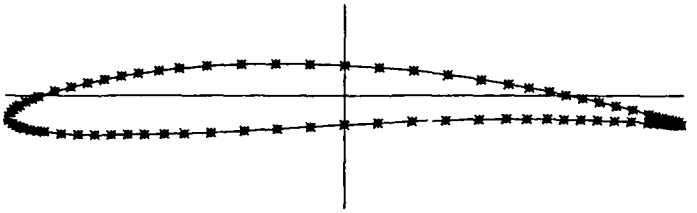

BLADE SECTION NO. 3

STAGGER ANGLE = 42.438 deg

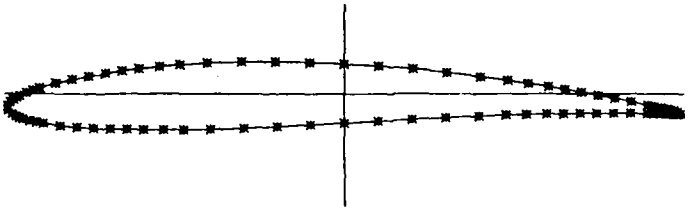

BLADE SECTION NO. 4

STAGGER ANGLE = 50.273 deg

Figure 19. Points Defining Blade Sections of AFRF Test Rotor

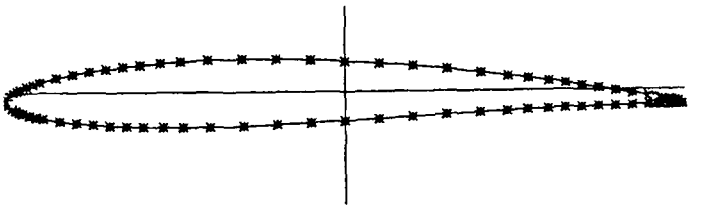

BLADE SECTION NO. 5

STAGGER ANGLE = 55.784 deg

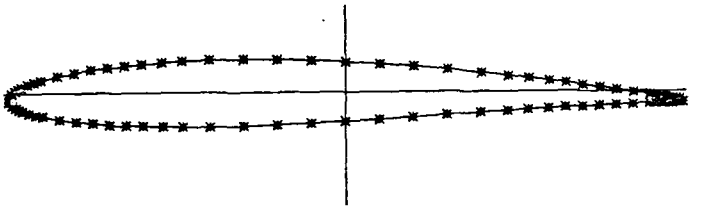

BLADE SECTION NO. 6

STAGGER ANGLE = 59.850 deg

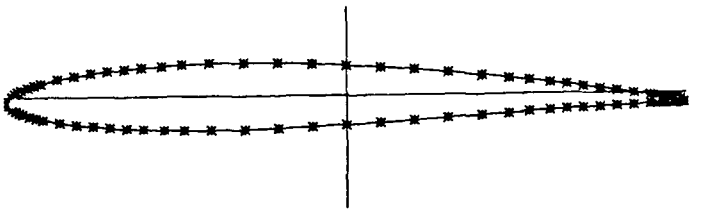

BLADE SECTION NO. 7

STAGGER ANGLE = 61.589 deg

Figure 19. (Continued)

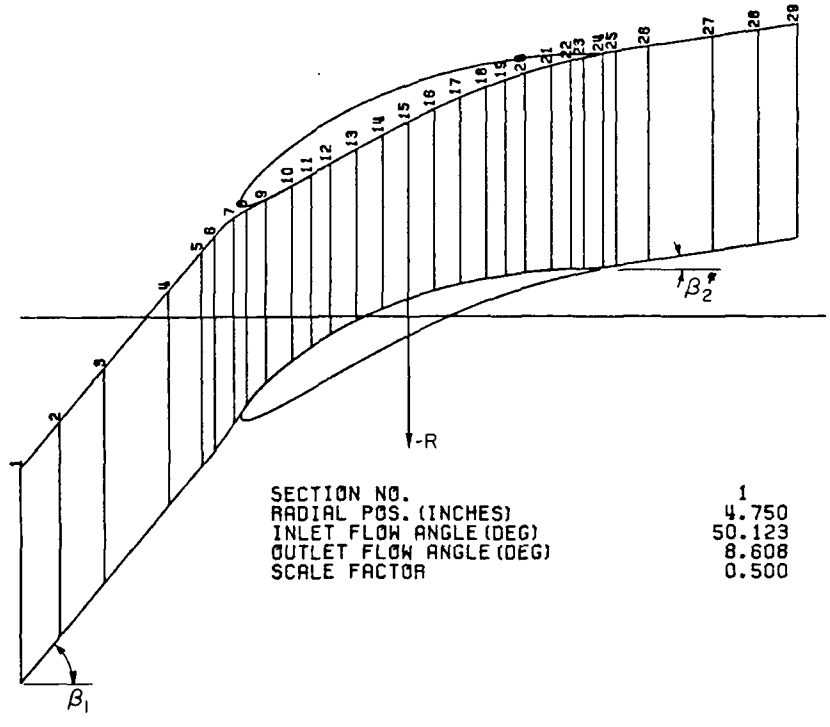

Figure 20. Streamline Curvature Initial Flow Boundaries - Section No. 1

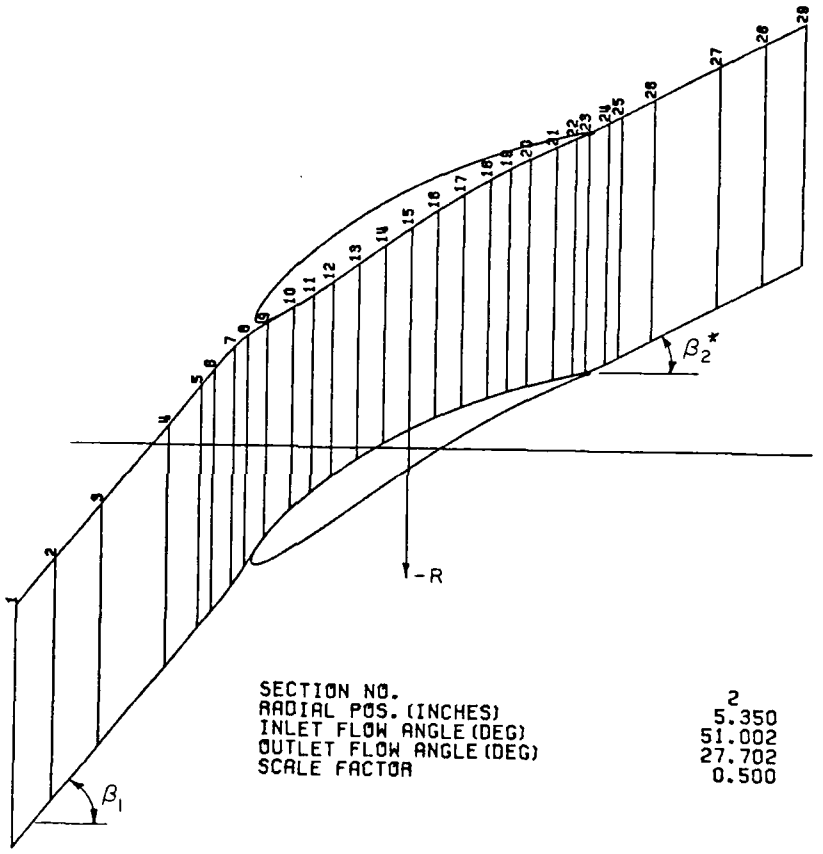

Figure 21. Streamline Curvature Initial Flow Boundaries - Section No. 2

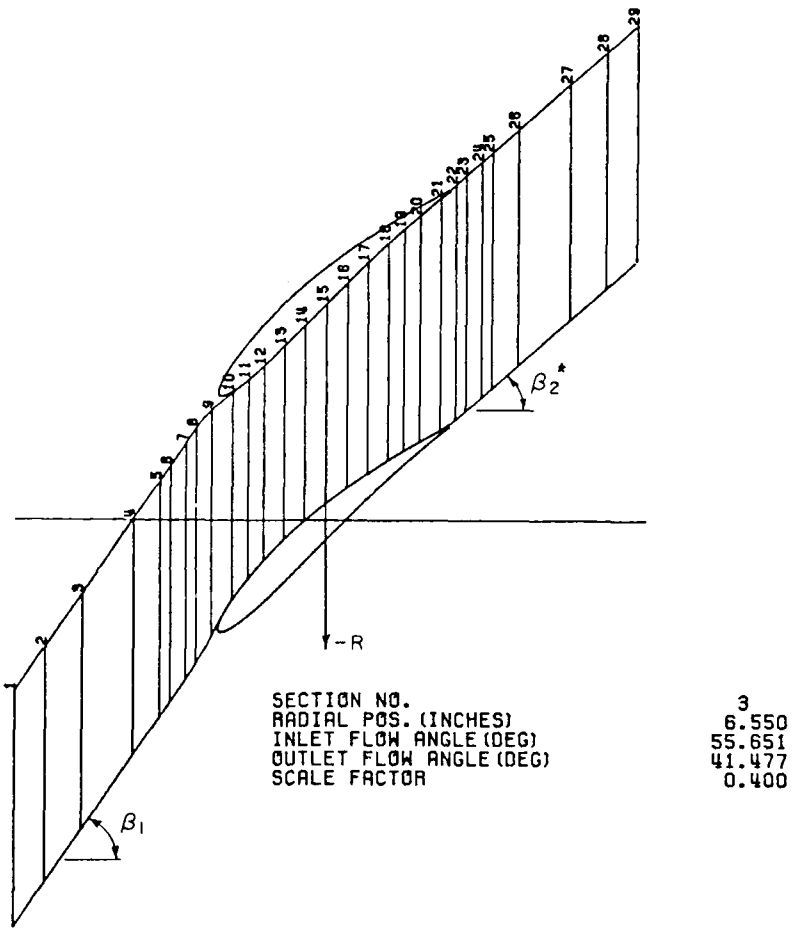

Figure 22. Streamline Curvature Initial Flow Boundaries - Section No. 3

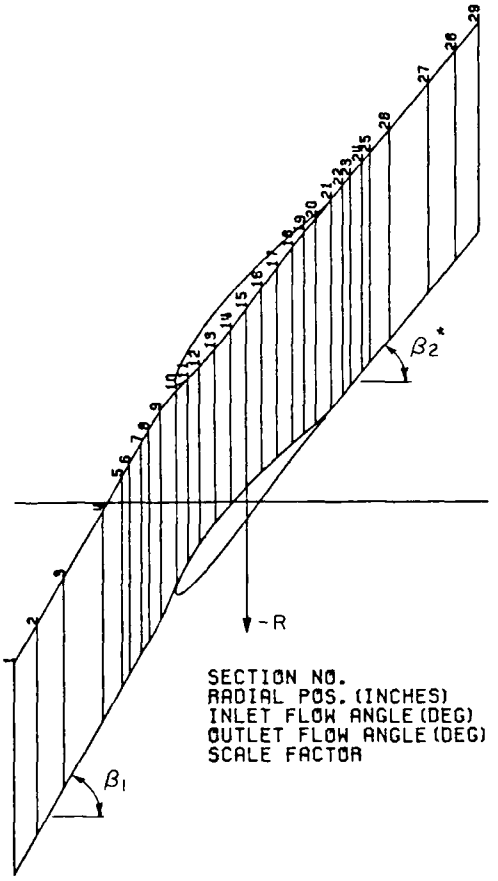

Figure 23. Streamline Curvature Initial Flow Boundaries - Section No. 4

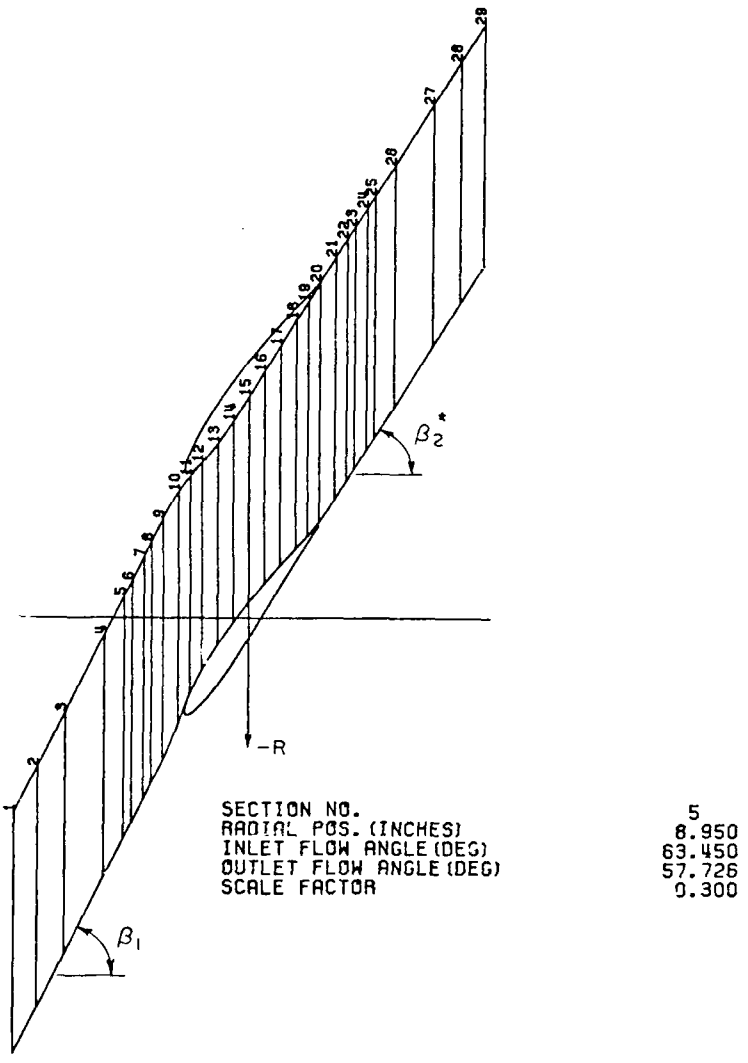

Figure 24. Streamline Curvature Initial Flow Boundaries - Section No. 5

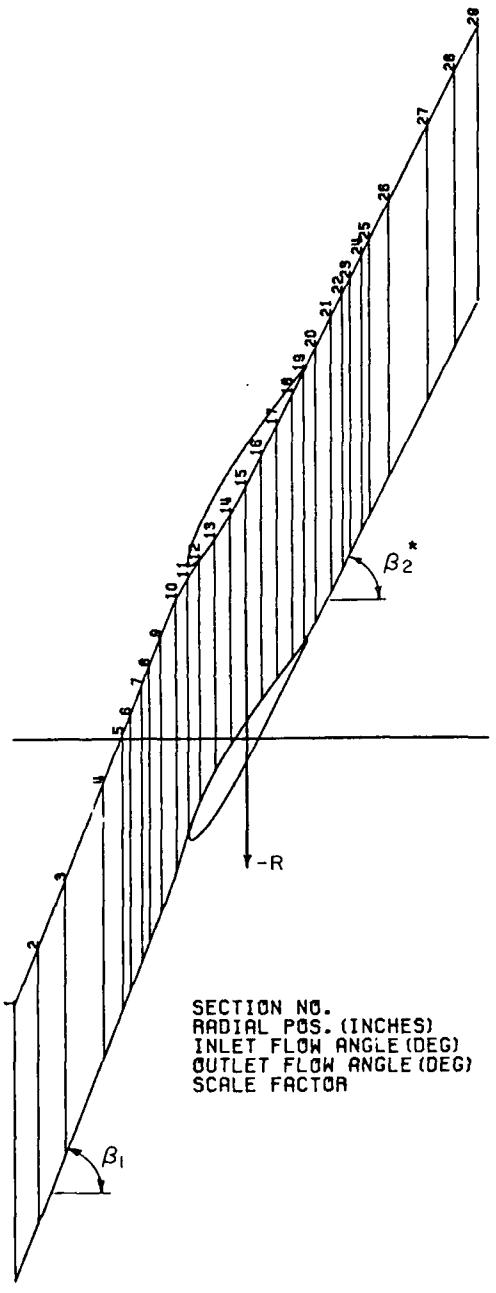

SECTION NO.	6
RADIAL POS. (INCHES)	10.150
INLET FLOW ANGLE (DEG)	68.300
OUTLET FLOW ANGLE (DEG)	63.193
SCALE FACTOR	0.300

Figure 25. Streamline Curvature Initial Flow Boundaries - Section No. 6

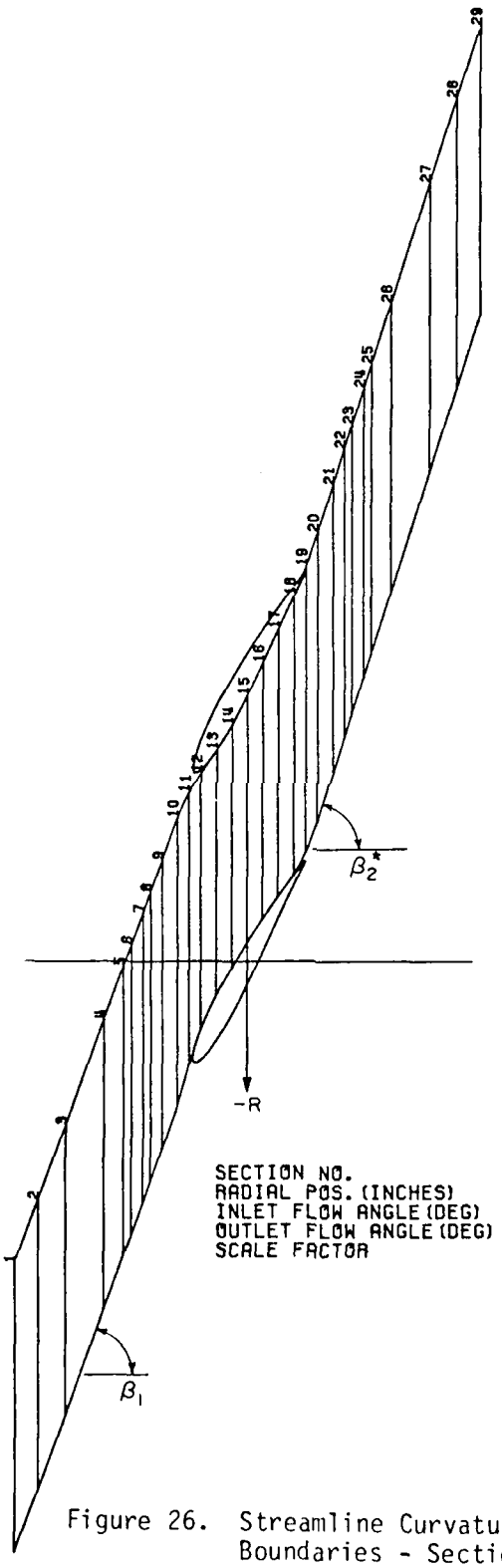

SECTION NO.	7
RADIAL POS. (INCHES)	10.750
INLET FLOW ANGLE (DEG)	70.011
OUTLET FLOW ANGLE (DEG)	72.261
SCALE FACTOR	0.300

Figure 26. Streamline Curvature Initial Flow Boundaries - Section No. 7

Table 7. SLC Calculating Station Coordinates - Section No. 1

SECTION NO.	1
RADIAL POS. (INCHES)	4.750
INLET FLOW ANGLE (DEG)	50.123
OUTLET FLOW ANGLE (DEG)	8.608
SCALE FACTOR	0.500

STAT.NO.	X-INNER	Y-INNER	X-OUTER	Y-OUTER
1	-6.000	-5.657	-6.000	-2.341
2	-5.400	-4.939	-5.400	-1.623
3	-4.700	-4.101	-4.700	-0.785
4	-3.700	-2.904	-3.700	0.412
5	-3.200	-2.305	-3.200	1.010
6	-3.000	-2.069	-3.000	1.253
7	-2.700	-1.650	-2.700	1.539
8	-2.500	-1.356	-2.500	1.667
9	-2.200	-1.015	-2.200	1.819
10	-1.800	-0.675	-1.800	2.032
11	-1.500	-0.458	-1.500	2.201
12	-1.200	-0.268	-1.200	2.370
13	-0.800	-0.055	-0.800	2.594
14	-0.400	0.125	-0.400	2.815
15	0.000	0.278	0.000	3.024
16	0.400	0.407	0.400	3.217
17	0.800	0.512	0.800	3.394
18	1.200	0.595	1.200	3.557
19	1.500	0.646	1.500	3.666
20	1.800	0.687	1.800	3.764
21	2.200	0.726	2.200	3.880
22	2.500	0.740	2.500	3.961
23	2.700	0.747	2.700	4.011
24	3.000	0.767	3.000	4.076
25	3.200	0.793	3.200	4.110
26	3.700	0.869	3.700	4.185
27	4.700	1.020	4.700	4.336
28	5.400	1.126	5.400	4.442
29	6.000	1.217	6.000	4.533

Table 8. SLC Calculating Station Coordinates - Section No. 2

SECTION NO.	2
RADIAL POS. (INCHES)	5.350
INLET FLOW ANGLE (DEG)	51.002
OUTLET FLOW ANGLE (DEG)	27.702
SCALE FACTOR	0.500

STAT.NO.	X-INNER	Y-INNER	X-OUTER	Y-OUTER
1	-6.000	-6.270	-6.000	-2.535
2	-5.400	-5.530	-5.400	-1.795
3	-4.700	-4.665	-4.700	-0.930
4	-3.700	-3.430	-3.700	0.305
5	-3.200	-2.813	-3.200	0.923
6	-3.000	-2.565	-3.000	1.169
7	-2.700	-2.182	-2.700	1.529
8	-2.500	-1.866	-2.500	1.709
9	-2.200	-1.408	-2.200	1.909
10	-1.800	-0.968	-1.800	2.152
11	-1.500	-0.694	-1.500	2.355
12	-1.200	-0.448	-1.200	2.565
13	-0.800	-0.167	-0.800	2.847
14	-0.400	0.078	-0.400	3.136
15	0.000	0.295	0.000	3.418
16	0.400	0.488	0.400	3.686
17	0.800	0.656	0.800	3.941
18	1.200	0.804	1.200	4.182
19	1.500	0.905	1.500	4.349
20	1.800	0.996	1.800	4.506
21	2.200	1.100	2.200	4.700
22	2.500	1.169	2.500	4.842
23	2.700	1.227	2.700	4.938
24	3.000	1.354	3.000	5.090
25	3.200	1.461	3.200	5.195
26	3.700	1.723	3.700	5.458
27	4.700	2.248	4.700	5.983
28	5.400	2.615	5.400	6.350
29	6.000	2.930	6.000	6.665

Table 9. SLC Calculating Station Coordinates - Section No. 3

SECTION NO.	3
RADIAL POS. (INCHES)	6.550
INLET FLOW ANGLE (DEG)	55.651
OUTLET FLOW ANGLE (DEG)	41.477
SCALE FACTOR	0.400

STAT.NO.	X-INNER	Y-INNER	X-OUTER	Y-OUTER
1	-6.000	-7.899	-6.000	-3.327
2	-5.400	-7.021	-5.400	-2.449
3	-4.700	-5.997	-4.700	-1.424
4	-3.700	-4.534	-3.700	0.039
5	-3.200	-3.802	-3.200	0.770
6	-3.000	-3.510	-3.000	1.063
7	-2.700	-3.070	-2.700	1.502
8	-2.500	-2.780	-2.500	1.796
9	-2.200	-2.230	-2.200	2.148
10	-1.800	-1.522	-1.800	2.489
11	-1.500	-1.120	-1.500	2.732
12	-1.200	-0.767	-1.200	3.001
13	-0.800	-0.356	-0.800	3.363
14	-0.400	0.006	-0.400	3.785
15	0.000	0.336	0.000	4.198
16	0.400	0.639	0.400	4.604
17	0.800	0.916	0.800	5.002
18	1.200	1.175	1.200	5.385
19	1.500	1.358	1.500	5.658
20	1.800	1.530	1.800	5.920
21	2.200	1.754	2.200	6.265
22	2.500	1.959	2.500	6.527
23	2.700	2.130	2.700	6.703
24	3.000	2.396	3.000	6.969
25	3.200	2.573	3.200	7.145
26	3.700	3.015	3.700	7.588
27	4.700	3.899	4.700	8.472
28	5.400	4.518	5.400	9.090
29	6.000	5.048	6.000	9.621

Table 10. SLC Calculating Station Coordinates - Section No. 4

SECTION NO.	4
RADIAL POS. (INCHES)	7.750
INLET FLOW ANGLE (DEG)	59.934
OUTLET FLOW ANGLE (DEG)	50.185
SCALE FACTOR	0.300

STAT.NO.	X-INNER	Y-INNER	X-OUTER	Y-OUTER
1	-6.000	-9.592	-6.000	-4.181
2	-5.400	-8.555	-5.400	-3.145
3	-4.700	-7.346	-4.700	-1.936
4	-3.700	-5.619	-3.700	-0.208
5	-3.200	-4.755	-3.200	0.656
6	-3.000	-4.409	-3.000	1.001
7	-2.700	-3.891	-2.700	1.519
8	-2.500	-3.545	-2.500	1.864
9	-2.200	-3.014	-2.200	2.375
10	-1.800	-2.108	-1.800	2.881
11	-1.500	-1.528	-1.500	3.182
12	-1.200	-1.060	-1.200	3.487
13	-0.800	-0.521	-0.800	3.944
14	-0.400	-0.051	-0.400	4.439
15	0.000	0.382	0.000	4.972
16	0.400	0.782	0.400	5.509
17	0.800	1.155	0.800	6.044
18	1.200	1.509	1.200	6.565
19	1.500	1.763	1.500	6.939
20	1.800	2.013	1.800	7.309
21	2.200	2.397	2.200	7.803
22	2.500	2.753	2.500	8.163
23	2.700	2.993	2.700	8.403
24	3.000	3.353	3.000	8.763
25	3.200	3.593	3.200	9.003
26	3.700	4.192	3.700	9.603
27	4.700	5.392	4.700	10.803
28	5.400	6.232	5.400	11.642
29	6.000	6.952	6.000	12.362

Table 11. SLC Calculating Station Coordinates - Section No. 5

SECTION NO.	5
RADIAL POS. (INCHES)	8.950
INLET FLOW ANGLE (DEG)	63.450
OUTLET FLOW ANGLE (DEG)	57.726
SCALE FACTOR	0.300

STAT.NO.	X-INNER	Y-INNER	X-OUTER	Y-OUTER
1	-6.000	-11.275	-6.000	-5.027
2	-5.400	-10.074	-5.400	-3.826
3	-4.700	-8.673	-4.700	-2.425
4	-3.700	-6.672	-3.700	-0.424
5	-3.200	-5.671	-3.200	0.577
6	-3.000	-5.271	-3.000	0.977
7	-2.700	-4.671	-2.700	1.578
8	-2.500	-4.270	-2.500	1.978
9	-2.200	-3.677	-2.200	2.583
10	-1.800	-2.725	-1.800	3.283
11	-1.500	-1.944	-1.500	3.678
12	-1.200	-1.337	-1.200	4.027
13	-0.800	-0.668	-0.800	4.534
14	-0.400	-0.098	-0.400	5.106
15	0.000	0.427	0.000	5.744
16	0.400	0.914	0.400	6.404
17	0.800	1.372	0.800	7.075
18	1.200	1.811	1.200	7.730
19	1.500	2.134	1.500	8.208
20	1.800	2.492	1.800	8.696
21	2.200	3.087	2.200	9.336
22	2.500	3.563	2.500	9.811
23	2.700	3.879	2.700	10.128
24	3.000	4.354	3.000	10.603
25	3.200	4.671	3.200	10.919
26	3.700	5.463	3.700	11.711
27	4.700	7.046	4.700	13.295
28	5.400	8.155	5.400	14.403
29	6.000	9.105	6.000	15.353

Table 12. SLC Calculating Station Coordinates - Section No. 6

SECTION NO.	6
RADIAL POS. (INCHES)	10.150
INLET FLOW ANGLE (DEG)	68.300
OUTLET FLOW ANGLE (DEG)	63.193
SCALE FACTOR	0.300

STAT.NO.	X-INNER	Y-INNER	X-OUTER	Y-OUTER
1	-6.000	-14.012	-6.000	-6.926
2	-5.400	-12.504	-5.400	-5.418
3	-4.700	-10.745	-4.700	-3.659
4	-3.700	-8.232	-3.700	-1.146
5	-3.200	-6.976	-3.200	0.110
6	-3.000	-6.473	-3.000	0.613
7	-2.700	-5.719	-2.700	1.367
8	-2.500	-5.218	-2.500	1.870
9	-2.200	-4.461	-2.200	2.622
10	-1.800	-3.393	-1.800	3.591
11	-1.500	-2.413	-1.500	4.149
12	-1.200	-1.607	-1.200	4.599
13	-0.800	-0.804	-0.800	5.149
14	-0.400	-0.138	-0.400	5.786
15	0.000	0.472	0.000	6.515
16	0.400	1.035	0.400	7.295
17	0.800	1.571	0.800	8.099
18	1.200	2.089	1.200	8.887
19	1.500	2.506	1.500	9.484
20	1.800	3.007	1.800	10.092
21	2.200	3.798	2.200	10.883
22	2.500	4.391	2.500	11.477
23	2.700	4.787	2.700	11.873
24	3.000	5.381	3.000	12.467
25	3.200	5.777	3.200	12.863
26	3.700	6.766	3.700	13.852
27	4.700	8.745	4.700	15.831
28	5.400	10.131	5.400	17.217
29	6.000	11.318	6.000	18.404

Table 13. SLC Calculating Station Coordinates - Section No. 7

SECTION NO.	7
RADIAL POS. (INCHES)	10.750
INLET FLOW ANGLE (DEG)	70.011
OUTLET FLOW ANGLE (DEG)	72.261
SCALE FACTOR	0.300

STAT.NO.	X-INNER	Y-INNER	X-OUTER	Y-OUTER
1	-6.000	-15.317	-6.000	-7.812
2	-5.400	-13.667	-5.400	-6.162
3	-4.700	-11.743	-4.700	-4.238
4	-3.700	-8.994	-3.700	-1.489
5	-3.200	-7.619	-3.200	-0.114
6	-3.000	-7.069	-3.000	0.436
7	-2.700	-6.244	-2.700	1.260
8	-2.500	-5.695	-2.500	1.811
9	-2.200	-4.867	-2.200	2.633
10	-1.800	-3.739	-1.800	3.718
11	-1.500	-2.680	-1.500	4.367
12	-1.200	-1.752	-1.200	4.861
13	-0.800	-0.872	-0.800	5.462
14	-0.400	-0.157	-0.400	6.126
15	0.000	0.494	0.000	6.899
16	0.400	1.096	0.400	7.740
17	0.800	1.670	0.800	8.615
18	1.200	2.243	1.200	9.477
19	1.500	2.805	1.500	10.226
20	1.800	3.600	1.800	11.112
21	2.200	4.861	2.200	12.366
22	2.500	5.799	2.500	13.303
23	2.700	6.424	2.700	13.929
24	3.000	7.362	3.000	14.866
25	3.200	7.987	3.200	15.492
26	3.700	9.550	3.700	17.055
27	4.700	12.676	4.700	20.181
28	5.400	14.864	5.400	22.369
29	6.000	16.740	6.000	24.245

The results of the two blade-to-blade analyses are shown in Figures 27 through 33 in the form of a surface static pressure coefficient plotted as a function of section chord length. A comparison of the data for the first section seems to indicate fairly close agreement on the latter half of the blade and some difficulties in the region of the leading-edge, especially on the suction surface. This is possibly due to the leading-edge cusp which exists in the SLC analysis due to a smoothing of the flow boundary in this area. The differences between these two analytic methods become increasingly pronounced as subsequent sections, at higher stagger angles, are studied. From the data trend, it appears that some computational irregularity exists in the streamline curvature technique used for this blade-to-blade investigation. The Douglas-Neumann results exhibit a consistent trend from section to section with only changes in the absolute magnitudes. Such a tendency appears to be reasonable since all the blade sections have the same basic thickness distribution, but differ with respect to the total amount of fluid turning. One of the parameters that is computed by the Douglas-Neumann analysis is the fluid turning angle ($\Delta\beta$). A comparison between these computed values and the design values is provided in Table 14. The inviscid Douglas-Neumann source analysis, except for the hub section, overpredicts the amount of total turning at each radial blade section. This overprediction is caused by the inviscid nature of the coding and the use of empirical correlations, which account for some of the viscous effects, to determine the design values.

The results of the SLC blade-to-blade analysis indicate that although the method fails to agree with the Douglas-Neumann cascade

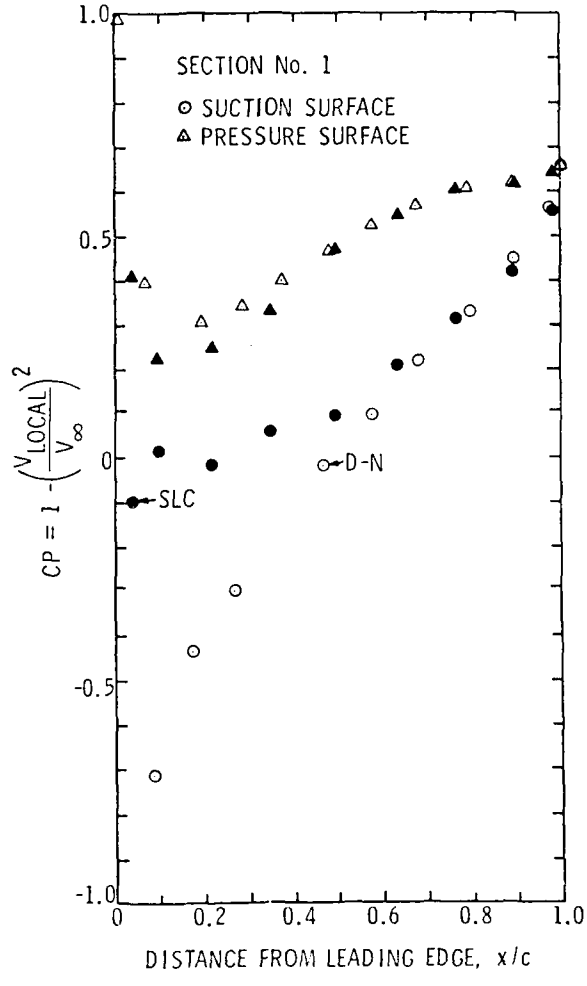

Figure 27. Comparison of Douglas-Neumann (D-N) and Streamline Curvature (SLC) Surface Pressure Distributions - Section No. 1

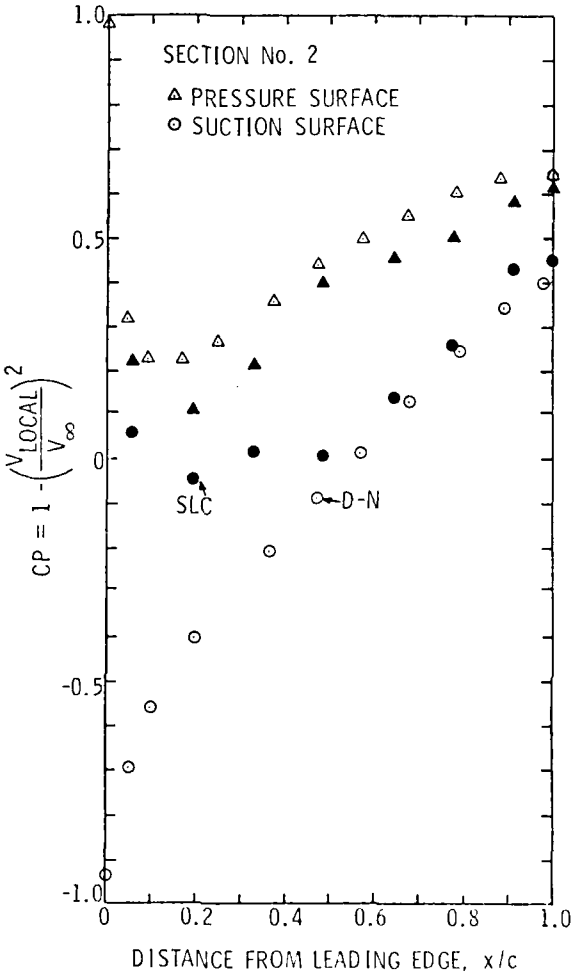

Figure 28. Comparison of Douglas-Neumann (D-N) and Streamline Curvature (SLC) Surface Pressure Distributions - Section No. 2

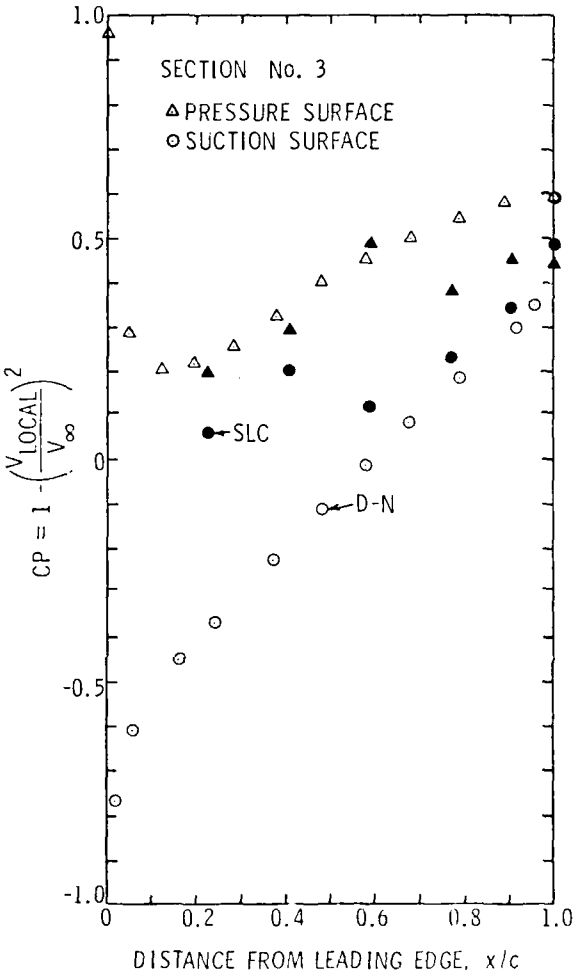

Figure 29. Comparison of Douglas-Neumann (D-N) and Streamline Curvature (SLC) Surface Pressure Distributions - Section No. 3

AD-A094 422 PENNSYLVANIA STATE UNIV UNIVERSITY PARK APPLIED RESE--ETC F/G 20/4
EXPERIMENTAL VERIFICATION OF THE STREAMLINE CURVATURE NUMERICAL--ETC(U)
MAY 80 M J PIERZGA N00024-79-C-6043
UNCLASSIFIED ARL/PSU/TM-80-181 NL

2 OF 3
AD A094422

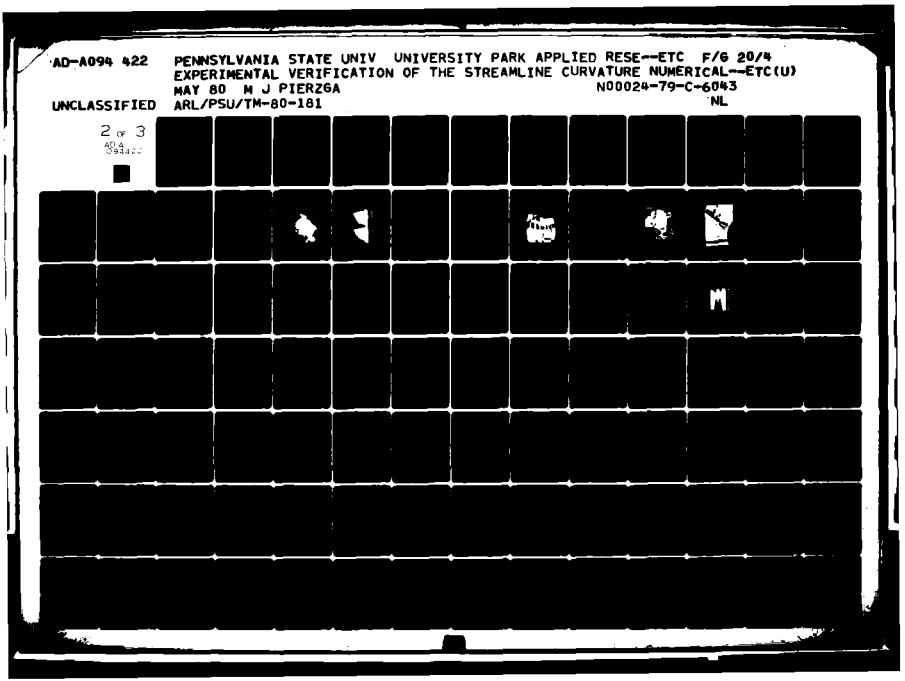

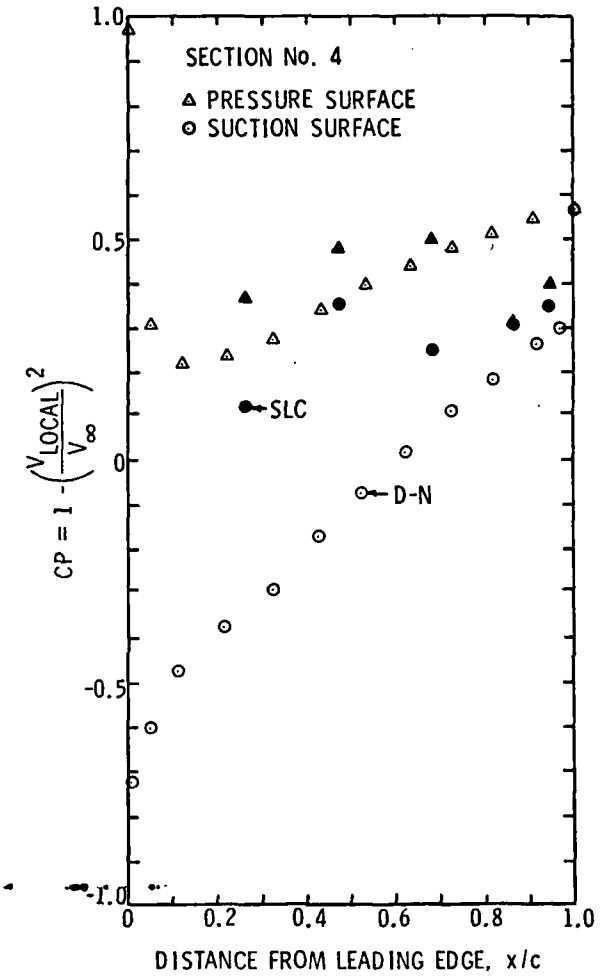

Figure 30. Comparison of Douglas-Neumann (D-N) and Streamline Curvature (SLC) Surface Pressure Distributions - Section No. 4

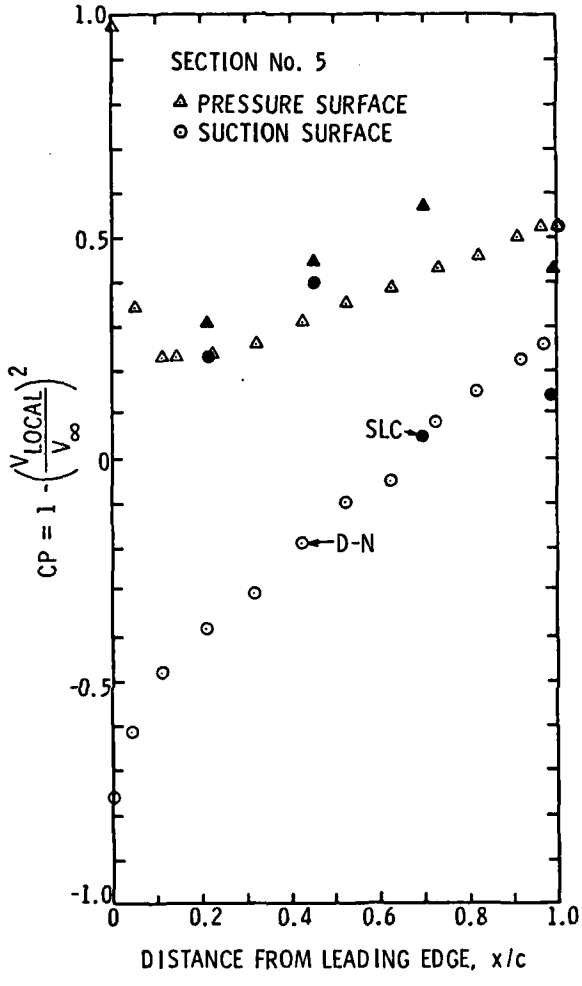

Figure 31. Comparison of Douglas-Neumann (D-N) and Streamline Curvature (SLC) Surface Pressure Distributions - Section No. 5

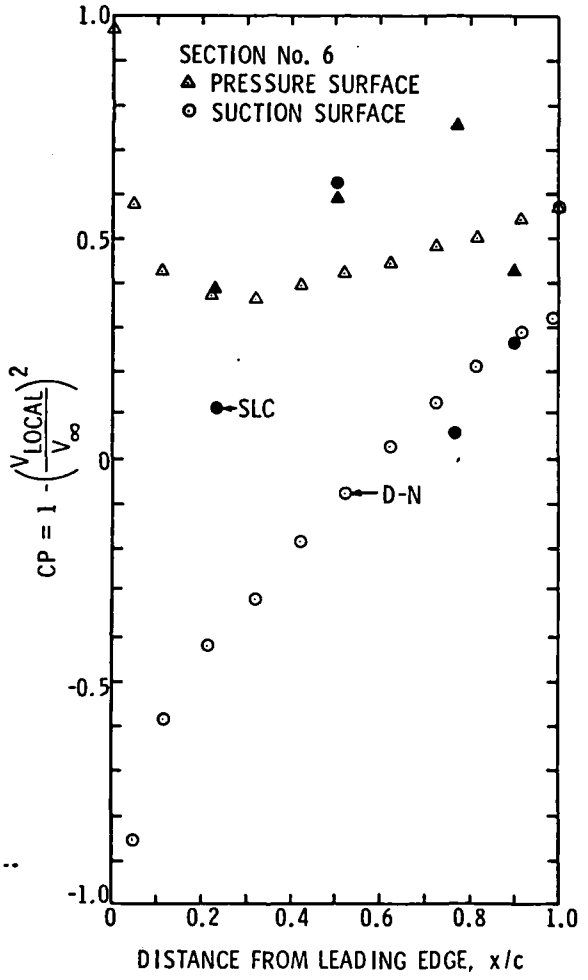

Figure 32. Comparison of Douglas-Neumann (D-N) and Streamline Curvature (SLC) Surface Pressure Distributions - Section No. 6

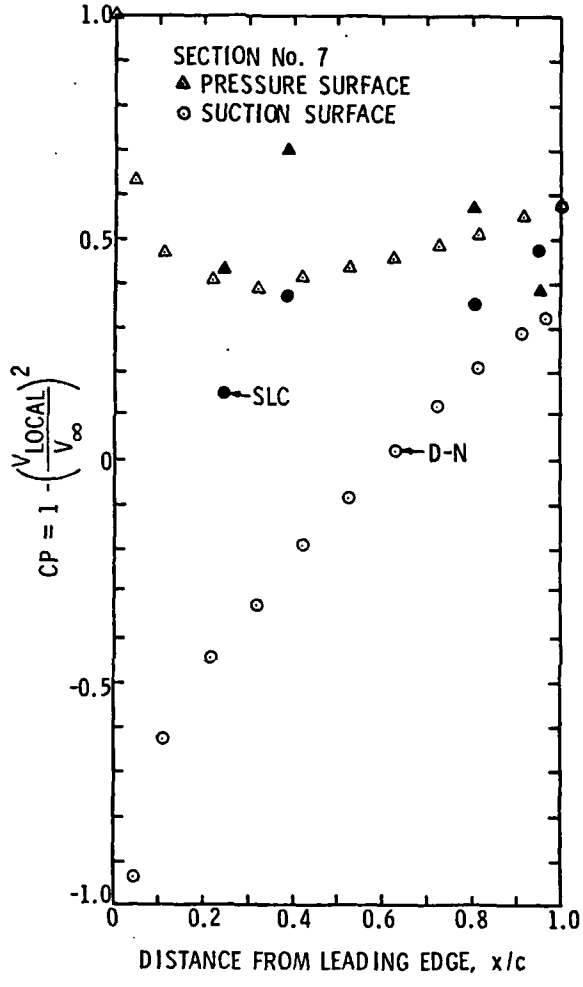

Figure 33. Comparison of Douglas-Neumann (D-N) and Streamline Curvature (SLC) Surface Pressure Distributions - Section No. 7

Table 14. Total Turning Angles Across Cascades

SECTION NO.	RADIAL POSITION (cm)	D-N ($\Delta\beta$)	DESIGN VALUE ($\Delta\beta$)
1	12.065	38.81°	39.8°
2	13.589	31.54°	24.8°
3	16.637	19.46°	17.5°
4	19.685	12.88°	10.5°
5	22.733	9.20°	6.2°
6	25.781	8.76°	4.6°
7	27.305	8.20°	3.5°

results, the SLC method may still be useful. The tendency of the predictions to diverge as the blade stagger angle becomes larger may mean that the error is associated with program geometry rather than program coding. If this is the case, the analysis would require only minor modifications to be an effective analysis tool. The reason for the attempt to convert the hub-to-tip analysis code to a blade-to-blade code is to obtain the streamlines and thus velocity distributions in the channel region. This type of information is not provided by the Douglas-Neumann analysis.

4. EXPERIMENTAL INVESTIGATION OF FLOW FIELD

4.1 Introduction

In order to verify the accuracy of the streamline curvature numerical analysis method, a number of experimental investigations were conducted. The first set of measurements consisted of spanwise flow surveys conducted at locations upstream and downstream of the AFRF test rotor. These data provide the overall machine performance by obtaining the stationary inlet and exit flow field. The second phase of the investigation deals with the design and manufacturing of a rotating traversing mechanism which allows the blade-to-blade flow field to be measured while the test rotor is operating. These intra-blade flow measurements are important to the improvement of the overall design capabilities of the turbomachine designer. Lastly, the static pressures on the rotating blade surfaces are measured for comparison with the two-dimensional cascade data. The results of such an experimental verification program provides a one-to-one correlation between the analytic and experimental phases of the entire study.

The major emphasis of this investigation is to establish the procedures and hardware necessary to conduct detailed flow field surveys for the purpose of verification and modification of existing design methods. The study conducted does not intend to completely verify the accuracy of the streamline curvature analysis method and further study along those lines is needed. Subsequent studies, however, should be able to use the hardware along with the computer codes developed thus far to conduct the more intensive flow field studies which are needed.

4.2 The Axial Flow Research Fan (AFRF) Test Facility

The experimental work for this investigation was conducted using the Axial Flow Research Fan (AFRF), a facility of the Garfield Thomas Water Tunnel which is located at The Pennsylvania State University. This facility, shown in Figure 34, consists of an annular flow passage bounded at one end by a bellmouth inlet and the other end by an exhaust throttle. The design of the AFRF facility provides uniform inlet flow and allows for a variety of operating conditions with the use of two separate drive motor assemblies. A 52.199 killowatt (70 Horsepower) motor is housed inside the centerbody of the facility and controls the speed of the test rotor. The auxiliary motor drives an Axivane fan at the rear of the facility which sets the tunnel through-flow velocity. The adjustment of either or both of these motors permits flow conditions of design and off-design incidence. Both drive motors are operated independently through the use of two Borg-Warner solid-state adjustable frequency drive inverter units that can produce rotational speeds of up to 3400 RPM.

The entire test facility rests on a system of movable dollies and can be separated for easy access to the test rotor or drive motors. In addition, the test section outer casing can be mechanically rotated through 360 degrees to allow circumferential flow surveys. This test section also includes a series of access ports through which pressure sensing probes may be radially traversed to obtain absolute upstream and downstream flow field measurements. The AFRF is elevated to a height of four inlet diameters to minimize the effects of its vortex generation caused by close proximity of the floor. A detailed

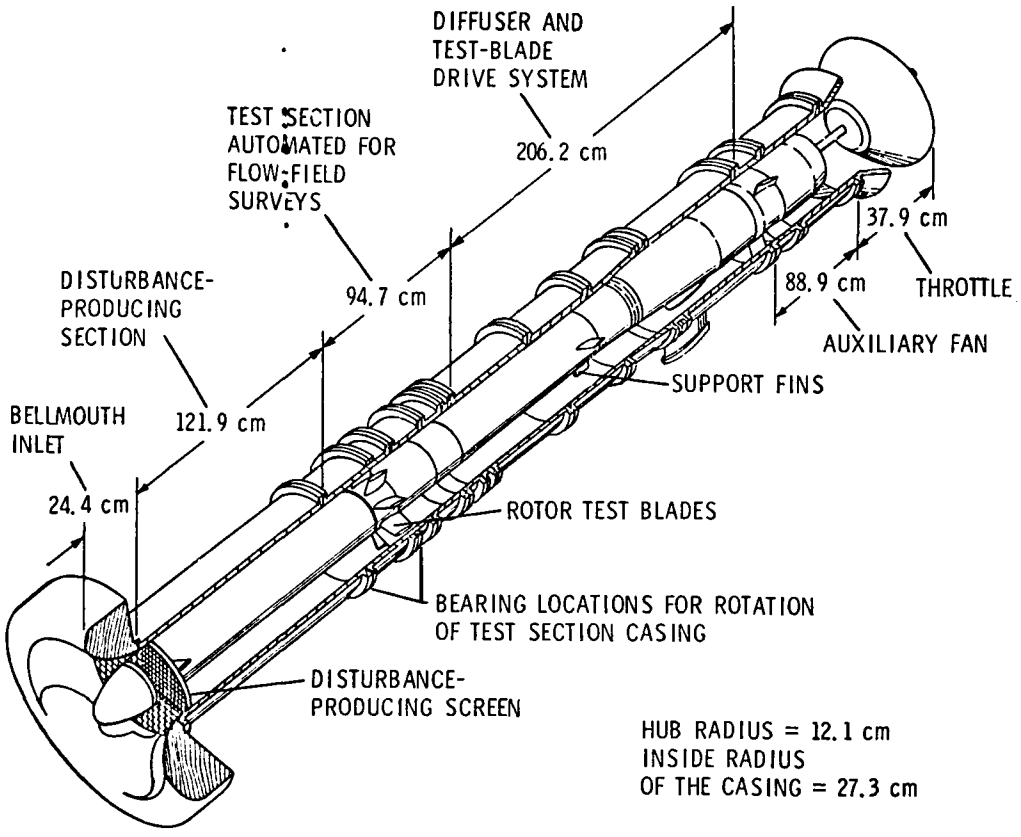

Figure 34. A Schematic of the Axial Flow Research Fan (AFRF) Facility

description of the design and use of the AFRF facility is given in Reference [12].

4.3 Test Rotor Design Procedure

The numerical analysis phase of this study was conducted using the physical characteristics of a test rotor designed by Bruce [21] specifically for the AFRF test facility. This rotor consists of nine circular-arc camberline blades that have a compressor cascade C1-thickness distribution with a maximum thickness of 10 percent of the chord. The designed free-vortex loading distribution requires considerable radial twist in the blade geometry while providing little or no axial accelerations from leading- to trailing-edge. The design loading level is expressed as

$$RV_\theta = 2.32 \text{ m}^2/\text{sec} \ (25.0 \text{ ft}^2/\text{sec}) \tag{31}$$

for a reference velocity of 24.28 m/sec (80.0 ft/sec). The design of this particular test rotor followed the method outlined by Lieblein [17] and incorporates many of the correlation data previously discussed in the SLC analysis. The choice of this test rotor for this study was largely due to the design technique which was used. In this way, comparisons between the design, predicted, and measured flow field data provide useful information concerning each phase of a new turbomachine. The design parameters, which are completely based on a uniform inlet velocity profile, are provided in Table 15. The actual measured performance characteristics of this particular rotor are shown in Appendix B.

Table 15. Design Data for Nine-Bladed Cambered Test Rotor

R	β_1	β_2	$\Delta\beta$	σ	$(i_0)_{10}-(\delta_0^0)_{10}$	1-m+n	Kt•Ksh•	ϕ	m
					Fig. 178	Fig.	$[(i_0)_{10}-(\delta_0^0)_{10}]$		
(cm)	(deg.)	(deg.)	(deg.)	(c/s)	(deg.)	179-b	(deg.)	(deg.)	Fig. 168
12.065	45.66	13.21	32.45	1.81	4.97	0.757	5.467	35.64	0.176
13.589	49.06	24.35	24.71	1.61	4.52	0.702	4.972	28.12	0.200
16.637	54.68	40.01	14.67	1.31	3.75	0.590	4.125	17.87	0.248
19.685	57.08	47.87	9.21	1.11	3.12	0.492	3.432	11.74	0.291
22.733	62.59	58.48	6.11	0.96	2.64	0.400	2.904	8.01	0.330
25.781	65.43	61.18	4.24	0.85	2.21	0.317	2.431	5.71	0.365
27.305	66.65	63.06	3.59	0.80	2.03	0.282	2.233	4.80	0.380

R	δ_0^0	δ^0	$(\delta_0^0)_{10}$	$(i_0)_{10}$	i_0	n	i	λ(or $\gamma°$)	V_θ/V_∞	α_2
	Eq.(271)	Eq.(268)	Fig. 161	Fig. 137	Eq.(262)	Fig. 138	Eq.(261)	Eq.(272)		$\tan^{-1}(V_\theta/V_\infty)$
(cm)	(deg.)	(deg.)	(deg.)	(deg.)	(deg.)		(deg.)	(deg.)		(deg.)
12.065	1.67	7.94	1.52	6.51	7.16	-0.069	4.70	23.14	0.789	38.26
13.589	1.83	7.45	1.66	6.20	6.82	-0.101	3.98	31.02	0.700	34.99
16.637	2.02	6.46	1.84	5.62	6.18	-0.161	3.30	42.44	0.572	29.76
19.685	2.08	5.48	1.89	5.00	5.50	-0.218	2.94	50.28	0.483	25.80
22.733	2.07	4.71	1.88	4.52	4.97	-0.271	2.80	55.78	0.418	22.71
25.781	2.06	4.14	1.87	4.11	4.52	-0.315	2.72	59.85	0.367	20.26
27.305	2.05	3.87	1.86	3.90	4.29	-0.340	2.66	61.59	0.348	19.21

Kt = 1.0
Ksh = 1.1
V_∞ = 37.556 m/sec
$V_{\theta inlet}$ = 0.0

V_x/V_∞ = 1.0
R_{tip} = 27.305 cm
R_{hub} = 12.065 cm
Chord = 15.240 cm

For figures and equations see Reference [16].

4.4 Instrumentation

With the exception of the blade surface static pressure measurements, all of the experimental flow field data are obtained through the use of standard prism-type, five-hole pressure probes. These probes are capable of obtaining the total and static pressures plus the three orthogonal components of total velocity. The flow angles and velocities are calculated from calibration data which are collected for each probe. The calibration procedure involves placing the given probe in a flow of known angularity in both the yaw and pitch planes, and recording the five pressure readings. From these readings, it is possible to compute individual yaw, pitch, static and total pressure coefficients for each angularity setting. A series of calibration grids are formed from these coefficients and flow angles and provide a means of determining the angularity and static and total pressures from the pressure data returned from the probe in an unknown flow. A description of the calibration procedure provided by Yocum [22] details this method as well as the Open Jet calibration facility used for the probe calibrations. A schematic of a typical five-hole prism probe along with the yaw and pitch plane orientation is given in Figure 35.

Probes of various lengths are needed for the collection of all the necessary flow field data. The probes used to measure the absolute upstream and downstream flow field, for example, are introduced into the flow channel through the outer casing. Therefore, probes of approximately 30 centimeters in length and 0.635 centimeter in diameter are used for these measurements. A schematic of this type of five-hole prism probe is shown in Figure 36. The probes that are used to measure the flow field inside the rotating blade passage are introduced into

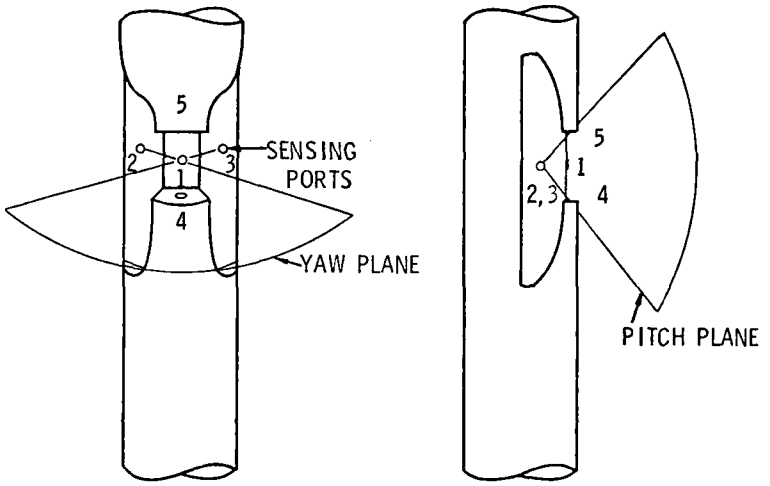

Figure 35. Orientation of Yaw and Pitch Planes of a Typical Five-Hole Prism-Type Pressure Probe

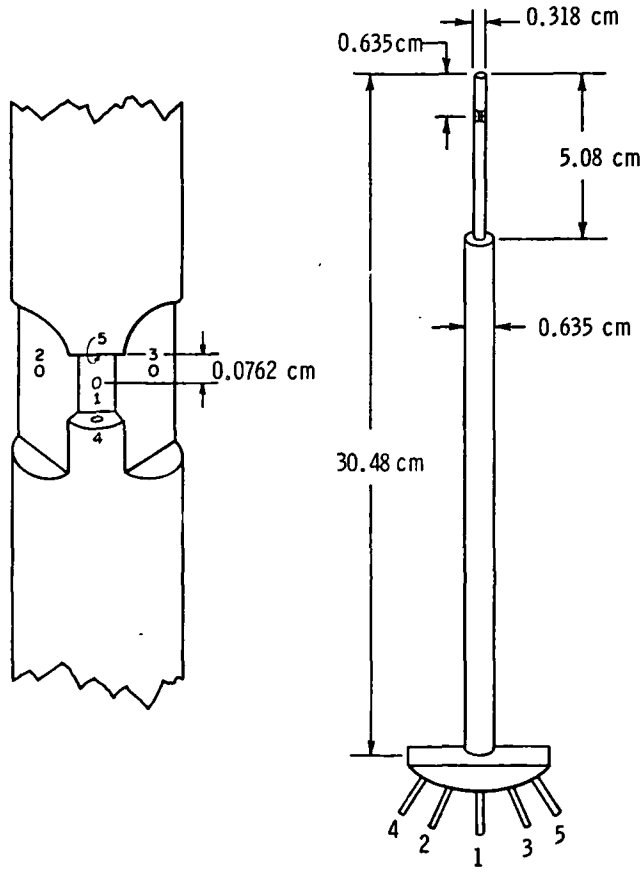

Figure 36. Five-Hole Prism Probe - United Sensor Type DA-125-12-F-10-CD

the channel from inside the modified rotor hub assembly. For each radial location that is surveyed, a separate probe is used. The lengths of these probes range from 5.8 to 17.3 centimeters and require a 0.3175 centimeter diameter to minimize any probe blockage effects. Figure 37 provides the geometry of each of the rotating five-hole pressure probes used in this investigation.

To obtain the static pressures on the blade surfaces, two additional rotor blades were fabricated and instrumented with static pressure taps. The pressure taps are arranged on the suction surface of one blade and the pressure surface of an adjacent blade at three spanwise and five chordwise locations. The chordwise tap locations are selected to yield the best least squares curve fit through the given data points as explained by Milne [23]. Each blade consists of the static pressure taps on one side of the blade and a series of spanwise slots connecting the tap holes on the opposite side. Into these slots, soft aluminum hypodermic tubing is set in place and the tap holes are redrilled to permit air flow into the tubing. Figure 38 shows the reverse side of one of these instrumented blades at this phase of the manufacturing process. The area around the hypodermic tubing is filled with a molten aluminum alloy and hand-finished to obtain the original blade contours. The excess tubing is embedded along the base of the blade and gathered at a central location. Figure 39 shows the finished instrumented rotor blades before rotor assembly.

To obtain the pressure measurements at a specific radial location, the unused tap holes leading into the hypodermic tubing are covered with small, thin pieces of clear adhesive tape. The pressure in each tube which represents the static pressure at the uncovered tap hole,

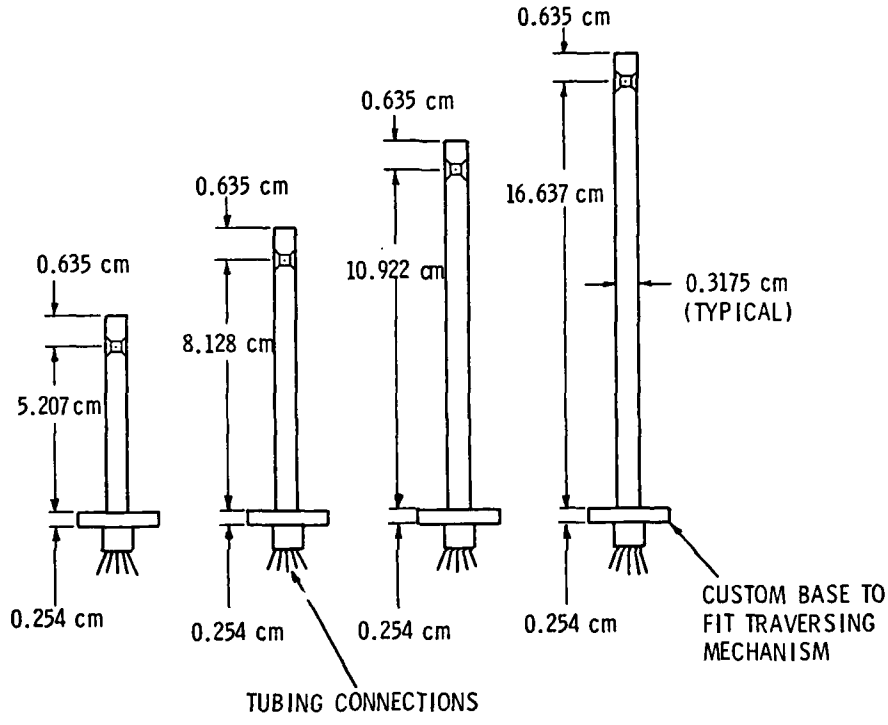

Figure 37. Dimensions of Rotating Five-Hole Prism-Type Probes

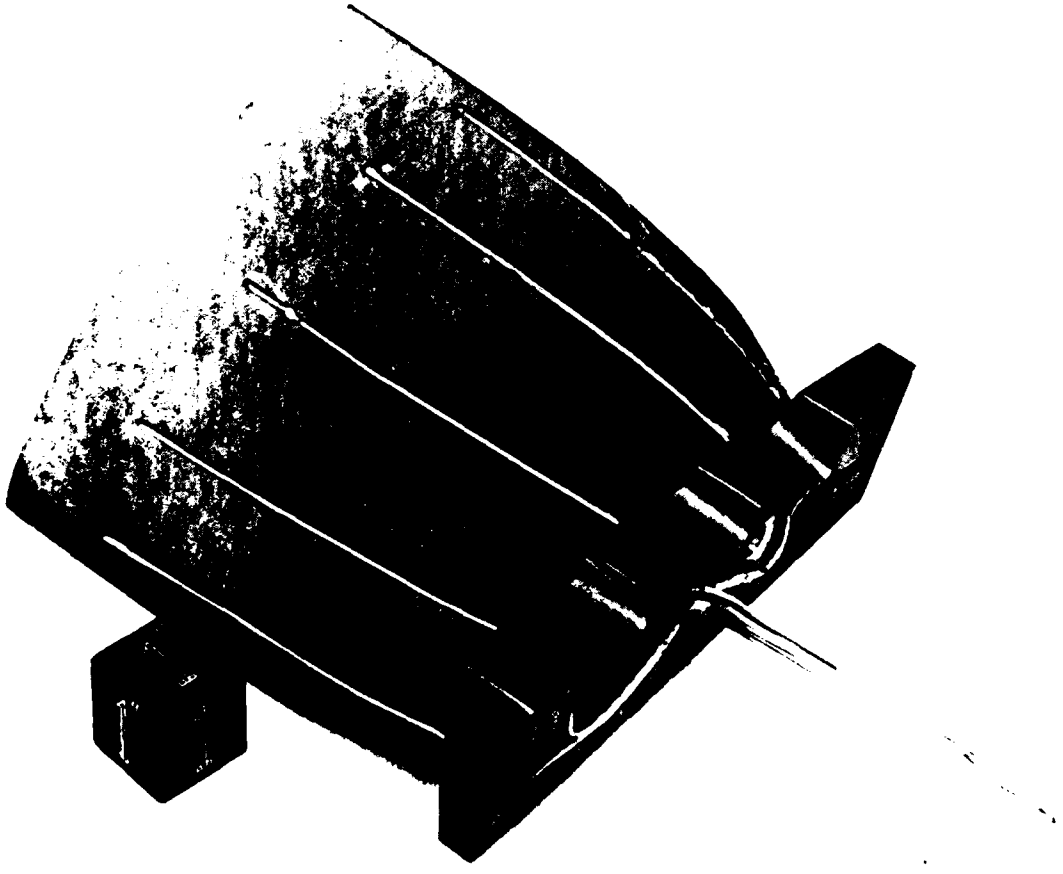

Figure 38. Instrumented Rotor Blade During Pressure Tap Installation

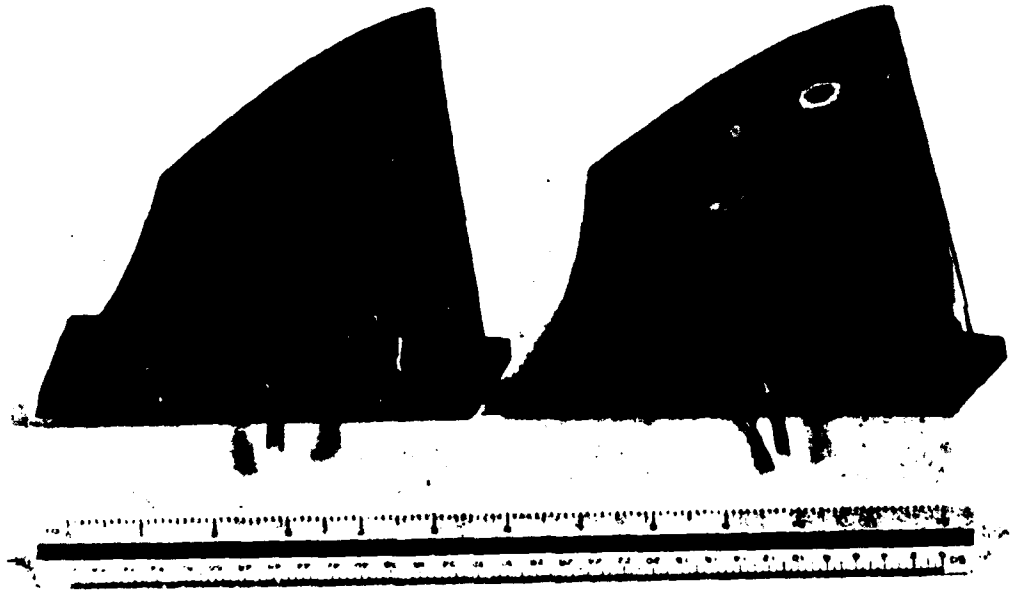

Figure 39. Rotor Blades Instrumented with Pressure Taps

is transmitted through plastic hypodermic tubing to a pressure slip-ring assembly located downstream of the test section. This slip-ring unit, used in all the rotating data collection, allows the pressure readings to be transferred from the rotational reference frame to the stationary reference frame where the signals can be converted to a usable form. A schematic of the slip-ring unit is shown in Figure 40.

A large amount of time and energy was spent developing a circumferential traversing mechanism which permits measurements of the flow field in the S_1 plane while the test rotor is operating. This mechanism consists of a modified rotor hub assembly, shown in Figure 41, and an internal mechanism that traverses a pressure probe from blade to blade. The internal mechanism is capable of positioning a probe at any of three axial locations from rotor leading to trailing edge and two positions behind the trailing-edge position. Traversing of the five-hole probe is accomplished by driving this internal assembly with a stepping motor and gear reduction unit that permits step increments of 0.083 degree. A schematic of this assembly is shown in Figure 42. The entire assembly--hub, internal probe holders, and stepping motor--rotates with the rotor while electrical signals are sent through an electrical slip-ring unit to the stepping motor, thus producing probe rotation relative to the rotating blade row. Figure 43 shows the individual components of this traversing mechanism, while Figure 44 shows one of the five-hole probes mounted in the traverser which has been installed in the AFRF test facility.

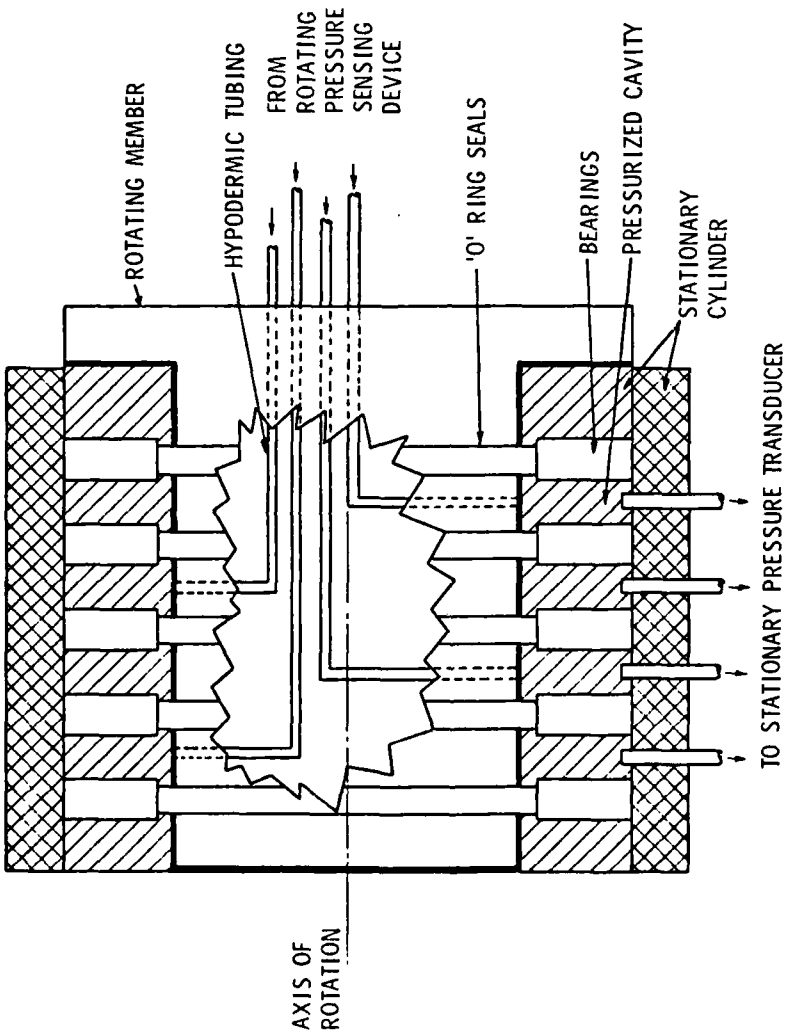

Figure 40. Pressure Slip-Ring Assembly

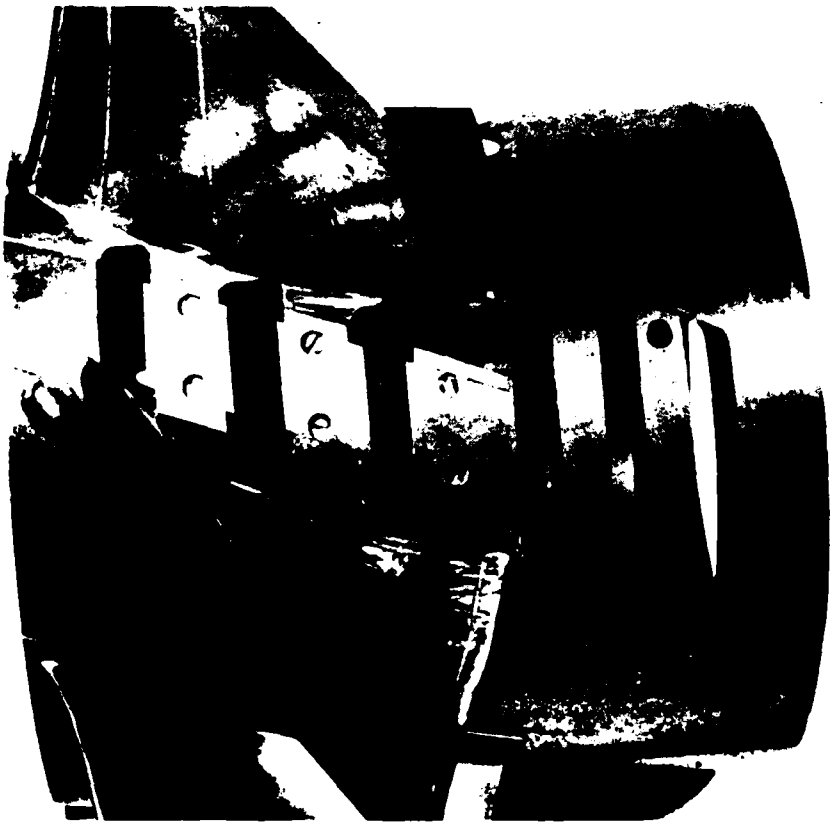

Figure 41. Modified Rotor Hub Assembly

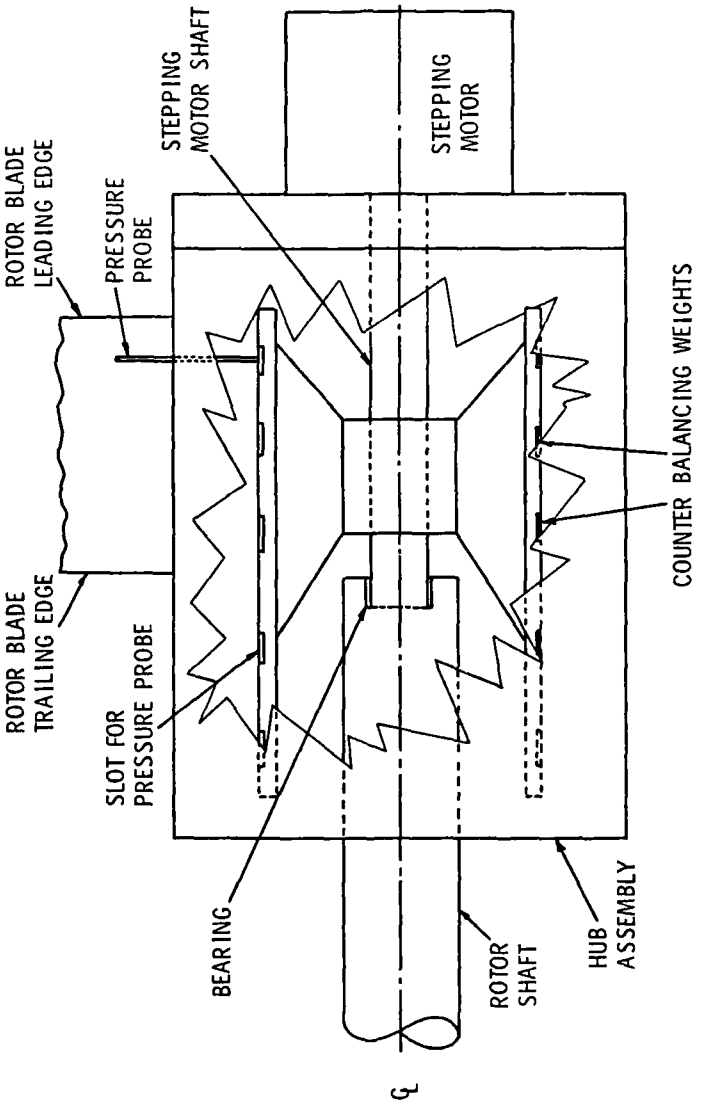

Figure 42. Schematic of AFRF Circumferential Traversing Mechanism

Figure 43. AFRF Traversing Mechanism Components

Figure 44. Five-Hole Probe Mounted in AFRF Traversing Mechanism

4.5 Data Acquisition

Once the pressure signals reach the stationary reference frame, the data must be properly processed into a usable form. The experimental data, whether collected in a rotational or stationary reference frame, are processed in an identical manner. The pressurized tubes from the sensing probes are connected to an automatically indexing scanivalve which permits the reading of each pressure port in sequence. This pressure is transmitted through the scanivalve to a ±1.0 psi Validyne Model DP15 differential pressure transducer and converted to an electrical signal. This electrical signal is transmitted to an integrating digital voltmeter and the voltage is recorded on paper tape. The reference side of the differential pressure transducer is open to atmospheric pressure which allows the zero shift of the power supply unit to be monitored and recorded for each survey point. This zero shift is subtracted from all the voltage values before any further data reduction is attempted. Figure 45 shows a schematic of the data acquisition system.

The final reduction of the test data requires the use of three computing systems. An IBM System-7 is used to read the paper tape containing the raw voltages and produces a punched deck of standard cards. These cards are read into an IBM System-34 computer for a preliminary data analysis. At this point, the data is checked for the repeatability of a particular test run. Each test run consists of four replicated sets of test conditions from which an average is calculated and a statistical analysis based on Student's t-distribution for small sample size is conducted. If the repeatability of the data is satisfactory, a second set of cards is produced. This final set of

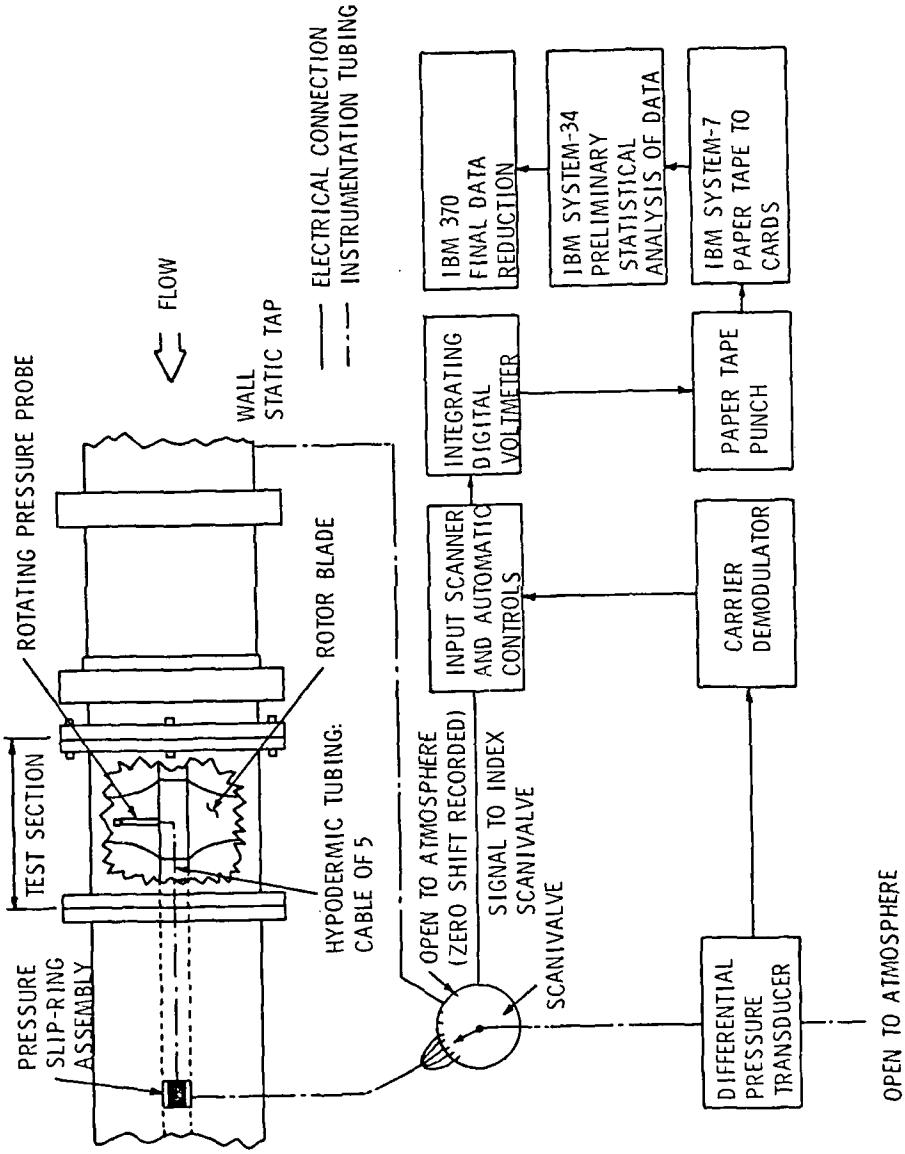

Figure 45. Schematic of Data Acquisition and Reduction System

cards is read into the final data reduction and statistical analysis program which is housed on the IBM 370 computer located at The Pennsylvania State University. This reduction program uses the individual calibration curves for the specific pressure probe and obtains the necessary velocity and pressure data.

5. EXPERIMENTAL PROCEDURES AND RESULTS

5.1 Stationary Measurements

A preliminary part of the experimental investigation included spanwise flow field surveys at the inlet and exit stations of the rotor. Fifteen radial positions were surveyed using two five-hole prism-type pressure probes. These probes were traversed radially through the access ports in the outer wall casing of the AFRF. The tunnel operating conditions throughout the experimental investigation were maintained to produce the design mass flowrate condition for the test rotor. This condition was obtained for a flow coefficient defined as

$$\phi = \frac{V_\infty}{U_{TIP}} \tag{32}$$

of 0.432. This design flow coefficient was achieved at a tunnel through-flow velocity of 19.8 m/sec (65.0 ft/sec) and a blade row rotational speed of 1604 RPM.

The radial coordinates of the 15 survey points are given in Table 16. The axial locations of the upstream and downstream probes normalized by the blade chord length are 0.717 and 1.62, respectively. This measurement and all subsequent axial locations are referenced to the leading-edge of the blade row at the blade-hub intersection point. The results of this survey are shown in Figure 46 as normalized velocity ratios as a function of the normalized radial position. Also shown in this figure are the design values of tangential and axial velocity. The experimental study shows an inlet axial velocity boundary layer on both the inner hub and outer casing surfaces of the AFRF. Even though

Table 16. Radial Distance from Rotor Hub for Each Radial Probe Position of Stationary Flow Field Measurements

Probe Position No.	Radial Distance from Rotor Hub
1	0.762 cm (0.30 in)
2	1.270 cm (0.50 in)
3	1.778 cm (0.70 in)
4	2.286 cm (0.90 in)
5	3.048 cm (1.20 in)
6	5.080 cm (2.00 in)
7	6.350 cm (2.50 in)
8	7.620 cm (3.00 in)
9	8.890 cm (3.50 in)
10	11.430 cm (4.50 in)
11	12.700 cm (5.00 in)
12	13.208 cm (5.20 in)
13	13.716 cm (5.40 in)
14	14.224 cm (5.60 in)
15	14.665 cm (5.75 in)

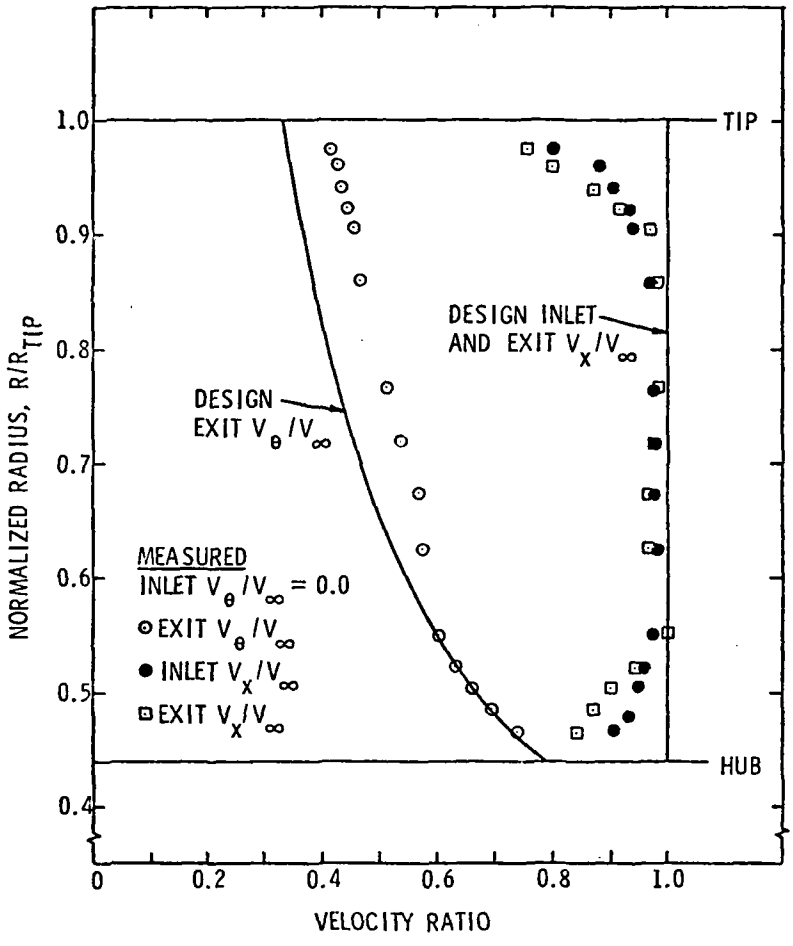

Figure 46. Measured and Rotor Design Inlet and Exit Velocity Profiles

the rotor design method fails to acknowledge this inlet boundary layer, the measured exit tangential velocity profile is not very far from the design profile. One of the effects of an inlet boundary layer is to increase the blade incidence angles in those regions where the actual axial velocity vector is smaller than the design value. Since the root sections of this free-vortex designed rotor are loaded quite heavily already, the increase in incidence angle probably does not add to the work that these sections do. In fact, there may even be a loss of work due to flow separation at high incidences. The tip sections, on the other hand, are loaded relatively lightly and may produce more turning at the higher incidence angles than anticipated from the design calculations. These two trends are observed in the comparison of the design and measured exit tangential velocity profiles in Figure 46.

5.2 Blade Surface Pressure Measurements

The next step of the experimental program was the measurement of the static pressures on the suction and pressure surfaces of the rotating blades. For this part of the study, the two instrumented blades were connected through the pressure slip-ring unit to the stationary data acquisition system. Again, the design mass flowrate condition was set and the measurements taken. Since only one radial location of taps can be surveyed at any one time, some error may be introduced if the run conditions differ between the shutdown and start-up phases. This error can be minimized by normalizing the results of each data point by some measured upstream reference condition. These reference conditions were monitored by upstream static pressure taps located on the AFRF outer casing and were recorded for each survey point. This normalizing procedure was used throughout the experimental investigation

and was also used in the numerical investigation to permit comparisons of the data from these two phases.

Since the blade surface static pressure measurements were conducted in a rotating reference frame, the effects of rotation must be accounted for in the reduction of the data. The effect of rotating a column of fluid is to exert a force outward from the axis of rotation whose magnitude is a function only of radial distance from the axis. The calculation of the true static pressure from any of the blade surface static pressure taps is given by

$$P_{TRUE} = P_{MEAS} - P_{ROTATION} \quad , \tag{33}$$

where the effects of rotation are expressed as a pressure ($P_{ROTATION}$). A summary of the derivation of the rotational correction to the static pressure measurement and the specific values of $P_{ROTATION}$ for each radial location is given in Appendix C. Figures 47 through 49 show the final corrected data in the form of a pressure coefficient as a function of the distance along the section chord.

5.3 Blade Passage Measurements

5.3.1 Axial Survey Locations. Flow field data collected in the regions between and behind two adjacent rotor blades required the majority of the testing time and produced the majority of data. This phase of the investigation involved the use of four five-hole prism-type pressure probes of different lengths. Each probe was circumferentially traversed across each of five axial locations provided by the AFRF rotor hub assembly. These locations consisted of three intra-blade stations and two wake survey stations downstream of the trailing-edge. Figure 50 provides a schematic and physical dimensions of the

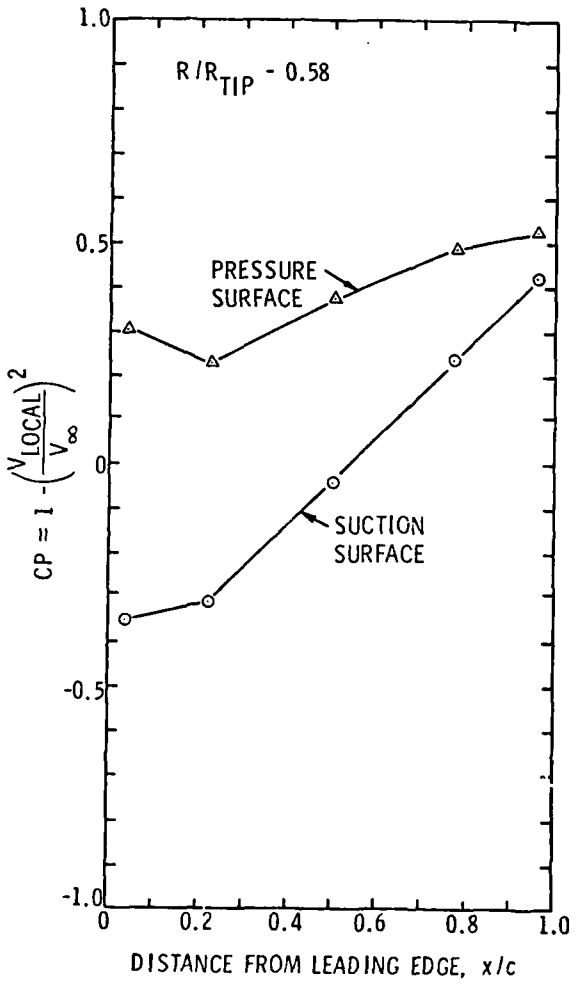

Figure 47. Measured Blade Surface Pressure Distribution at R/R_{TIP} = 0.580

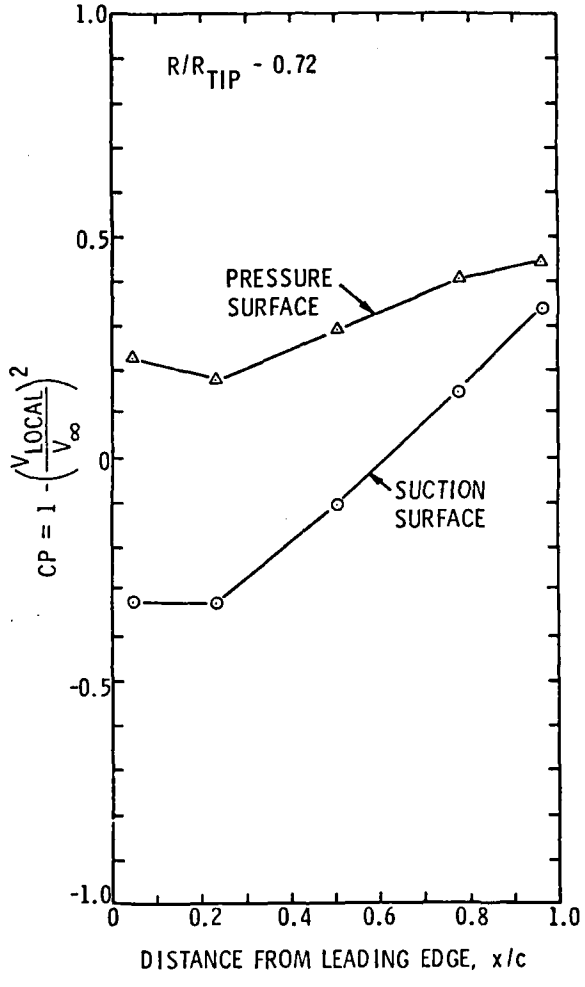

Figure 48. Measured Blade Surface Pressure Distribution at R/R_{TIP} = 0.720

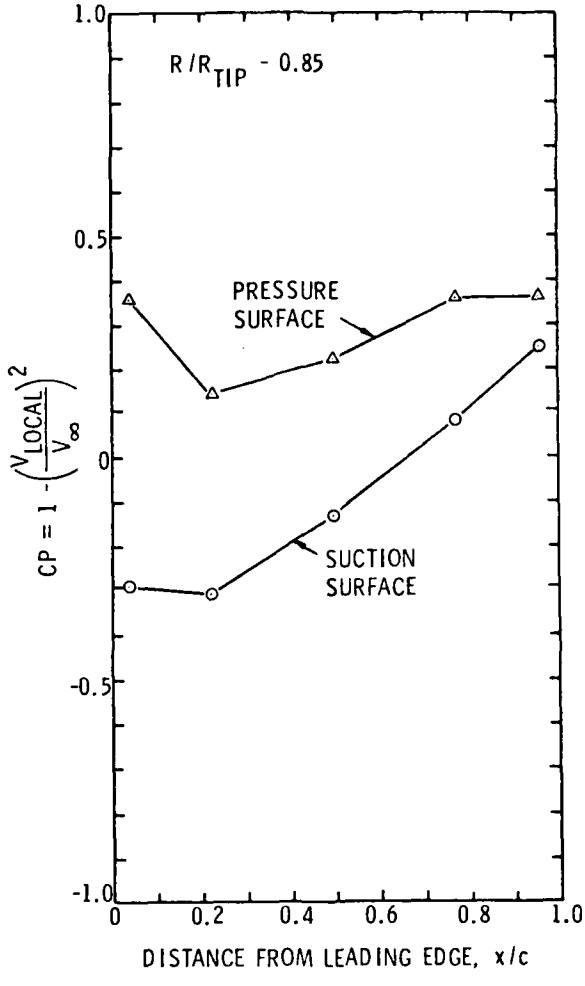

Figure 49. Measured Blade Surface Pressure Distribution at $R/R_{TIP} = 0.850$

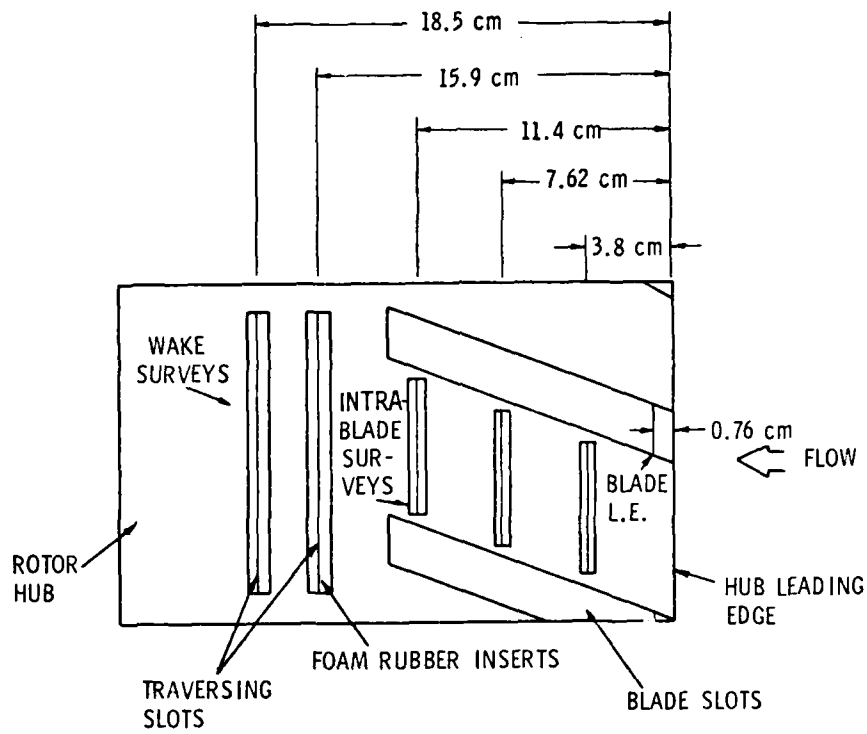

Figure 50. Schematic of Rotor Hub Assembly Indicating Location of Traversing Slots

station locations, while Figure 51 shows the actual internal traversing mechanism which holds the probes in place. The overall diameter of this internal device is 16.05 cm and includes a series of counterbalancing weights which fill the remaining unused probe locations.

Each test run consisted of traversing one of the pressure probes from the suction surface of one blade to the pressure surface of the next blade a total of four times. These four surveys were then analyzed to determine the repeatability of each probe position data point, and finally, an average value was computed from these runs at each data point position. The number of final data points for a particular survey was a function of the blade spacing and probe radius. The radius of the probe was included as one of the factors influencing the number of data points because the local twist of the blade is a function of radius. Due to this large amount of blade twist, some of the longer probes cannot survey the flow field close to the blade surface without touching the lower more highly twisted sections. For this reason, the starting and stopping distance relative to the blade surfaces was recorded for each survey.

5.3.2 Rotational Effects. The five-hole prism-type pressure probes yield five values of pressure for each data point: the indicated total pressure (hole 1), the pressures in the yaw plane (holes 2 and 3), and the pressures in the pitch plane (holes 4 and 5). The relative difference in pressure sensed by the two yaw plane readings and the two pitch plane static readings is related to the flow yaw and pitch angles, respectively. The five pressure readings (P_1, P_2, P_3, P_4, and P_5) are used to form two normalized coefficients known as the yaw coefficient

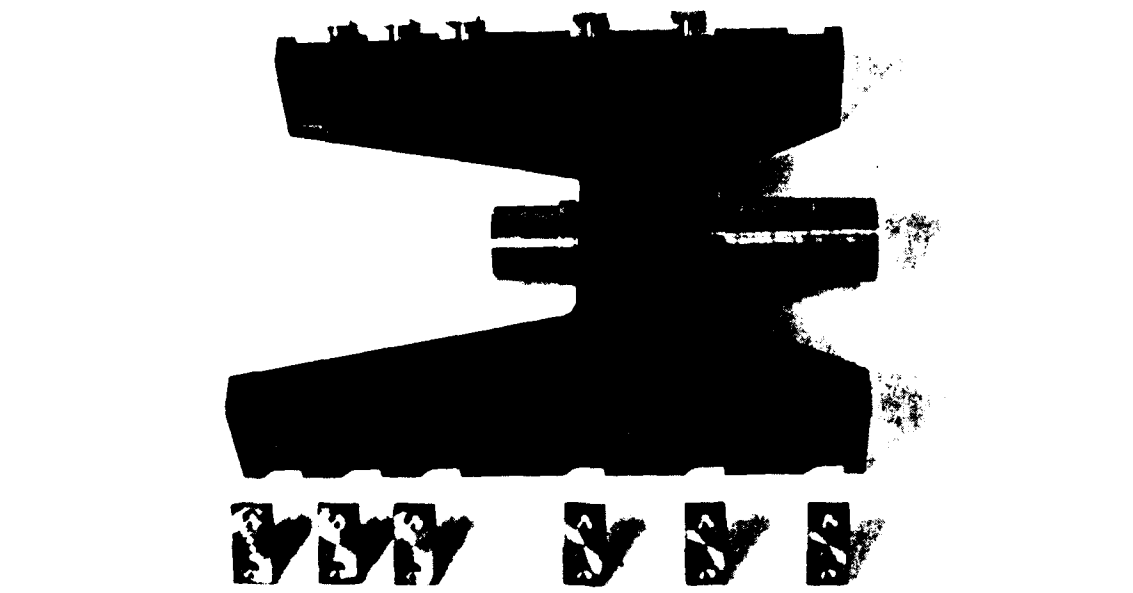

Figure 51. The Internal Traversing Probe Holder

$$CP_Y = \frac{P_3 - P_2}{P_1 - 0.25\ (P_2 + P_3 + P_4 + P_5)} \quad , \tag{34}$$

and the pitch coefficient

$$CP_P = \frac{P_4 - P_5}{P_1 - 0.25\ (P_2 + P_3 + P_4 + P_5)} \quad . \tag{35}$$

These coefficients are used in conjunction with the calibration data obtained for each probe to compute total and static pressure, as well as yaw and pitch flow angles. The actual calibration curves used in the computational procedure for the four rotating pressure probes are shown in Figures 52 through 63. Each probe needs three calibration grids which are numerically cross-plotted by the data reduction procedure so that, given the yaw and pitch coefficients, which are computed from the five pressure readings, the actual pressure, and velocity fields can be determined. The effects of the rotation of the column of air inside the pressure probe are accounted for through the formulation of the coefficients given in Equations (33) and (34). Since all of the five readings from the five-hole probe will be affected by the same rotational pressure force, the net effect is to multiply and divide Equations (33) and (34) by some constant value. The finite spacing that exists between the five pressure sensing holes is so small that any rotational effect due to this distance is considered negligible. Thus, the data reduced from the rotating five-hole pressure probes requires no additional correction for rotational effects.

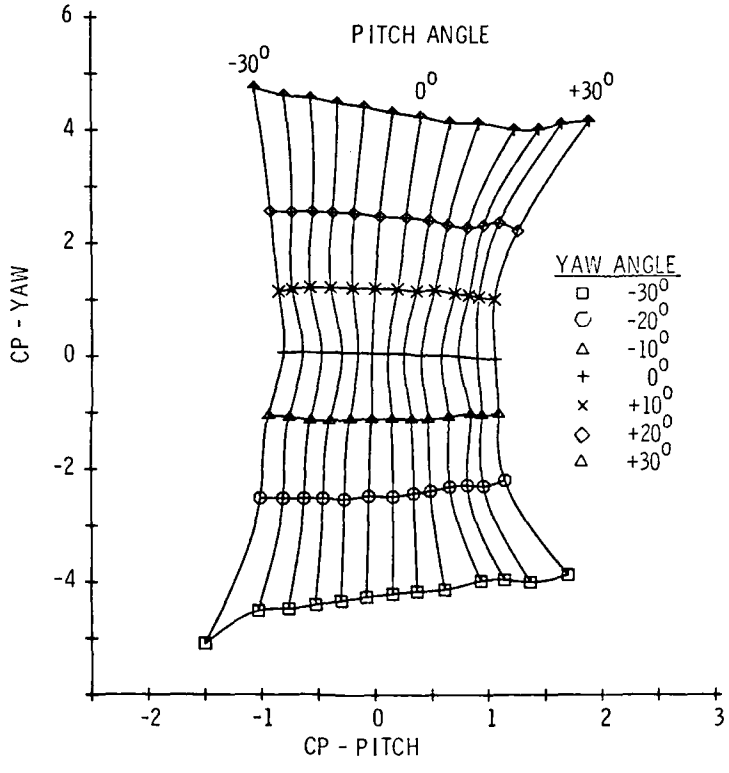

Figure 52. CP_Y vs. CP_P Calibration Grid for Rotating Probe (R/R_{TIP} = 0.484, Re = 5182)

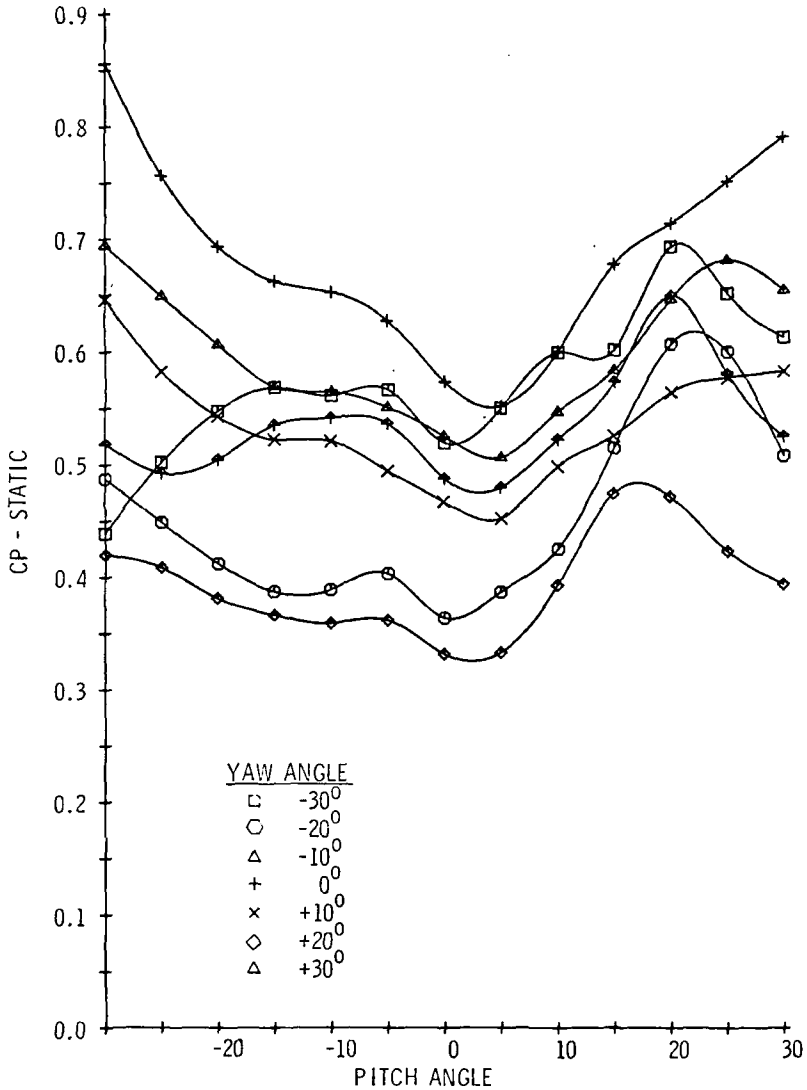

Figure 53. Static Pressure Coefficient vs. Pitch Angle Calibration Grid for Rotating Probe (R/R_{TIP} = 0.484, Re = 5182)

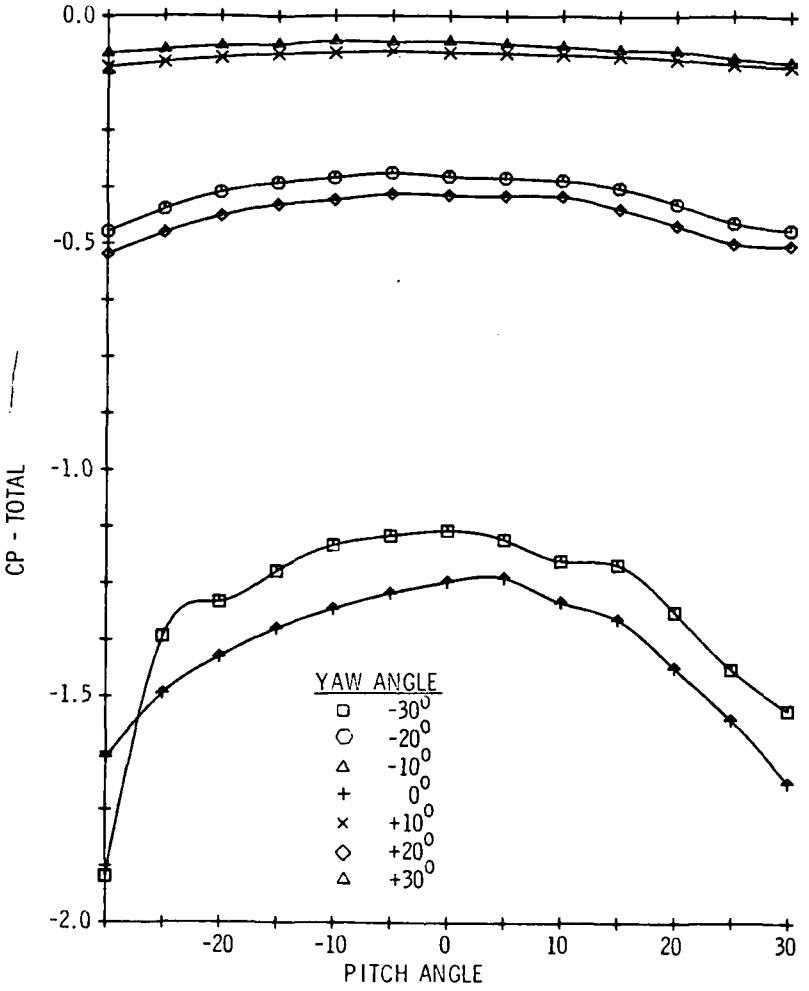

Figure 54. Total Pressure Coefficient vs. Pitch Angle Calibration Grid for Rotating Probe (R/R_{TIP} = 0.484, Re = 5182)

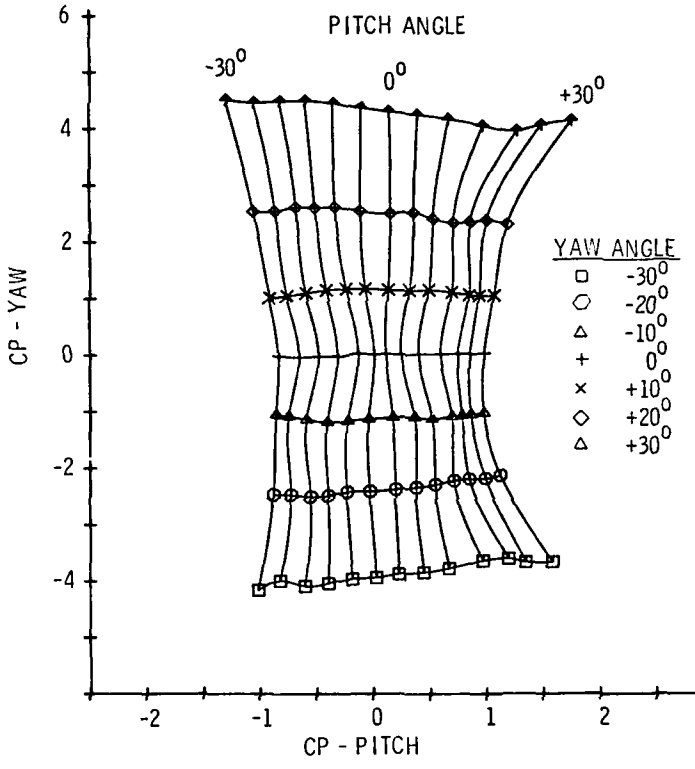

Figure 55. CP_Y vs. CP_P Calibration Grid for Rotating Probe (R/R_{TIP} = 0.591, Re = 6312)

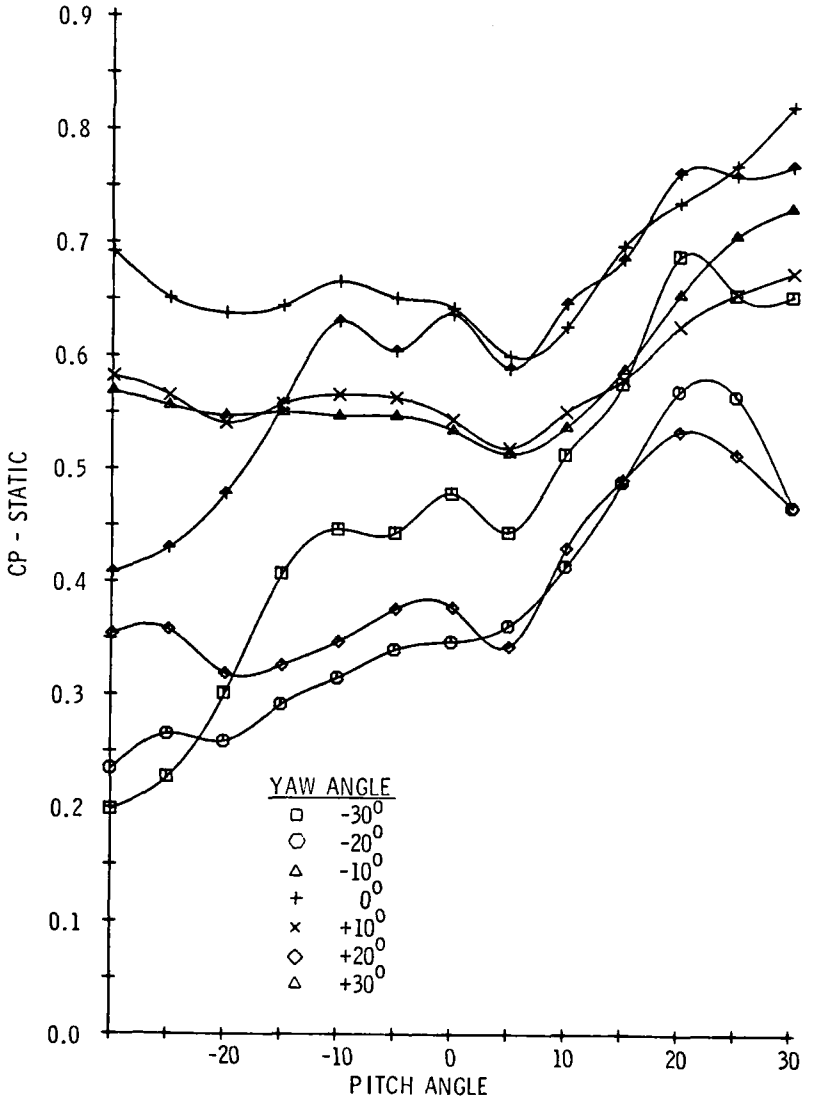

Figure 56. Static Pressure Coefficient vs. Pitch Angle Calibration Grid for Rotating Probe (R/R_{TIP} = 0.591, Re = 6312)

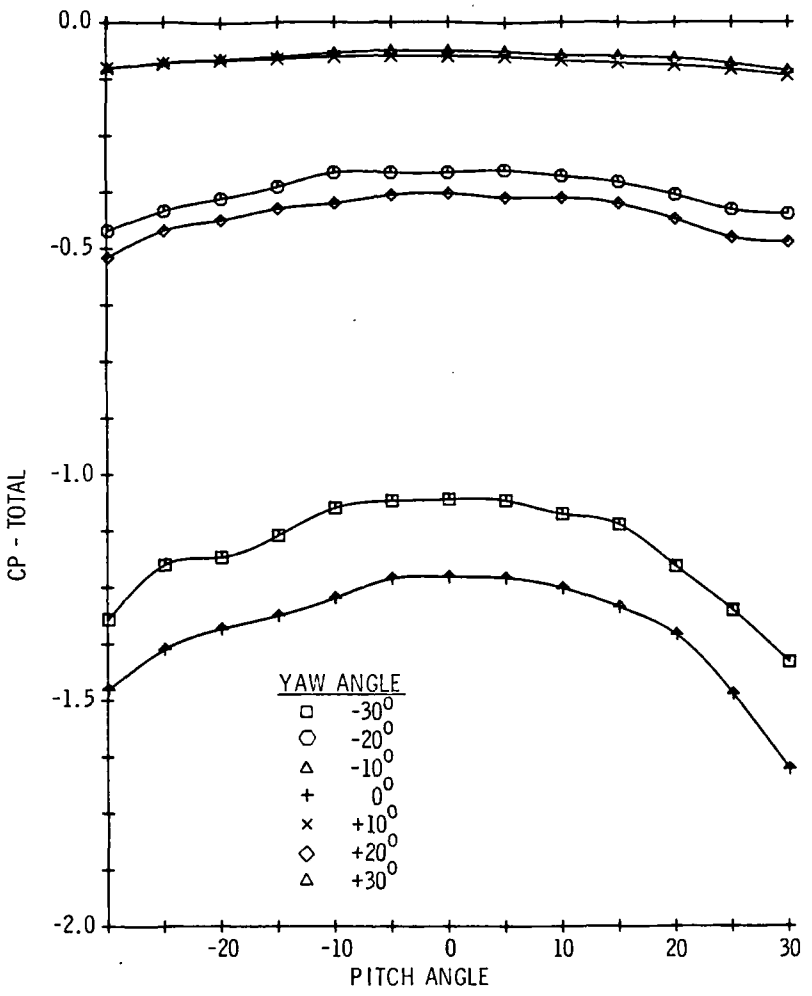

Figure 57. Total Pressure Coefficient vs. Pitch Angle Calibration for Rotating Probe (R/R_{TIP} = 0.591, Re = 6312)

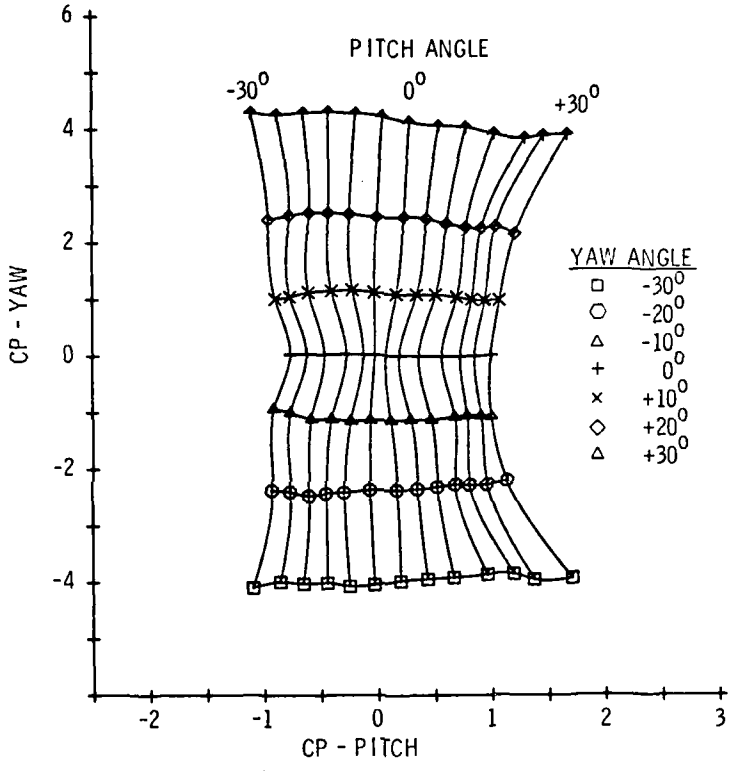

Figure 58. CP_Y vs. CP_P Calibration Grid for Rotating Probe (R/R_{TIP} = 0.694, Re = 6976)

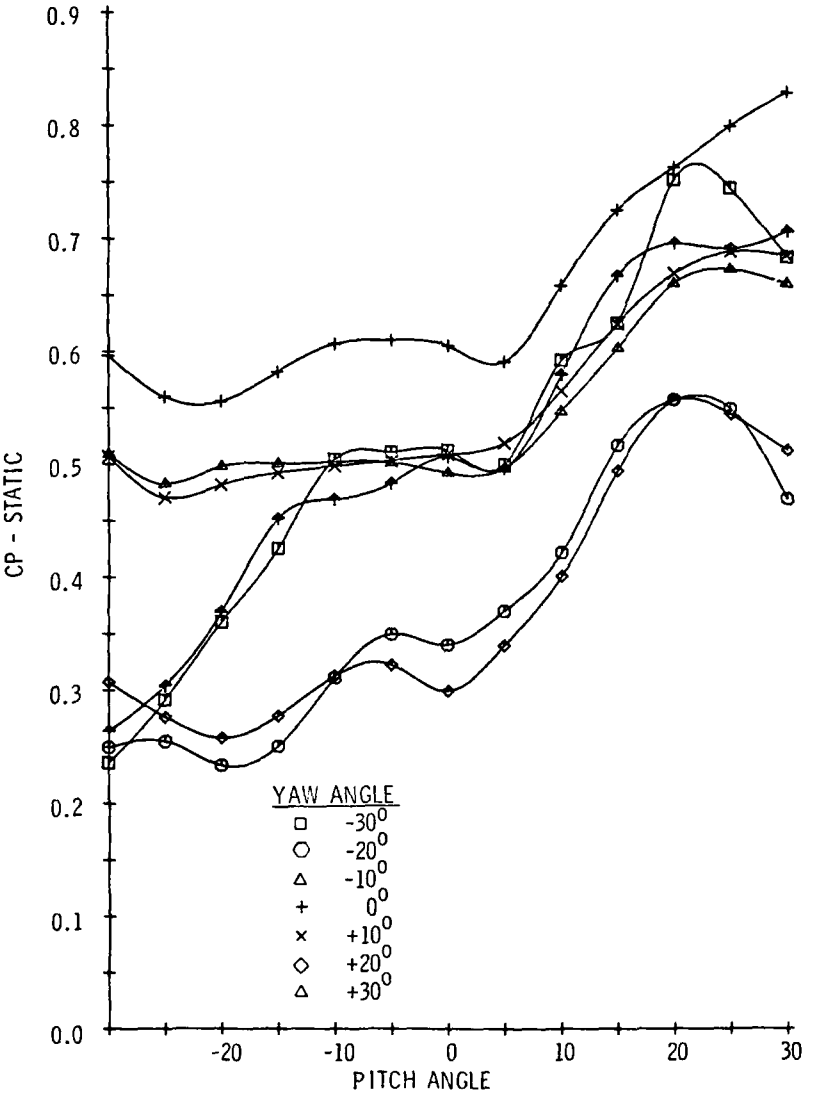

Figure 59. Static Pressure Coefficient vs. Pitch Angle Calibration Grid for Rotating Probe (R/R_{TIP} = 0.694, Re = 6976)

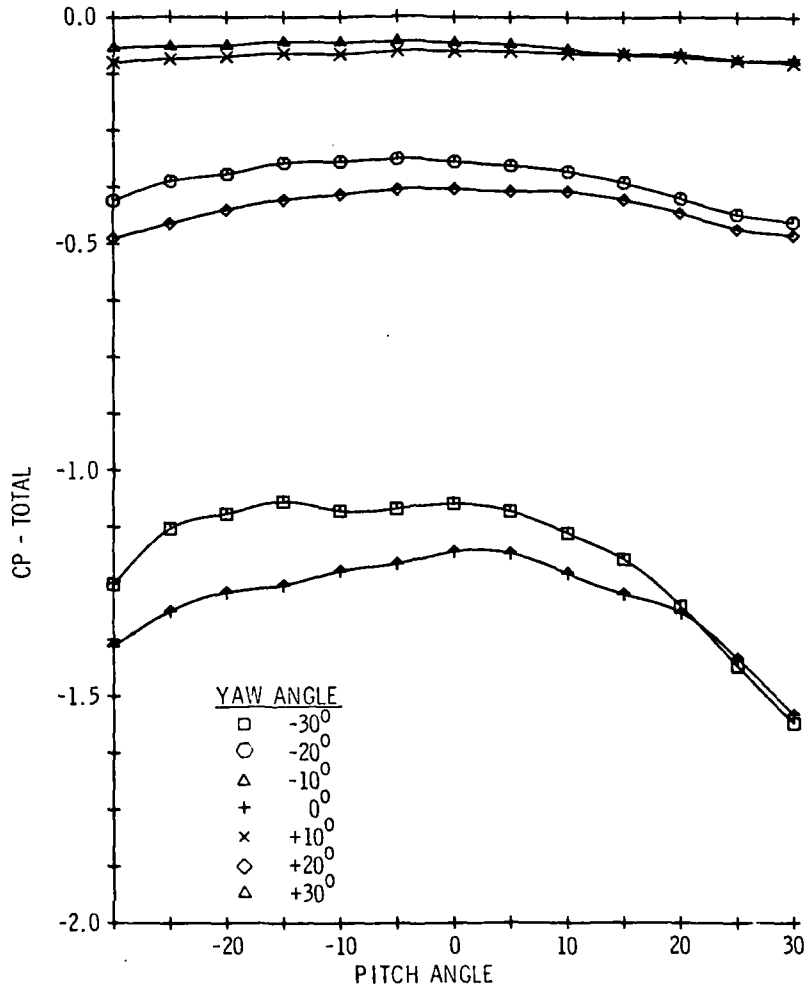

Figure 60. Total Pressure Coefficient vs. Pitch Angle Calibration Grid for Rotating Probe (R/R_{TIP} = 0.694, Re = 6976)

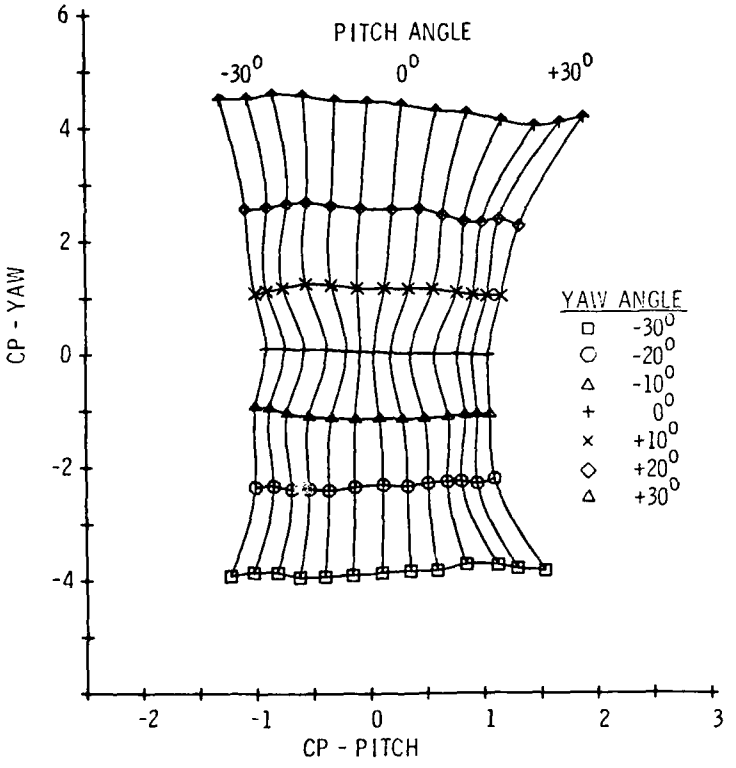

Figure 61. CP_Y vs. CP_P Calibration Grid for Rotating Probe (R/R_{TIP} = 0.903, Re = 7355)

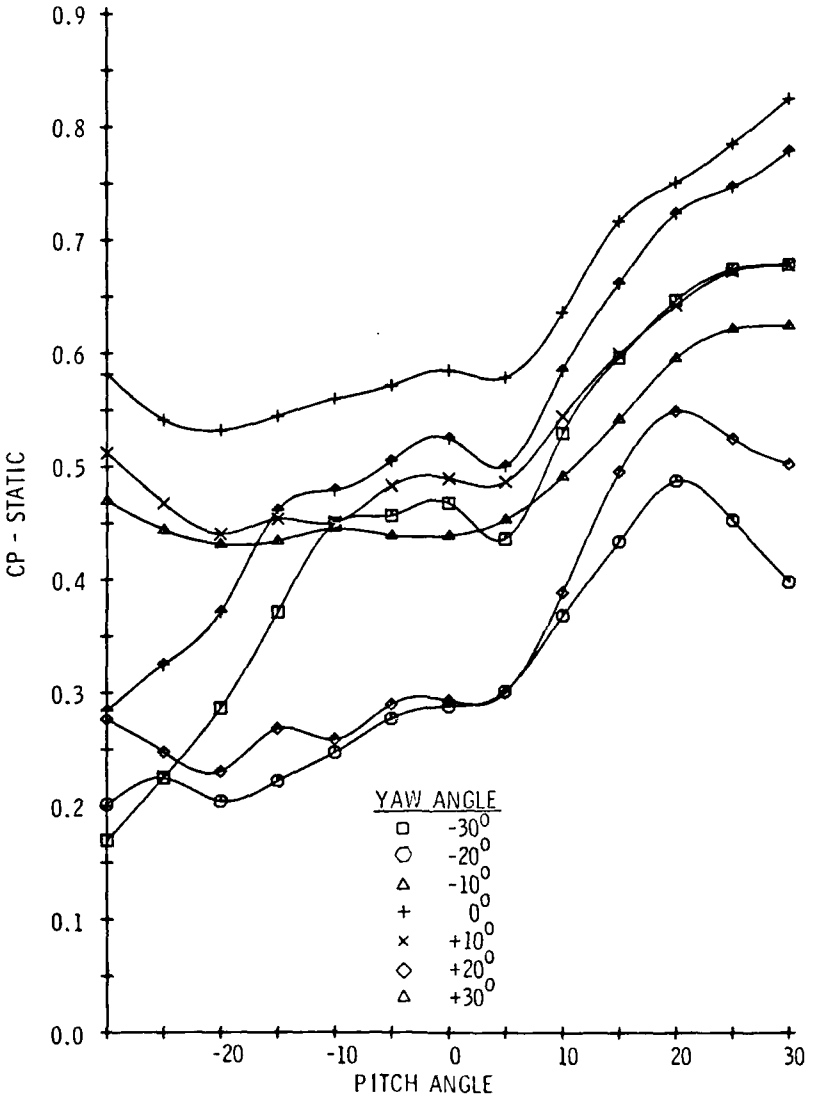

Figure 62. Static Pressure Coefficient vs. Pitch Angle Calibration Grid for Rotating Probe (R/R_{TIP} = 0.903, Re = 7355)

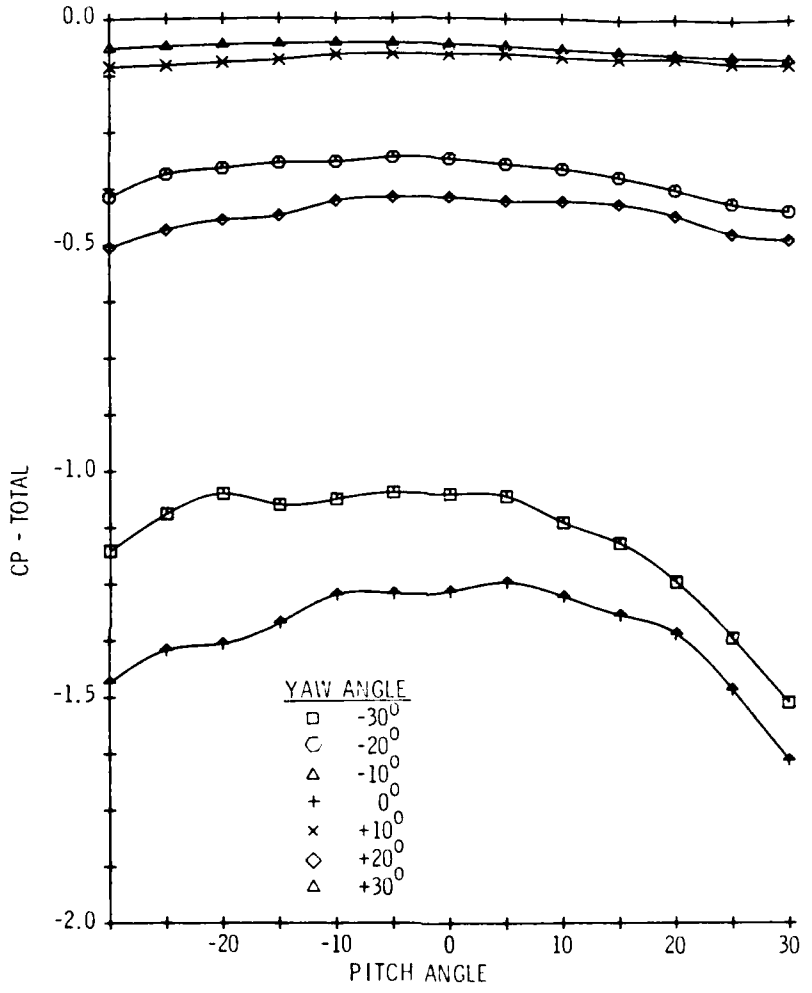

Figure 63. Total Pressure Coefficient vs. Pitch Angle Calibration Grid for Rotating Probe (R/R_{TIP} = 0.903, Re = 7355)

5.3.3 Wall Effects. The pressure probes used for the blade channel rotating measurements were calibrated at a Reynolds number based on probe diameter close to the value that each probe was expected to experience. The selection of the particular calibration Reynolds number was based on the rotor design information. The other concern during the calibration of the rotating probes was the effect of close proximity of the solid blade surfaces on the data accuracy. To investigate the effects of traversing a probe longitudinally towards a solid surface, the Open Jet calibration facility was fitted with a flat plate mounted parallel to the longitudinal axis of a probe. A schematic of the test setup is shown in Figure 64. The probe was positioned 6.35 cm from the plate and successively moved to within 0.159 cm of the plate. The readings obtained from the five pressure sensing holes were reduced to yield the total and static pressure coefficients, as well as the yaw and pitch coefficients. The four parameters were then plotted as a function of the distance from the flat plate in terms of probe diameters in Figures 65 through 68. Three separate test configurations were included in these results so that the effect of yaw angle could be investigated. The plot of the total pressure coefficient, Figure 65, shows a relatively flat response to the wall proximity phenomenon to within approximately two probe diameters. Figure 66, on the other hand, indicates an increased sensitivity in the static pressure coefficient to this phenomenon. Even so, the major perturbations to the static pressure coefficient occurred within two or three probe diameters. These two plots also show that, while the magnitude of the coefficients change with yaw angle, the basic trends remain unaffected.

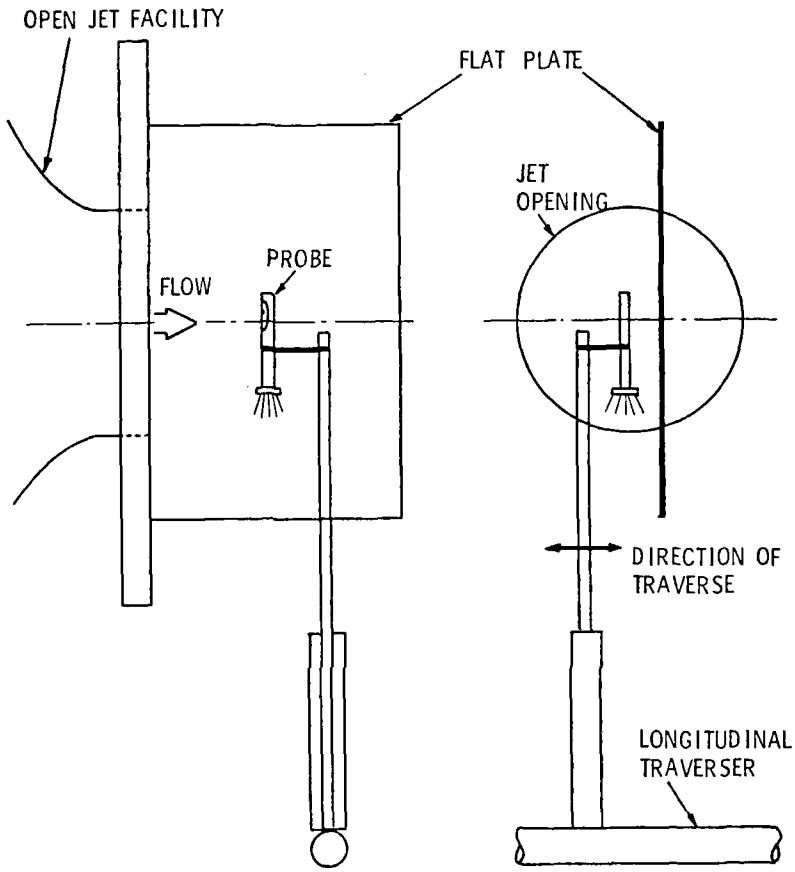

Figure 64. Schematic of Wall Proximity Test Setup

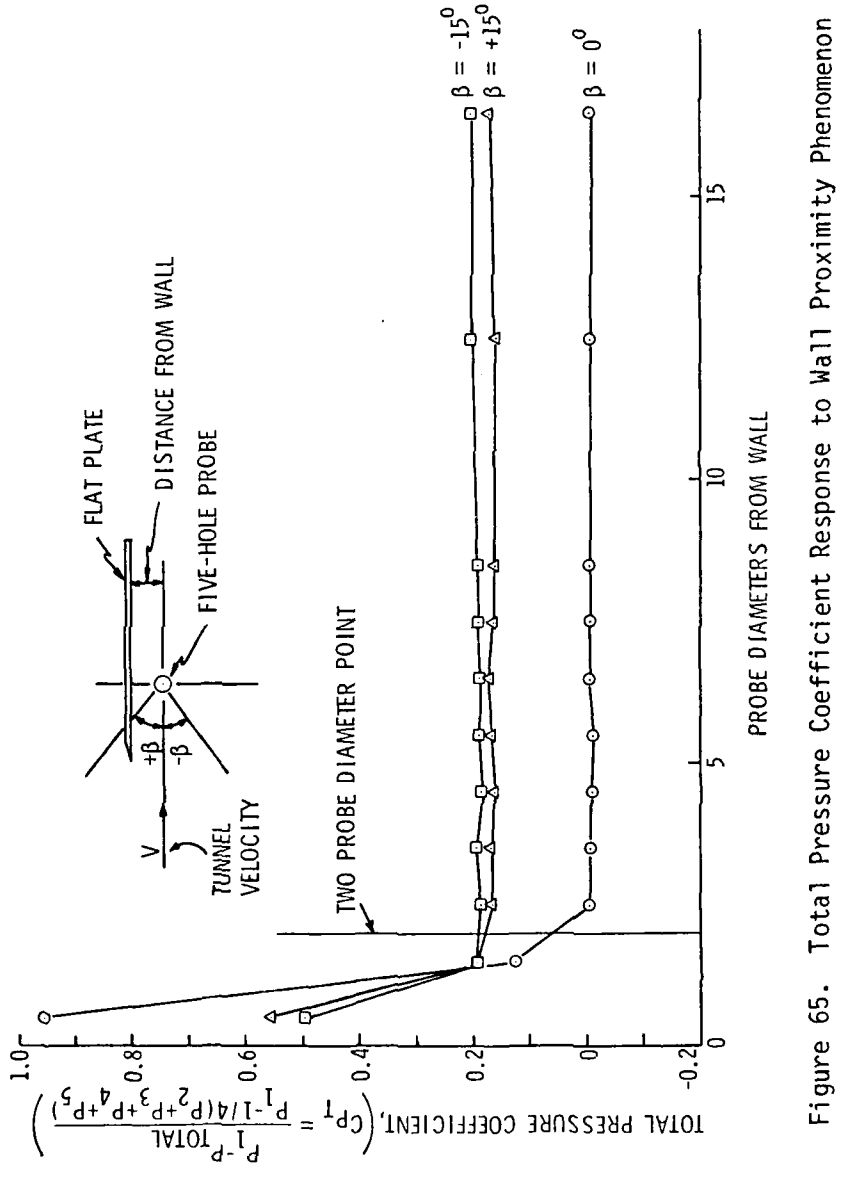

Figure 65. Total Pressure Coefficient Response to Wall Proximity Phenomenon

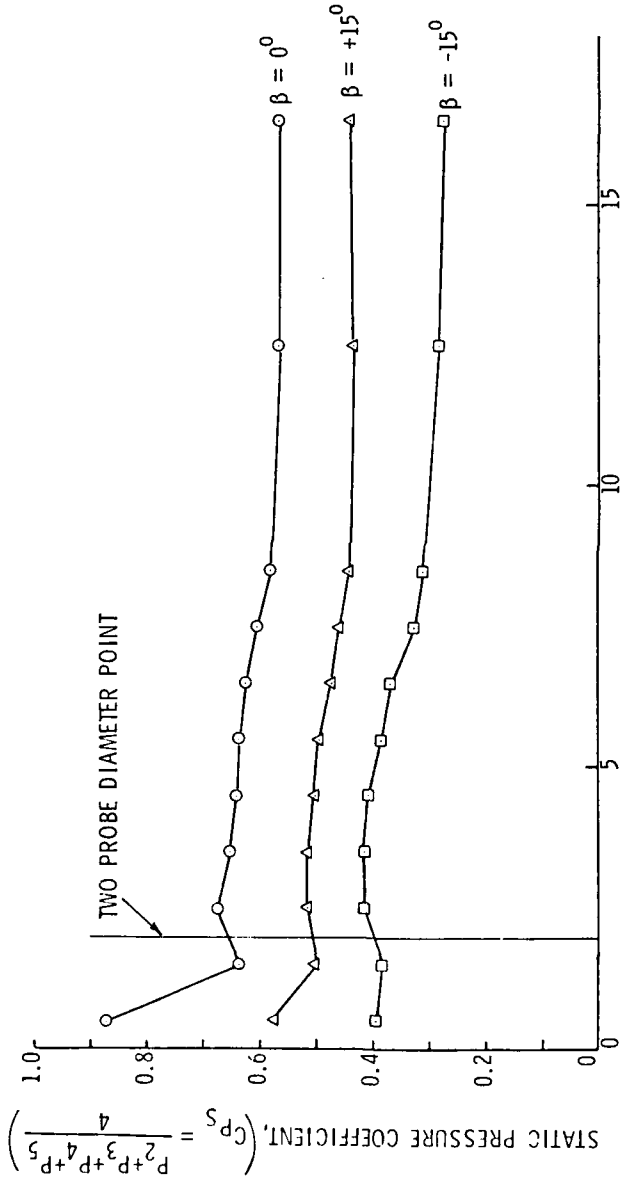

Figure 66. Static Pressure Coefficient Response to Wall Proximity Phenomenon

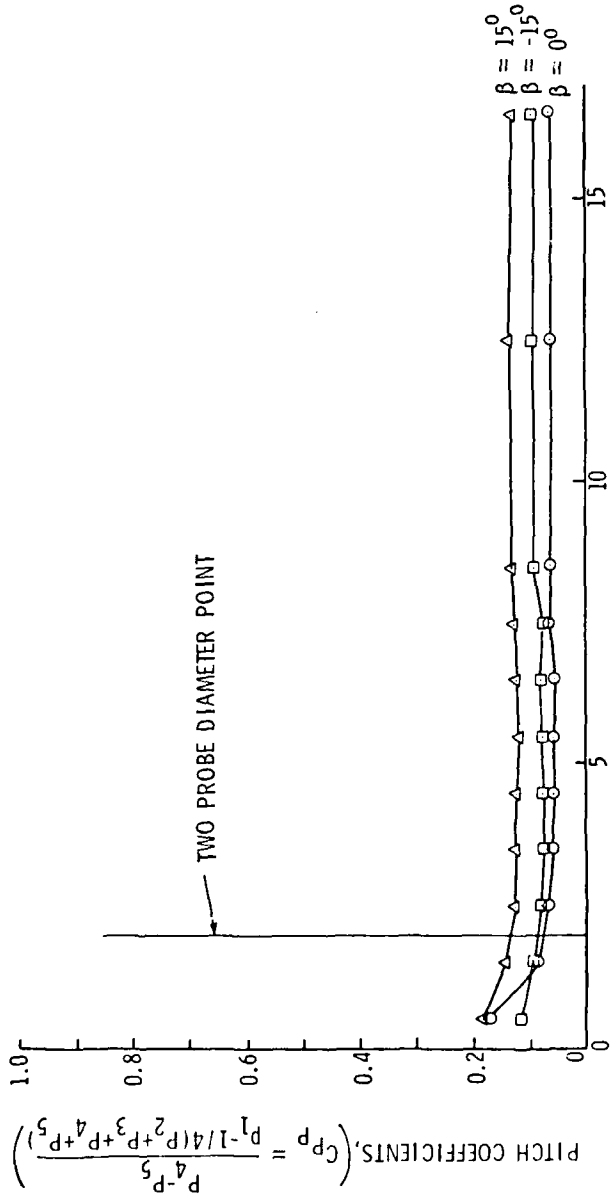

Figure 67. Pitch Coefficient Response to Wall Proximity Phenomenon

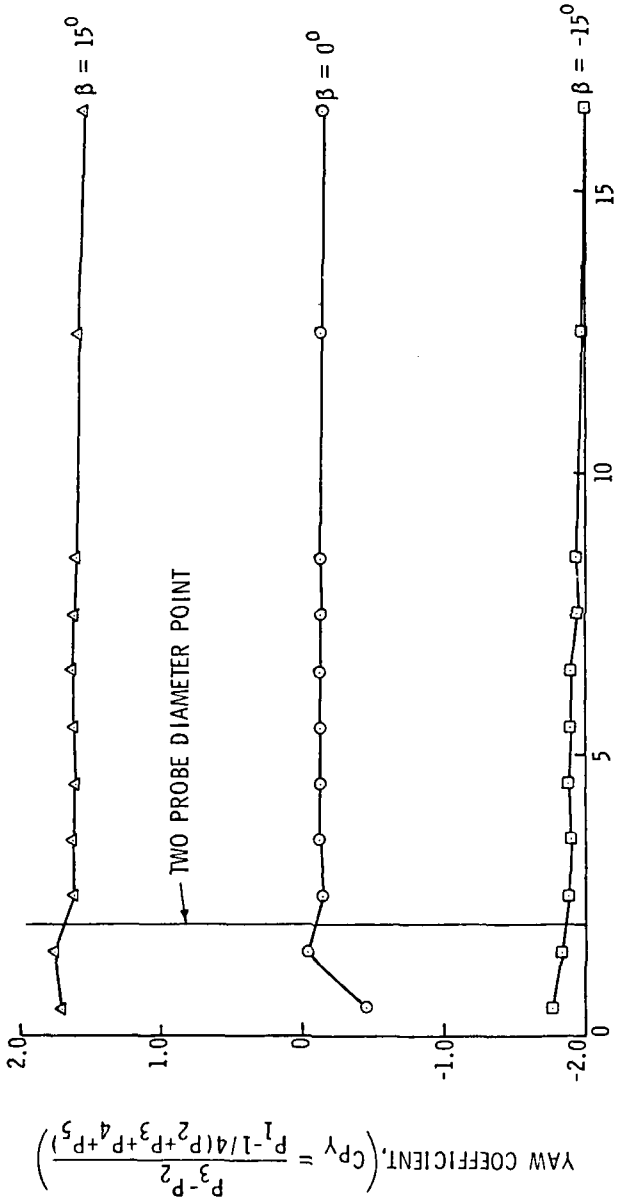

Figure 68. Yaw Coefficient Response to Wall Proximity Phenomenon

The procedure which is used in the data reduction process for the rotating probe surveys involves only the calculated yaw and pitch coefficients. Thus, the manner in which these parameters react to a close solid wall more accurately reflects the sensitivity of the data accuracy as a function of distance from the surface. Figure 67 shows that the pitch coefficient varies very little over the entire survey range and is affected the most when the probe is within two probe diameters. The effects of the solid wall on the yaw coefficient are perhaps more pronounced than on the pitch coefficient, but Figure 68 shows the region where the effects are greatest are again within two probe diameters for all three different yaw angle configurations. The conclusion which was drawn from the data obtained on the wall proximity phenomenon is that while, the data at any position from the solid blade surface is probably reasonably accurate, it is certain that the effects of the blade surface become negligible outside of two or three probe diameters.

5.3.4 Test Results. The results of the internal blade measurements are summarized in Figures 69 through 84. These figures are plots of the three components of normalized total velocity as a function of a nondimensional distance from the suction surface of the blade row. This normalized distance across the channel ranges from zero at the blade suction surface to unity at the pressure surface. The fact that some of the surveys start and end at points other than the extremes has been previously discussed in terms of blade twist and radial location. Each figure indicates the axial location of the survey which is plotted, along with the radius of the pressure probe which was used. The actual

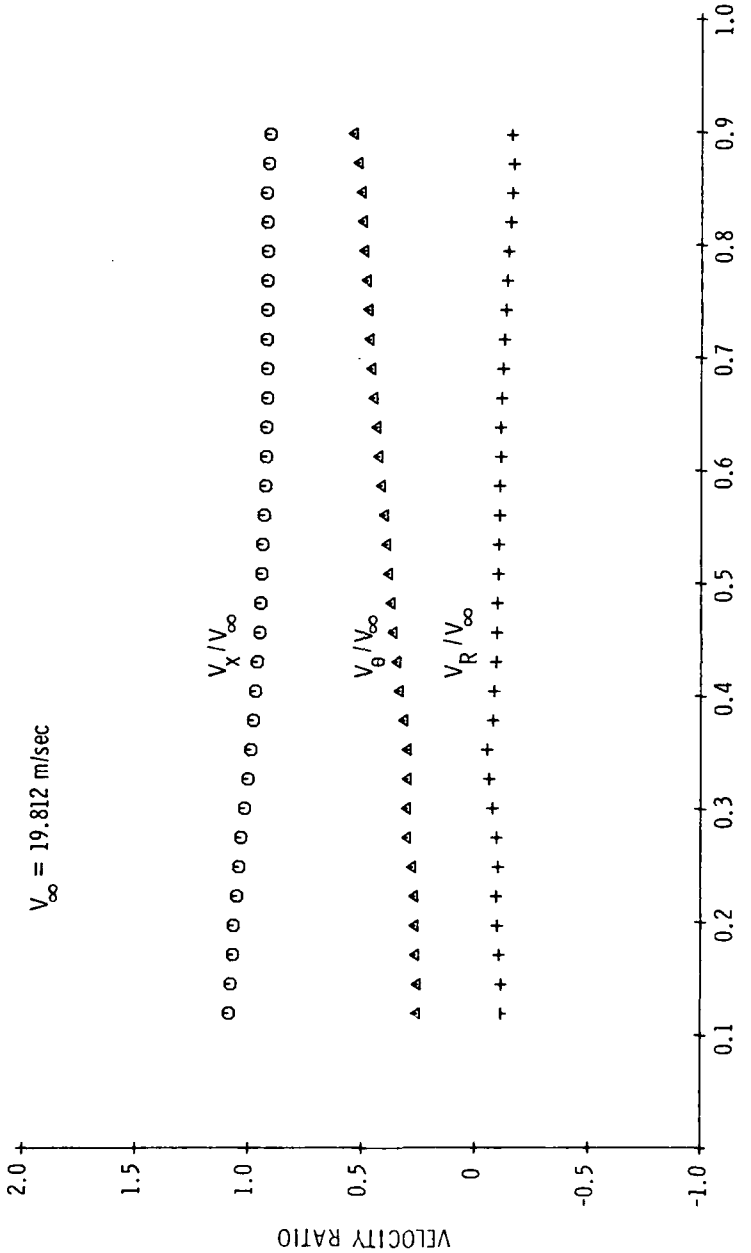

Figure 69. Rotating Pressure Probe Data - Passage Survey (Axial Station 1; Probe Radius 13.233 cm, Channel Width 7.452 cm)

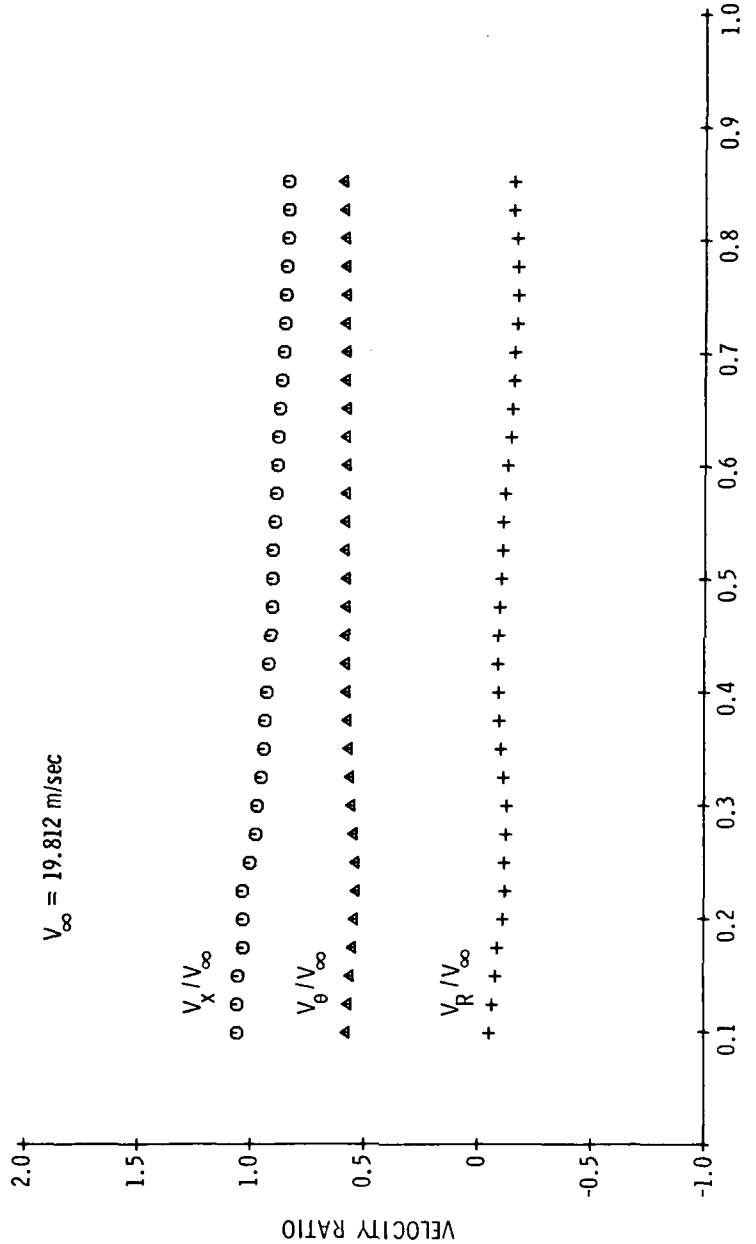

Figure 70. Rotating Pressure Probe Data - Passage Survey (Axial Station 2, Probe Radius 13.233 cm, Channel Width 7.706 cm)

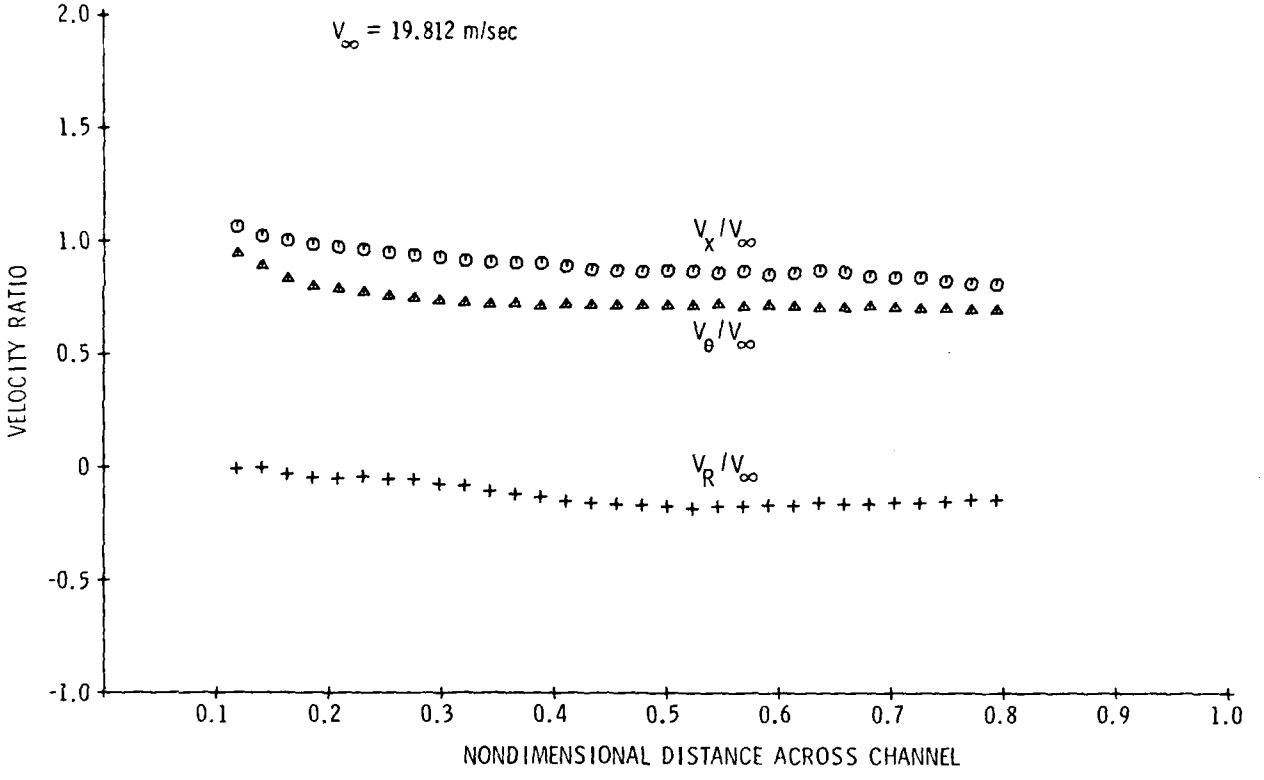

Figure 71. Rotating Pressure Probe Data - Passage Survey (Axial Station 3; Probe Radius 13.233 cm, Channel Width 8.595 cm)

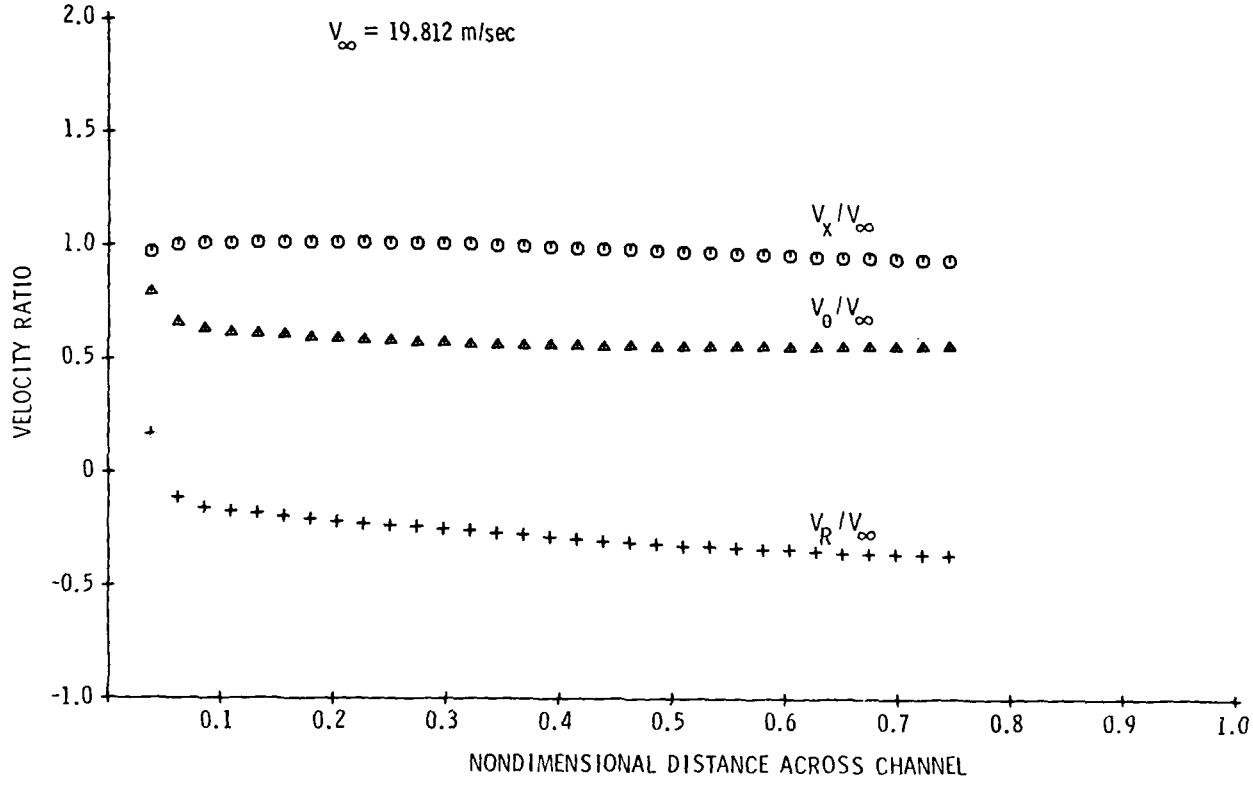

Figure 72. Rotating Pressure Probe Data - Passage Survey (Axial Station 3; Probe Radius 16.154 cm, Channel Width 9.992 cm)

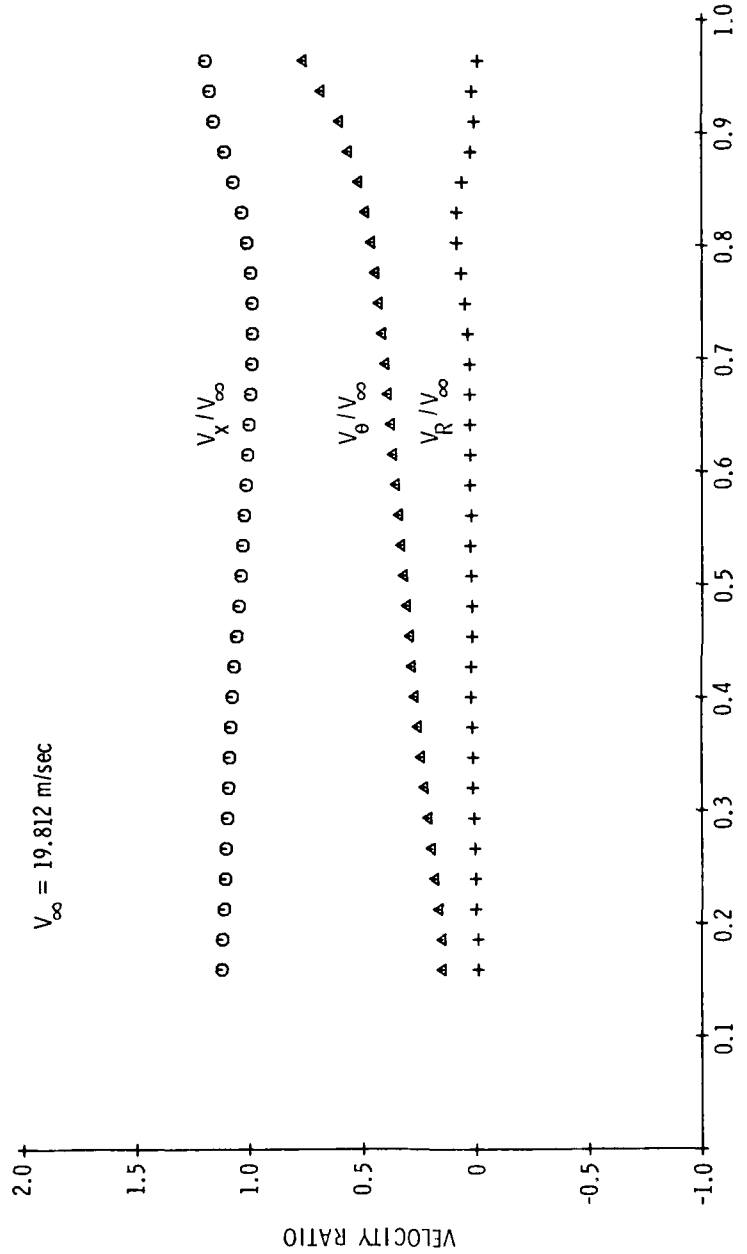

Figure 73. Rotating Pressure Probe Data - Passage Survey (Axial Station 1; Probe Radius 18.948 cm, Channel Width 10.376 cm)

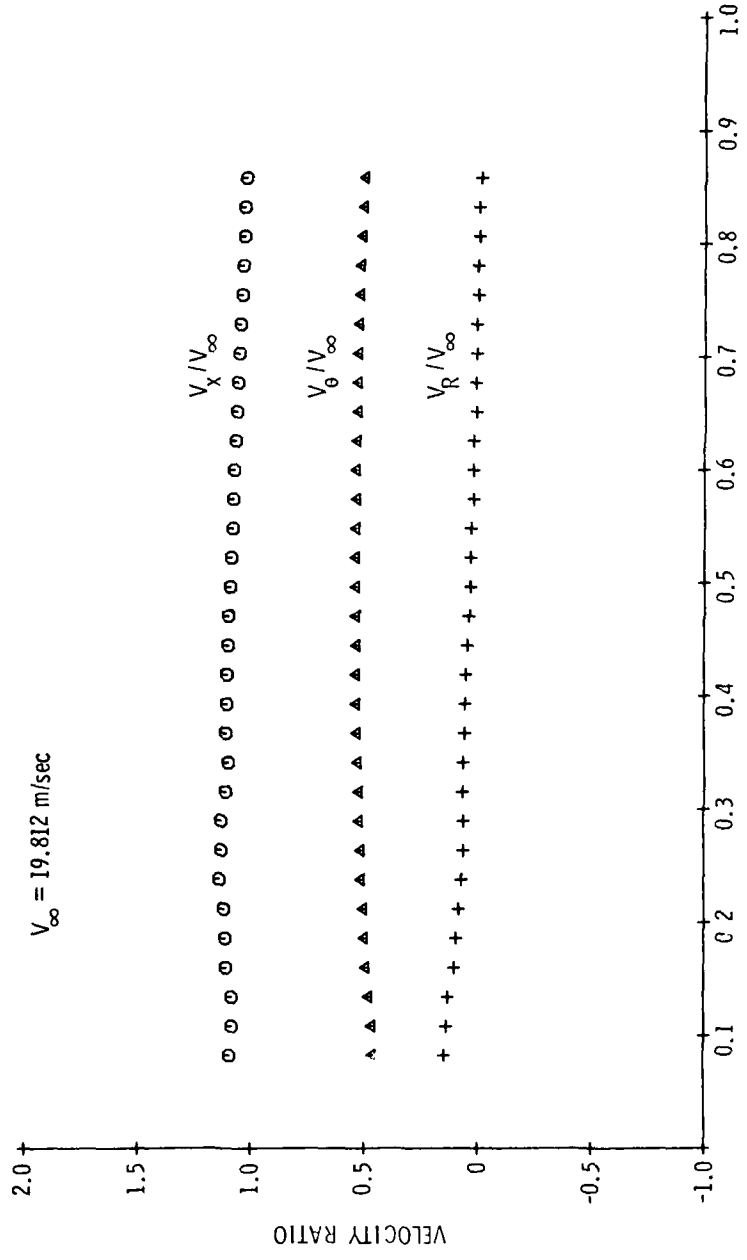

Figure 74. Rotating Pressure Probe Data - Passage Survey (Axial Station 2; Probe Radius 18.948 cm, Channel Width 10.755 cm)

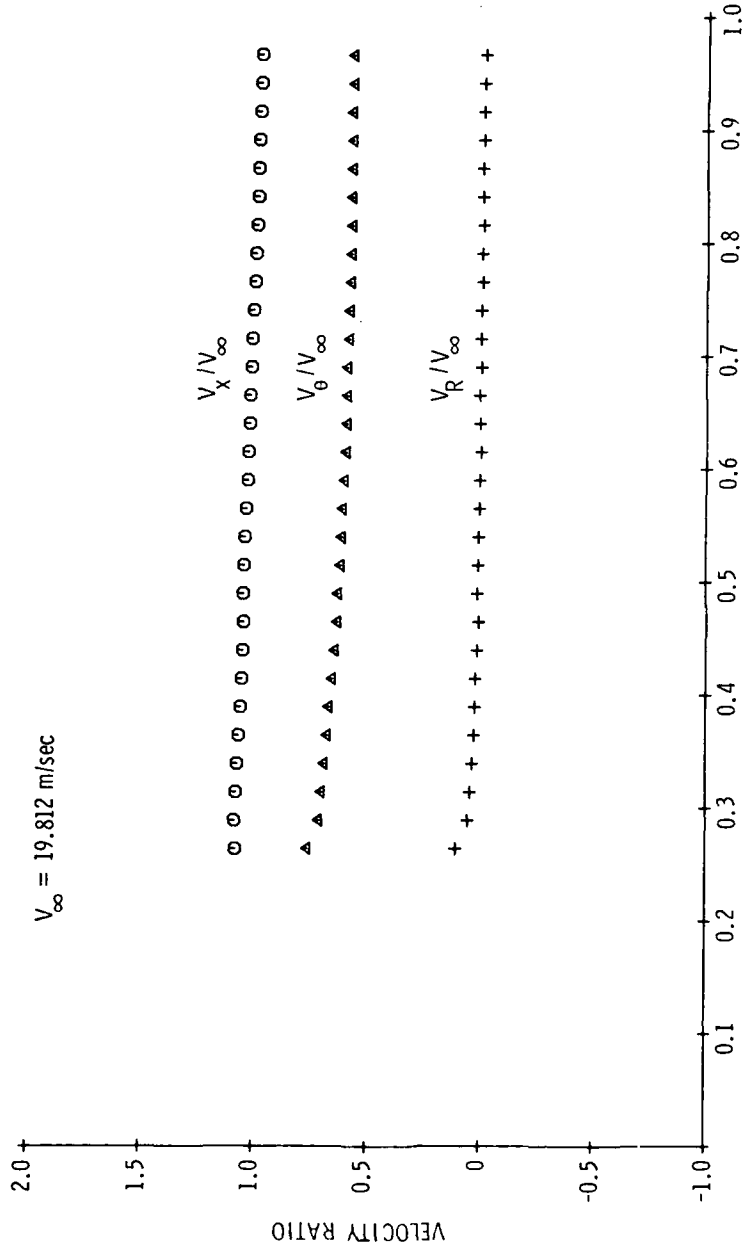

Figure 75. Rotating Pressure Probe Data - Passage Survey (Axial Station 3; Probe Radius 18.948 cm, Channel Width 11.087 cm)

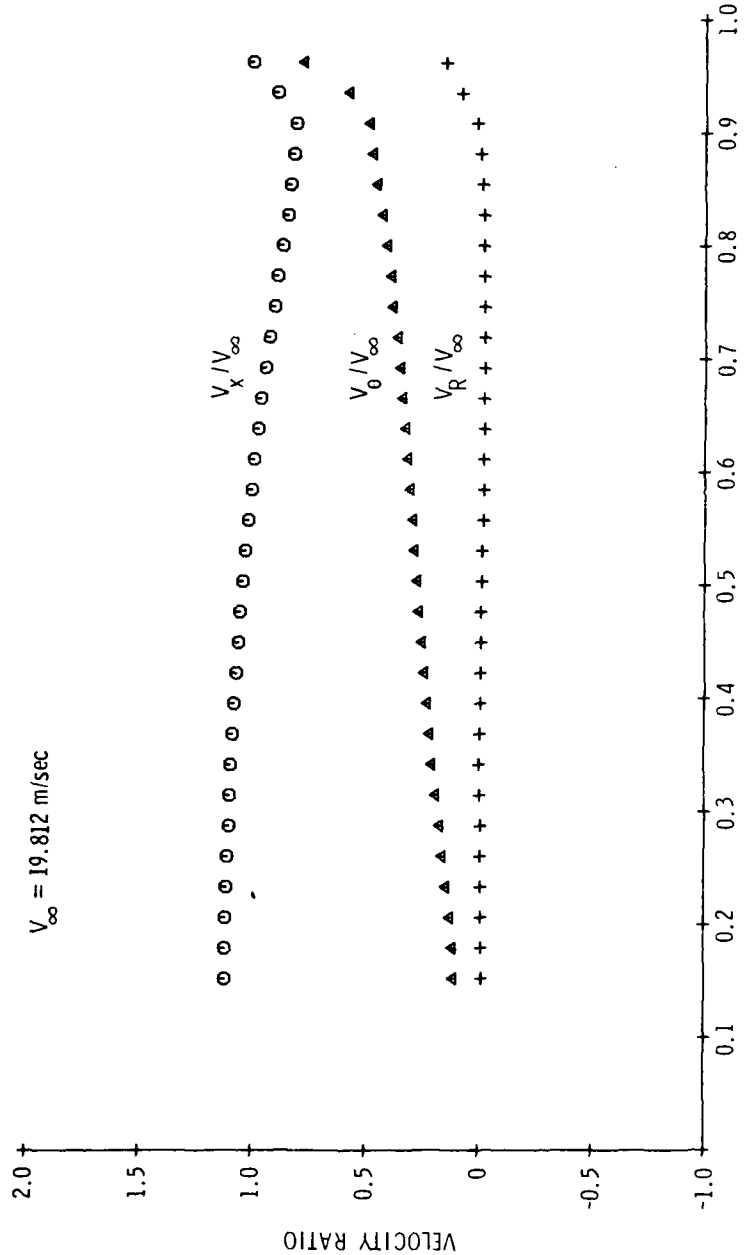

Figure 76. Rotating Pressure Probe Data - Passage Survey (Axial Station 1; Probe Radius 24.663 cm, Channel Width 13.368 cm)

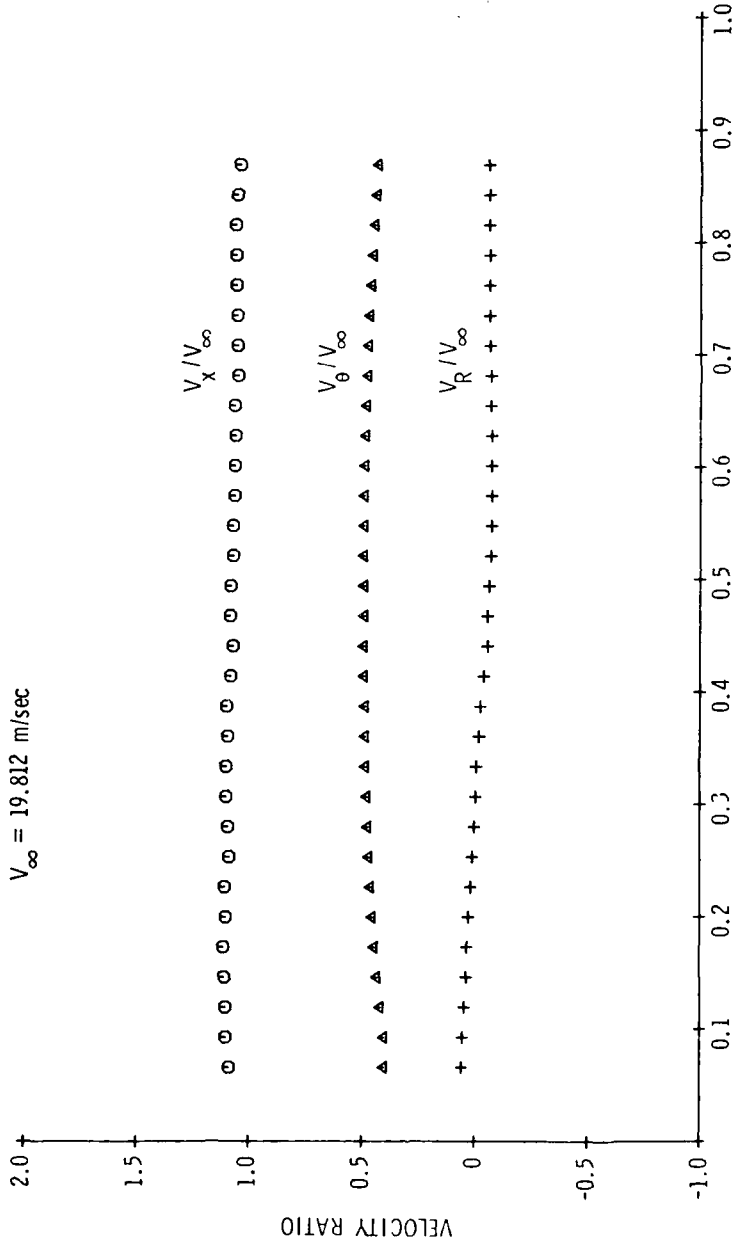

Figure 77. Rotating Pressure Probe Data - Passage Survey (Axial Station 2, Probe Radius 24.663 cm, Channel Width 13.495 cm)

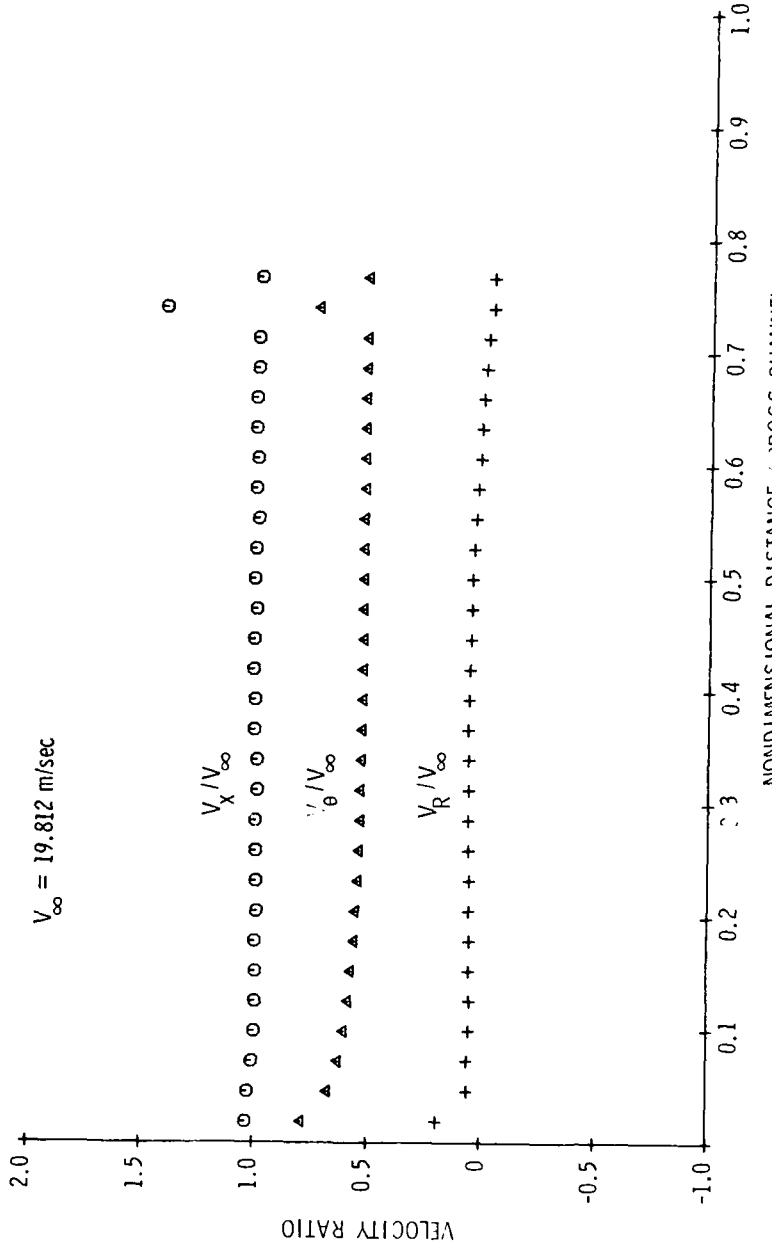

Figure 78. Rotating Pressure Probe Data - Passage Survey (Axial Station 3; Probe Radius 24.663 cm, Channel Width 13.535 cm)

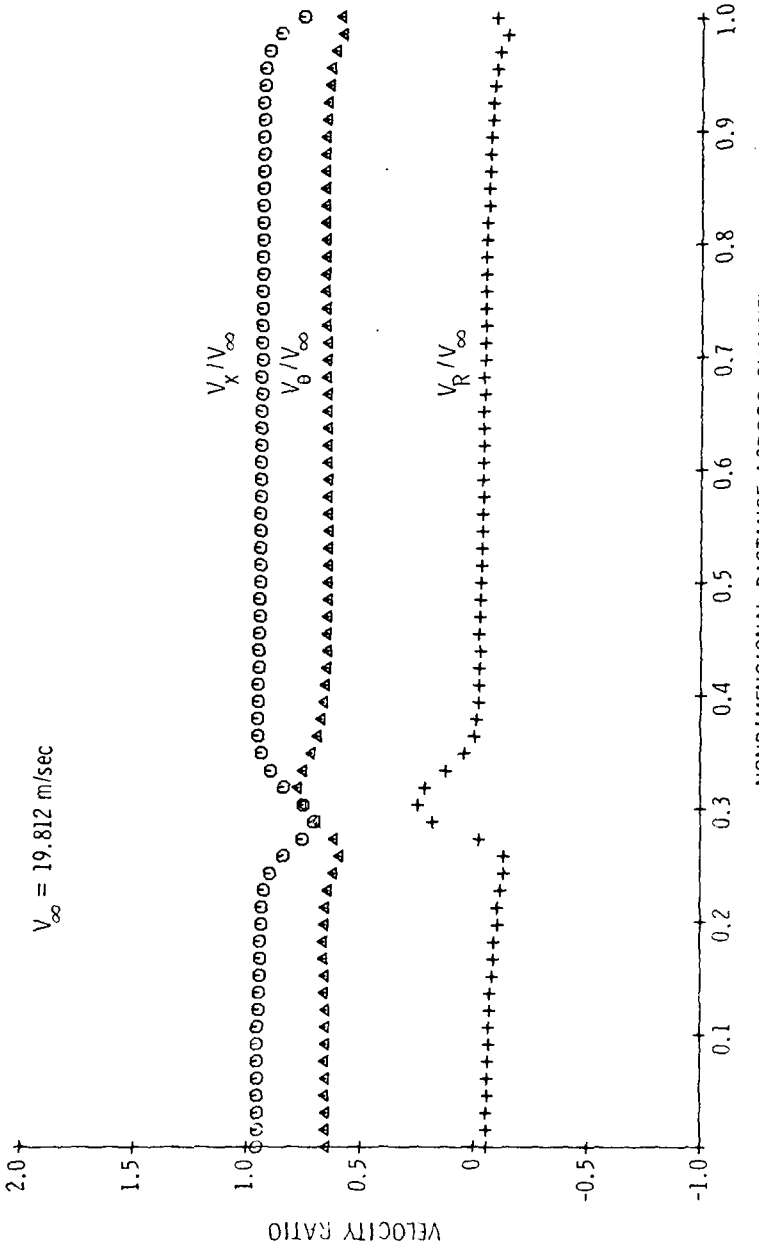

Figure 79. Rotating Pressure Probe Data - Wake Survey (Axial Station 4; Probe Radius 16.154 cm, Channel Width 15.557 cm)

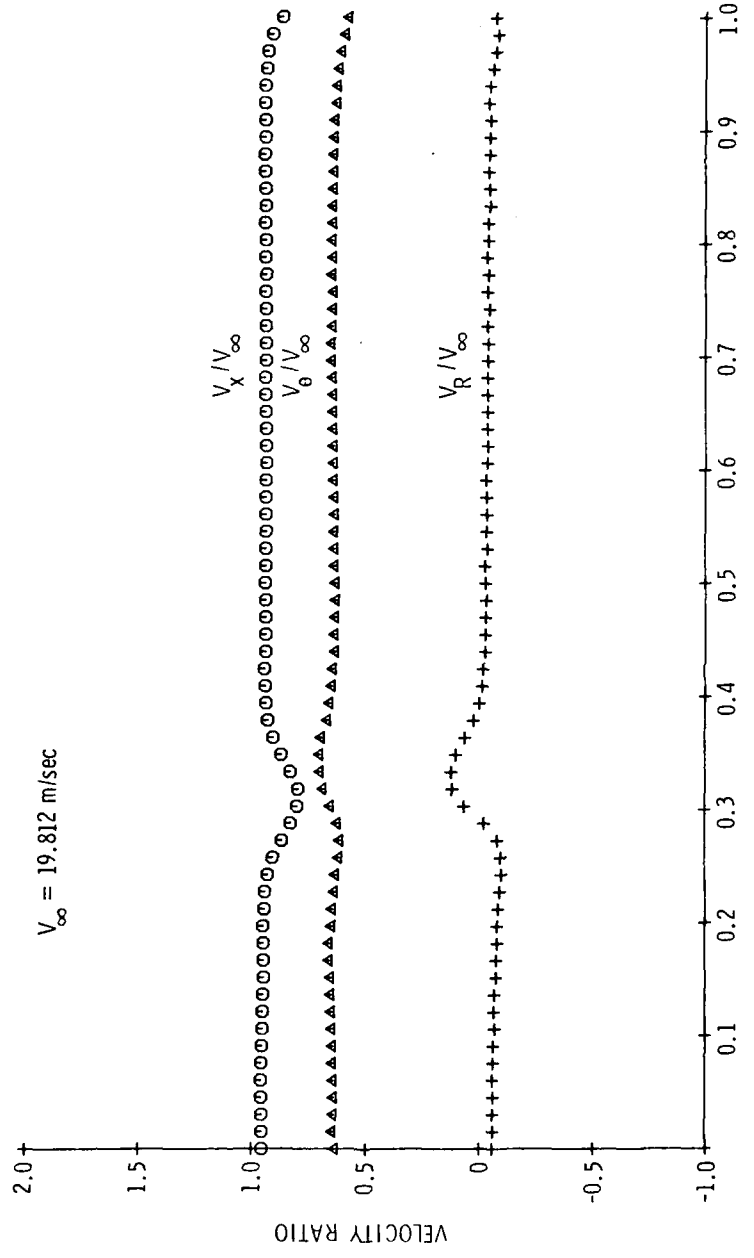

Figure 80. Rotating Pressure Probe Data - Wake Survey (Axial Station 5; Probe Radius 16.154 cm, Channel Width 15.557 cm)

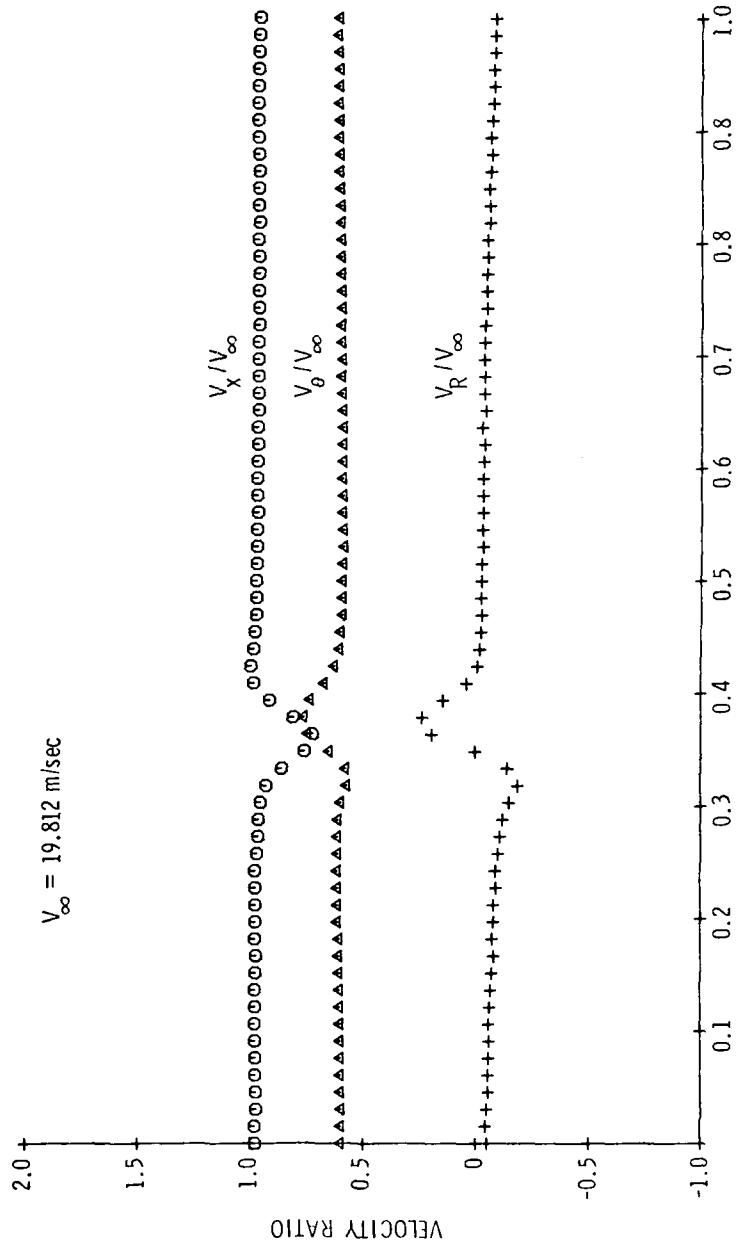

Figure 81. Rotating Pressure Probe Data - Wake Survey (Axial Station 4; Probe Radius 18.948 cm, Channel Width 18.351 cm)

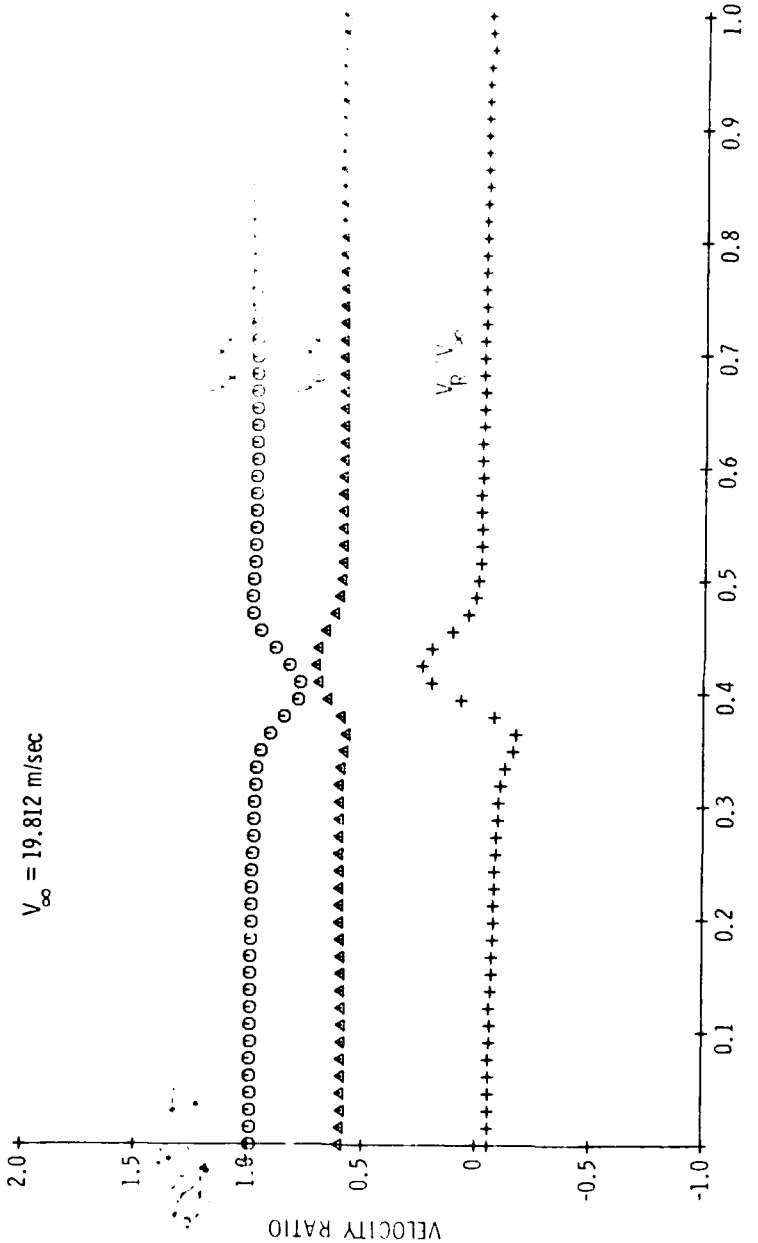

Figure 82. Rotating Pressure Probe Data - Wake Survey (Axial Station 5; Probe Radius 18.948 cm, Channel Width 18.351 cm)

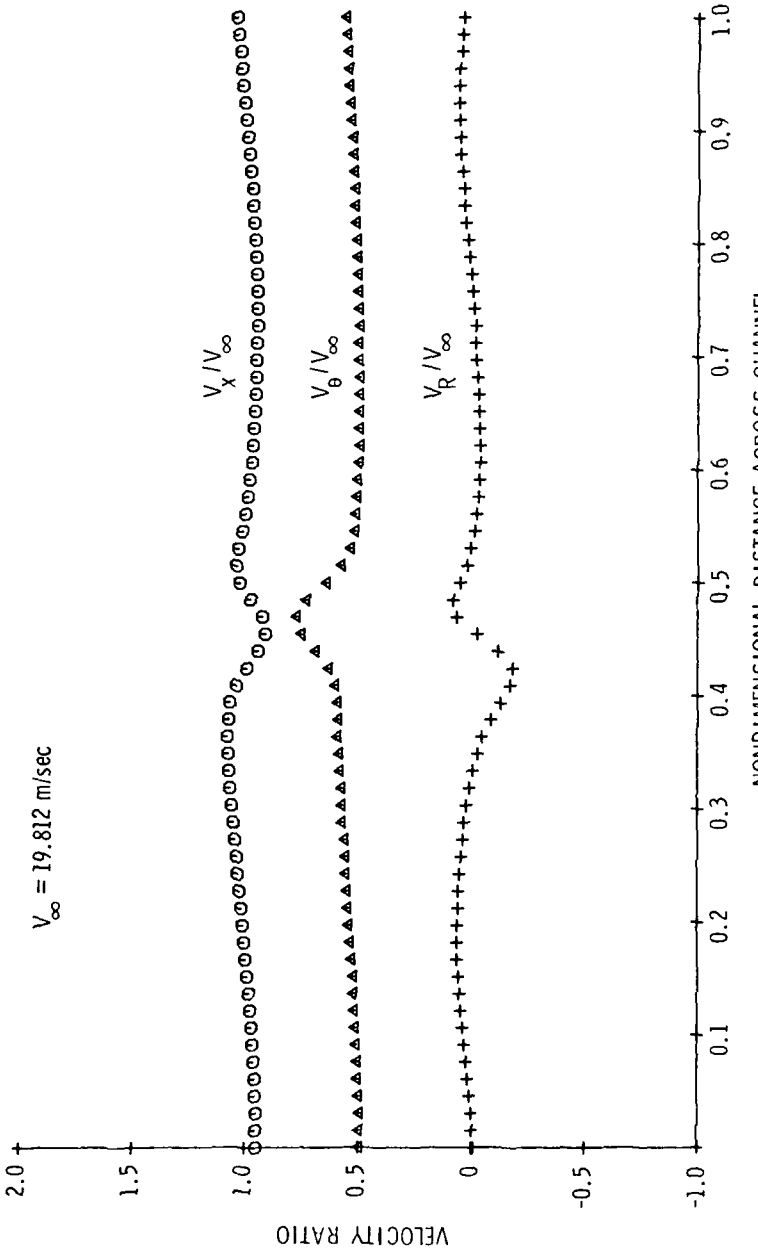

Figure 83. Rotating Pressure Probe Data - Wake Survey (Axial Station 4; Probe Radius 24.663 cm, Channel Width 23.822 cm)

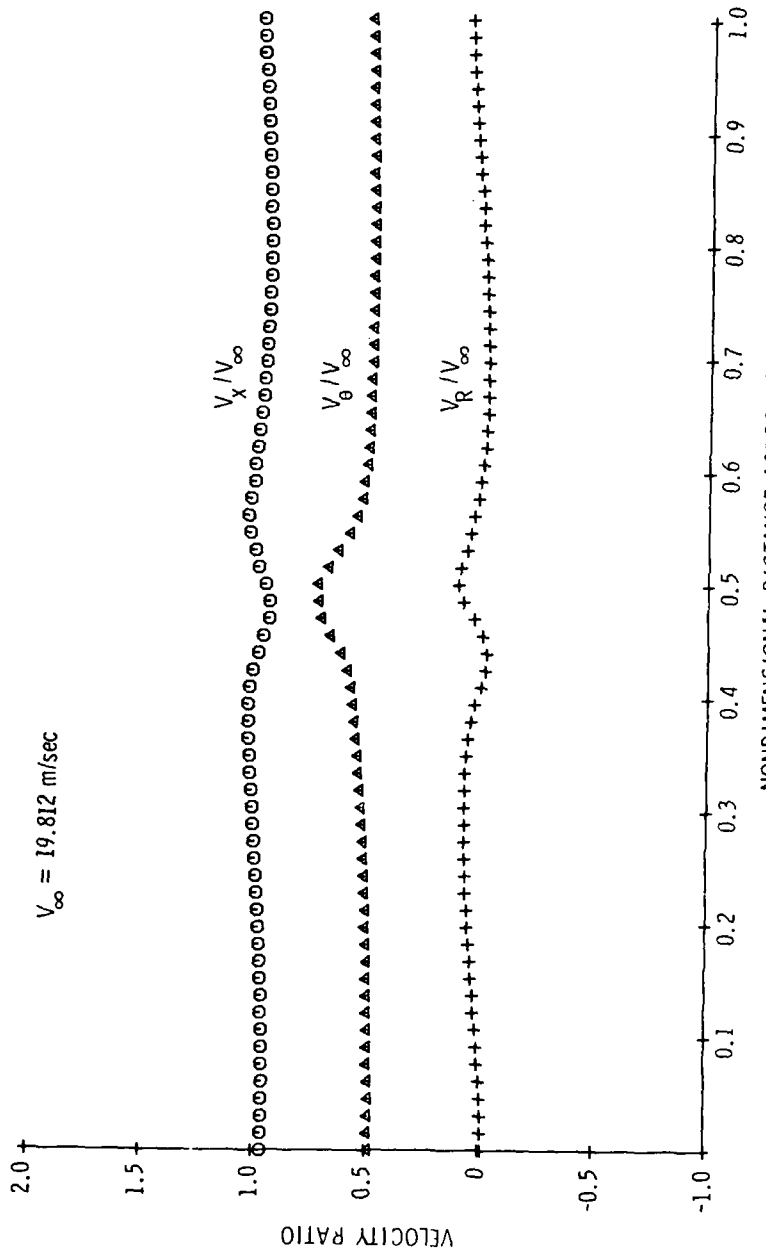

Figure 84. Rotating Pressure Probe Data - Wake Survey (Axial Station 5; Probe Radius 24.663 cm, Channel Width 23.822 cm)

channel width for each survey is also included in each figure. This distance is an arc length based on the stepping increment used and the radius of the probe. All rotating pressure probe surveys were conducted at the design mass flowrate condition for the AFRF test rotor which corresponds to the design flow coefficient. The presentation sequence of the test data is such that all the internal blade passage data, axial stations one through three, are grouped and shown at a constant probe radial location. The two wake survey stations are arranged in a similar fashion so that the change in velocity components as the flow moves through the rotor at a given radius may be viewed easily. Due to the apparent existence of very large flow angles and possible regions of flow separation near the rotor trailing-edge, the smallest probe (R = 13.288 cm) could not handle the flow field downstream of the third axial station. All of the five-hole pressure probes are calibrated for flow angles of ±30 degrees in both the yaw and pitch planes. The 60-degree spread is usually considered more than ample for normal design speeds, however, in this region of possible flow separation, the range was not sufficient. So as not to lose the remaining downstream wake data due to this unusual condition, an additional probe (R = 16.154 cm) was used to obtain the wake survey data in place of the smaller probe.

If Figures 69 through 78 are viewed in groups of constant radii, there are a few interesting trends which seem to develop from the data. The first point of interest is the somewhat constant nature of the blade-to-blade axial velocity profile. This uniformity is observed at all three internal stations and at each radial position indicating that there should be little, if any, change in axial velocity from

leading- to trailing-edge. Since all the values of the axial velocity ratio center themselves around unity, it is also probable that the data were collected outside of the hub and casing boundary layers. The second trend which can be pointed out by these data is the manner in which the tangential velocity component, which has been transferred to the absolute reference frame, changes from leading- to trailing-edge and from blade to blade. At each radial position, the magnitude of the circumferentially averaged tangential velocity increases as the flow moves through the passage. This trend is obviously shown, but more importantly, the change in this velocity appears to be greater from station one to station two than from station two to station three. This trend is revealed at each radial position and indicates that the fluid turning is not distributed uniformly from leading- to trailing-edges, but rather a greater percentage occurs in the front portion of the blade than in the aft portion. Another feature of the tangential velocity profile is that, at a constant radius, the first station exhibits a gradual increase from suction to pressure surface, while the remaining stations show rather constant blade-to-blade profiles. Again, this phenomenon is repeated at each radial position. The last important piece of information that can be observed from these blade passage data plots is the size of the radial velocity component. These profiles for all of the radial locations hover around the zero value and are thus considered as a negligible velocity term.

In addition to the internal blade passage data, the plots of the wake survey data indicate some interesting trends. Figures 79 to 84 show the three components of velocity through the wake of one blade. The reason that only one blade wake was traversed is that the flow

angles are relatively large in these areas behind the trailing-edge, and although the probe physically traversed two blades, only one wake, and sometimes the start of the next, was recorded. These wake data show an axial velocity deficit occurring in an otherwise circumferentially uniform flow field downstream of the blade passage. Also evident in this region is a vortex-like tangential and radial velocity distribution similar to data collected by Hirsh and Kool [24], and Raj and Lakshminarayana [25]. At each of the three radial positions, it is evident from these data that as the flow moves downstream the blade wakes are filling in and the flow is tending toward some circumferential uniform velocity profile of all three components. It is interesting to note that the magnitudes of the axial velocity deficit at the lower- and mid-radial locations are equal, or very nearly equal. This is not the case with the tip radius profile. Here, the axial velocity deficit is less pronounced and decays more rapidly as the flow progresses downstream. A possible influencing factor in this region may be the tip leakage vortex which is shed from the blade row. This vortex would increase the fluid mixing in this region and could cause an increase in the wake decay rate. One factor which leads to this possibility is the rather pronounced vortex-like behavior of the radial velocity component at this tip radius location.

To verify the quality of the rotational data, a comparison is made with the stationary flow field data. The axial positions of the two surveys differ considerably; however, it is possible to obtain some qualitative information concerning the data. Figure 85 is a plot of axial velocity ratio as a function of the axial distance from the leading-edge blade-hub intersection point normalized by the aerodynamic

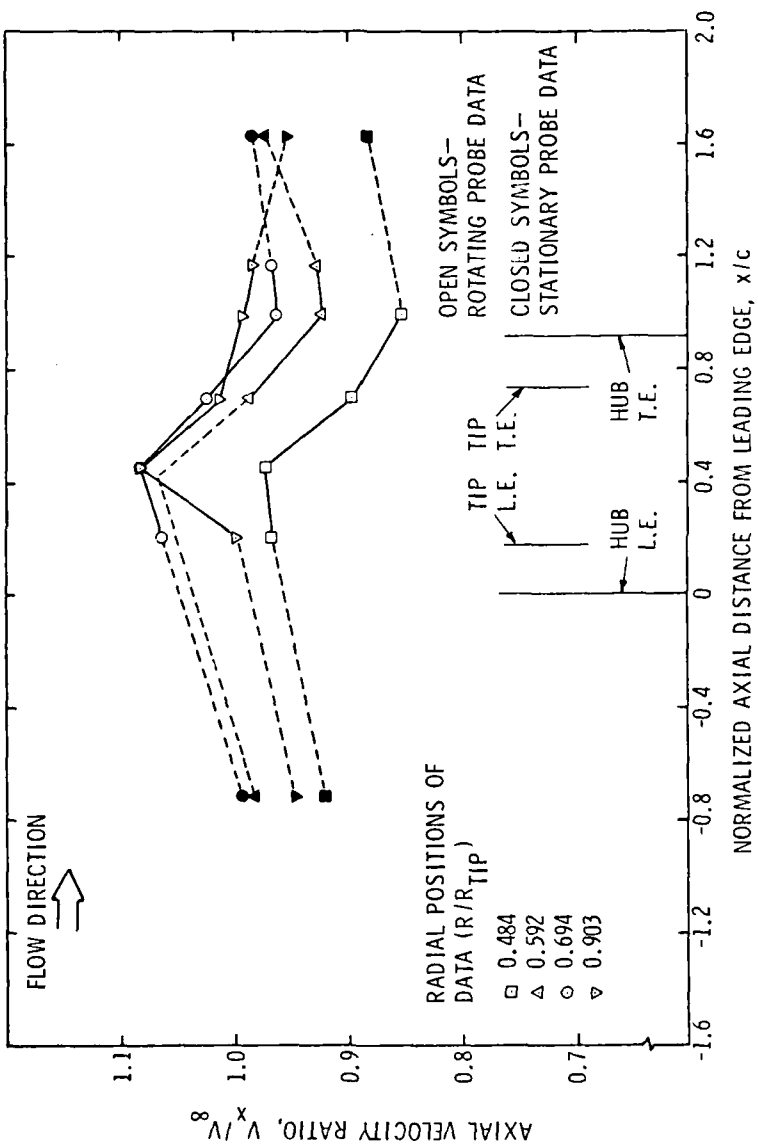

Figure 85. Measured Axial Velocity Profile Through the Blade Row

chord of the rotor. In this figure, both the stationary probe data and rotating probe data are compared. The blackened symbols represent the measurements conducted in the stationary reference frame, while the open symbols represent the rotational reference frame data. The indicated axial positions for the rotor leading- and trailing-edges are shown for the hub and tip sections. With the large amount of radial twist which is present in this rotor, the axial positions of the blade edges varies from hub to tip and must be considered when analyzing the experimental data.

Figure 85 indicates the general distribution of axial velocity both in the hub-to-tip plane, as well as in the axial direction through the blade row. The upstream stationary data indicates that two of the data points are on the edge of the inlet boundary layer giving rise to the lower velocities, and two are in the uniform portion of the profile. As the flow path is traced through the rotor for the first radial position, indicated by the squares, one notices a small region of acceleration around the leading-edge and then a marked deceleration toward the aft portion of the blade. The dashed symbol shown at the fourth station through the blade row is the location where large flow angles presented measuring problems. This point is an approximate average of the data which was considered usable; however, its accuracy is questionable. This is the region in which a possible flow separation is suspected to have occurred and, based on the large decrease in axial velocity just upstream of this point, the justification of such a suspicion is evident. The other extreme radial position, indicated by the inverted triangle, is at the tip section. The velocity trend at this location is to accelerate dramatically over the leading-edge

and then decelerate to outlet velocity which is still higher than the inlet condition. The two data points in the mid-span region experience this same large acceleration followed by a gradual deceleration to some final free-stream value. The data points represented by the triangle are those surveys conducted with the backup probe used to measure the downstream wake profiles when the flow separation phenomenon prohibited the use of the smaller (R/R_{TIP} = 0.484) probe. It is for this reason that data do not exist for the first two intra-blade stations for this probe. However, given the trend of the data which was obtained and the trends of the other radial locations, the upstream dotted lines are included in the plot but no data point is shown. It is interesting to see this large acceleration of the axial velocity occurring at the same axial position through the blade passage for each radial position. The reason for this large acceleration is due to the nature of the rotor design. The blades are designed with circular-arc camberlines and a C1-thickness distribution and are stacked along a radial line at 50 percent of the chord. This combination produces a point of maximum thickness at the stacking point. Thus, the point at which the flow channel area is the smallest occurs along a radial line which is half way between the blade edges. This point of maximum blockage thereby produces the observed flow accelerations.

Figure 86 is a plot of the tangential velocity profiles from both the stationary and rotational flow surveys. This figure, unlike Figure 85, traces the flow field from the blade row leading-edge but does not include the swirl-free upstream flow field. The experimental data show a definite trend as the flow progresses through the passage. First, as one would expect from this free-vortex designed rotor, the

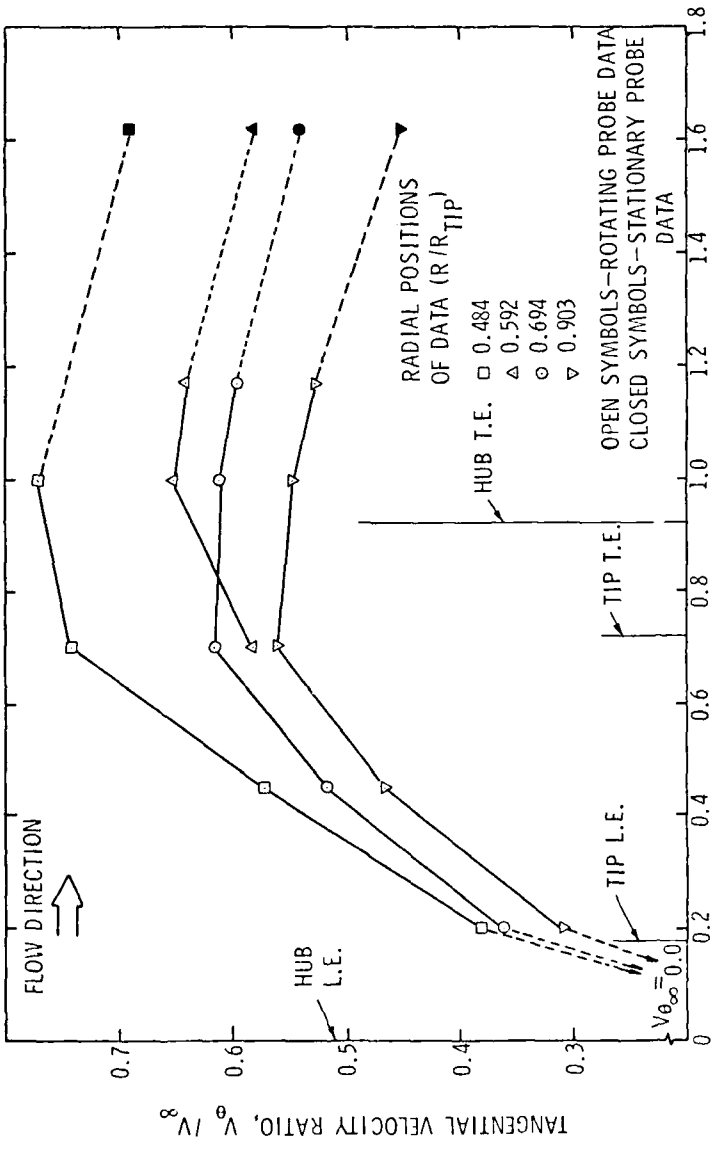

Figure 86. Measured Tangential Velocity Profile Through the Blade Row

tangential velocity is greatest at the hub radii and decreases steadily as the tip radii are approached. There is one data point which does not follow this trend, however. The reason for this deviation from the trend is not fully understood; however, this point is within the region that is thought to have separated at the lower radius and thus may have had some influence on the flow field at this slightly higher position. The other interesting data trend is the manner in which the turning and, hence, tangential velocity, changes as it passes through the blade row. The slopes of the lines which connect the data points decreases with axial distance. This indicates that the fluid is turned very quickly by the front portions of the blade and then experiences only slight turning over the back portions. From these experimental data, the actual distribution of turning through the blade passage, as shown in Figure 87, can be determined and used in the SLC analysis program to predict the internal flow field more accurately than the straight line approximation previously used. Another interesting trend that can be seen in Figure 86 is the decay rate of the tangential velocity values outside of the blade passage. The straight lines connecting the downstream stationary survey data and the rotating wake survey data appear to have nearly equal slopes. This indicates that the decay rate of the tangential velocity, due to viscous effects, is linear and constant with axial distance for all radii.

The data presented in Figures 85 and 86 are, within the experimental accuracy of the instrumentation, representative of the actual flow field which exists upstream, downstream, and inside the blade passage of the AFRF test rotor at the design mass flow. The rotational survey data points are a circumferential average of the more than 100

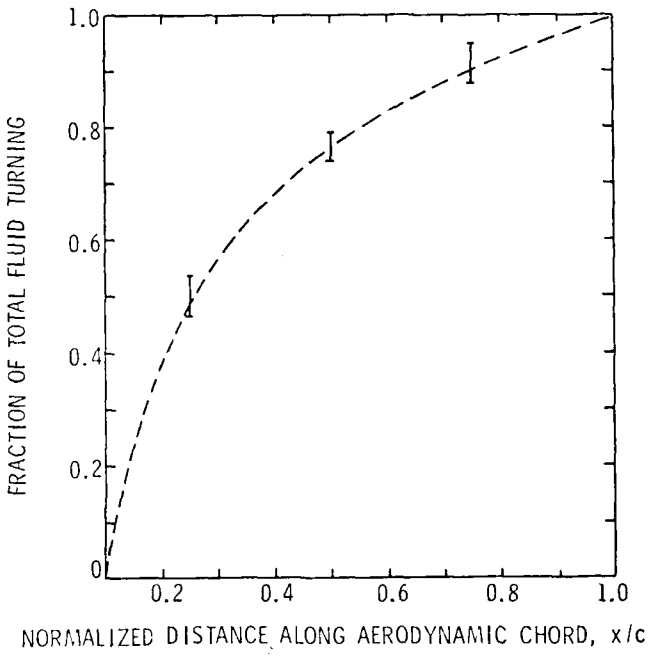

Figure 87. Proposed Chordwise Loading Distribution Based on Intra-Blade Flow Field Data

individual survey points obtained from blade to blade at each radial position. The stationary survey data points are the average of four individual experimental points and it is assumed that these values are circumferential averages of an axisymmetric flow field. In general terms, it appears that the two separate flow field surveys are compatible and Figures 85 and 86 show no gross discontinuities or apparent inaccuracies in the data.

6. DISCUSSION OF RESULTS

The two phases of this investigation, the numerical analysis of the AFRF test rotor and the experimental evaluation of the actual hardware, have been completed. The analysis of the AFRF flow field using the axisymmetric streamline curvature computer code has been compared to available design data as a preliminary indication of the accuracy of the technique. These comparisons have shown that the SLC analysis is able to predict the design parameters for this test rotor reasonably well. The purpose of this investigation, however, is to examine how well the SLC analysis is able to predict the actual flow field parameters. The experimental phase of this investigation provides the necessary detailed flow field data which are used as the basis for all of the accuracy comparisons.

The overall accuracy of the SLC analysis method is indicated rather well by Figure 88. This figure represents a comparison between the measured profiles of axial and tangential velocity and the SLC predictions of the axial and tangential velocity profiles at the downstream measuring station. The important parameter which a turbomachinery designer would like to be able to predict accurately is the turning of the fluid as it passes through the blade row. Since this turning is directly related to the outlet tangential velocity profile, Figure 88 shows that the SLC analysis does predict the measured turning very well. There are some points of discrepancy between the measured and predicted axial velocity profiles shown in Figure 94. The largest deviation in the two axial velocity profiles occurs near the blade tip where the SLC outlet flow angle

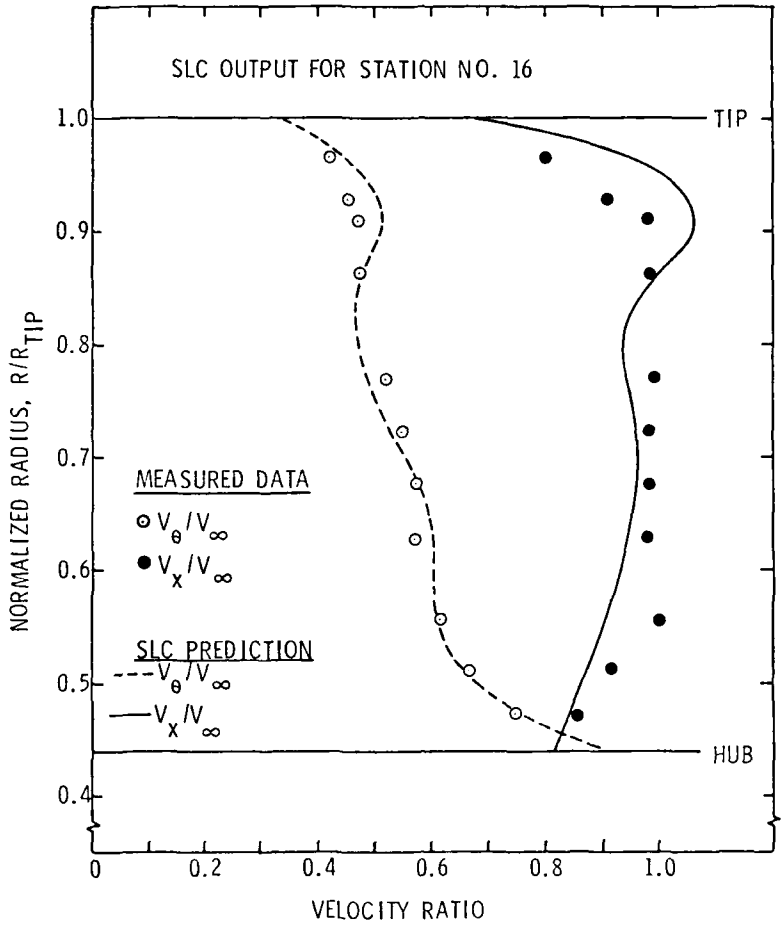

Figure 88. Comparison of Streamline Curvature Prediction and Measured Flow Field

calculations are the weakest. The general shape of the rest of the profile, however, is not very much different from the measured profile. Overall, the degree of accuracy which is indicated by Figure 88 would suggest that the SLC technique is probably acceptable as it now exists, but further investigations are definitely needed to examine off-design capabilities and other rotor configurations.

The surface static pressure measurements are compared to the Douglas-Neumann analysis results in Figures 89 through 91. Since the static pressure taps are not located at radial positions coinciding with the design blade section, there is a small difference as to the radial locations of the measurements and predicted values in these figures. For the sake of comparison, the blade section closest to the pressure tap radial location is used in these figures. Even though the Douglas-Neumann analysis is a potential flow solution, the agreement between measured and predicted pressures is very good. The results of the numerical analysis consistently over-predicts the measured surface static pressure on each blade surface. The phenomenon is most likely due to the inviscid nature of the analysis. The other interesting point about the D-N results is that the pressure becomes very large around the leading edge of the blade section, possibly due to the inability of the program to handle the stagnation region. This is a minor point as long as detailed information around the leading-edge is not required. Pressure diagrams, like those shown in Figures 89 through 91, are an important part of the design process. These distributions, if accurate, can be used to determine the aerodynamic loads that are present on the blades and thus allow stress analyses to be conducted. Whether or not the designed blades will withstand

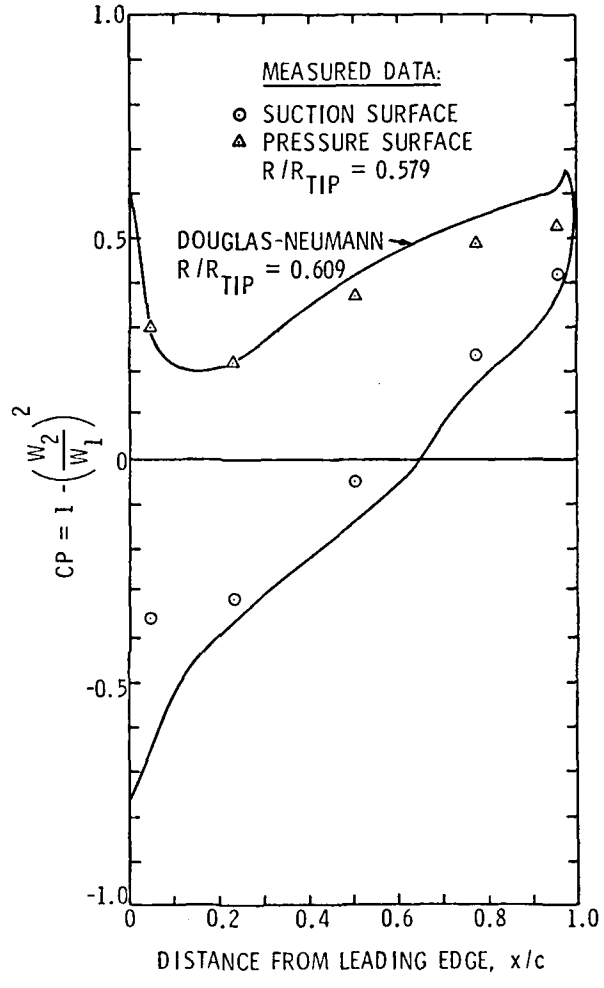

Figure 89. Comparison of Blade Surface Pressure Data

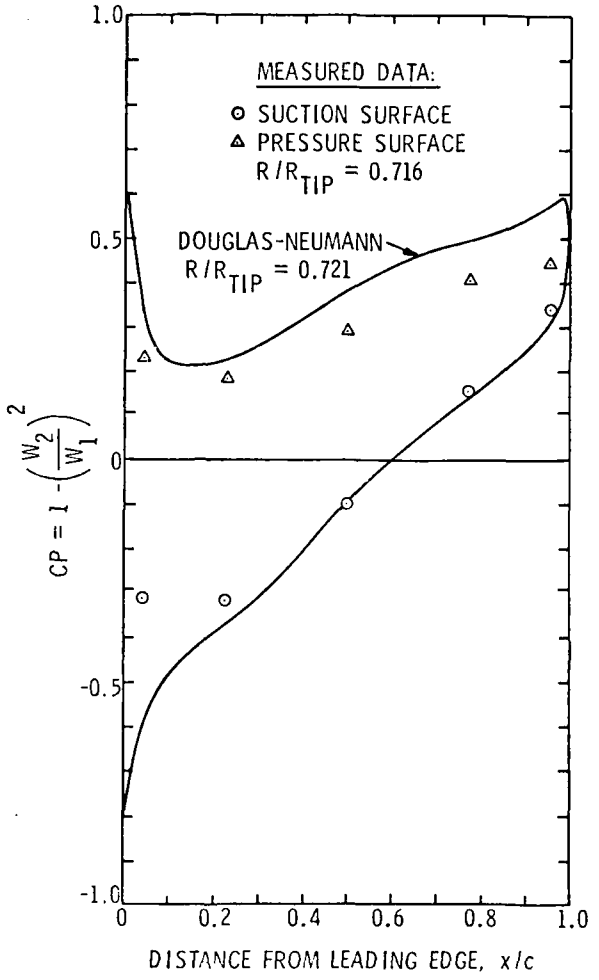

Figure 90. Comparison of Blade Surface Pressure Data

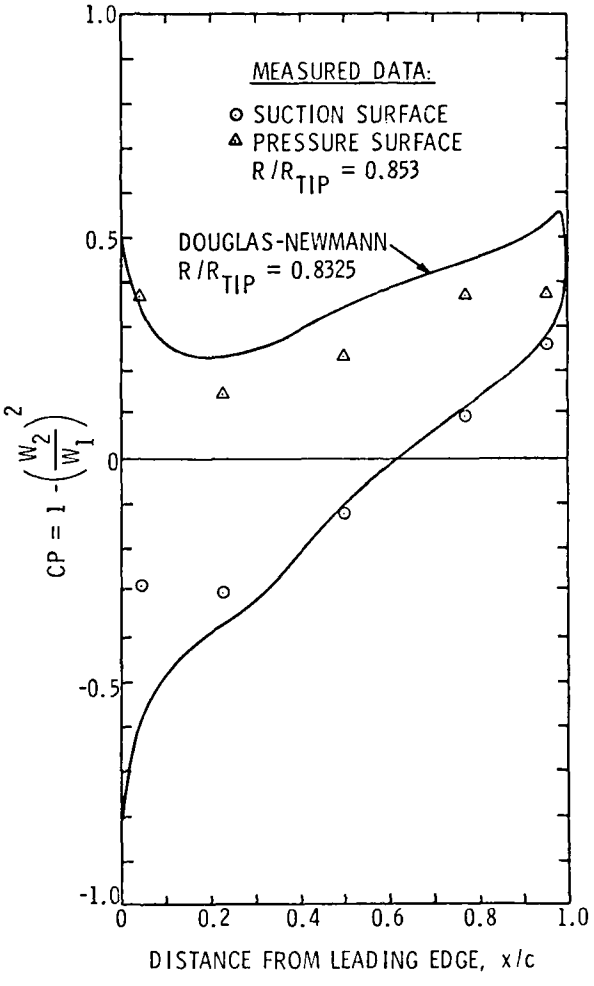

Figure 91. Comparison of Blade Surface Pressure Data

the high aerodynamic and centrifugal forces is a determining factor relative to the feasibility of the overall design.

The additional blade-to-blade analysis using the streamline cu ture computer code provides information about the channel flow fiel which the Douglas-Neumann technique does not provide. The SLC blad blade solution of the flow field predicts the velocity profiles acr the blade passage as well as the surface pressure distributions. Unfortunately, it has previously been mentioned that this new porti of the SLC code is not functioning properly and requires more time a more complete investigation of the problems. Once this facet of the SLC analysis is solved, there are experimental data from this s which can be used for verification. The usefulness of the SLC code the axisymmetric and blade-to-blade solutions is displayed in the relative ease of coupling the analyses to form a technique which iterates between the two solutions and forms a quasi-three-dimensio analysis.

Predicting the hub-to-tip flow inside the blade row is not a s task without some indication of how the fluid turning is distribute along the blade chord. From the experimental measurements conducte through the blade row, it is possible to determine the loading distribution. Figure 87 shows a radial average of total fluid turni as a function of chord which has been deduced from the experimental blade-to-blade data. Figure 92 shows the streamline pattern throug the AFRF facility, as well as the calculating station lines for the SLC analysis. This loading distribution is used in the SLC axisym-metric hub-to-tip flow field solution and the results are shown in Figures 93 through 97.

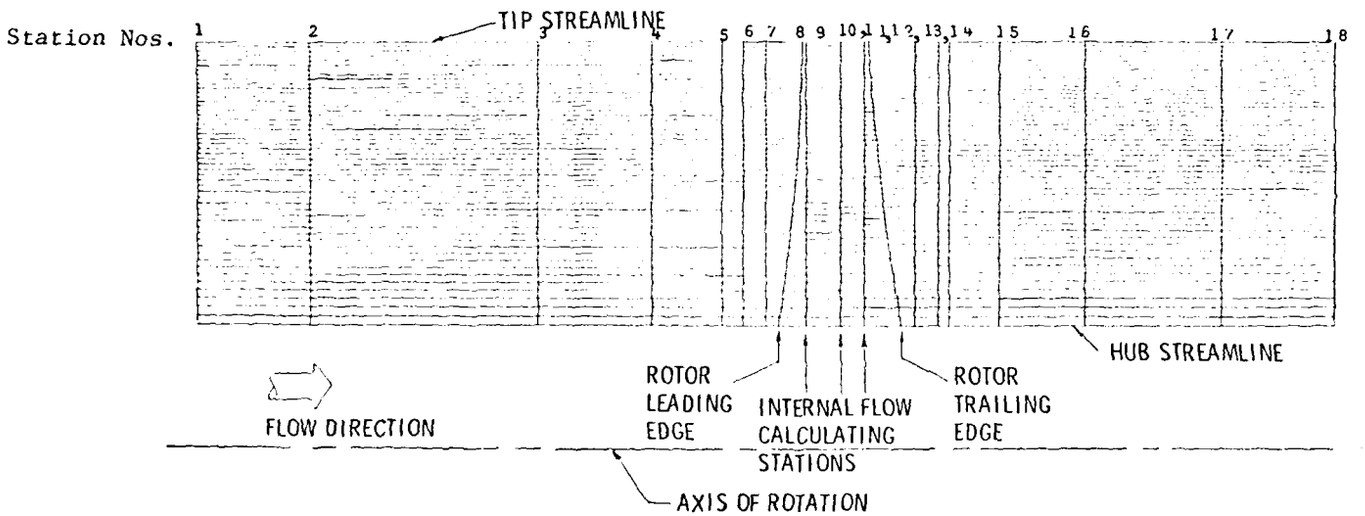

Figure 92. AFRF Flow Geometry for Streamline Curvature Axisymmetric Analysis

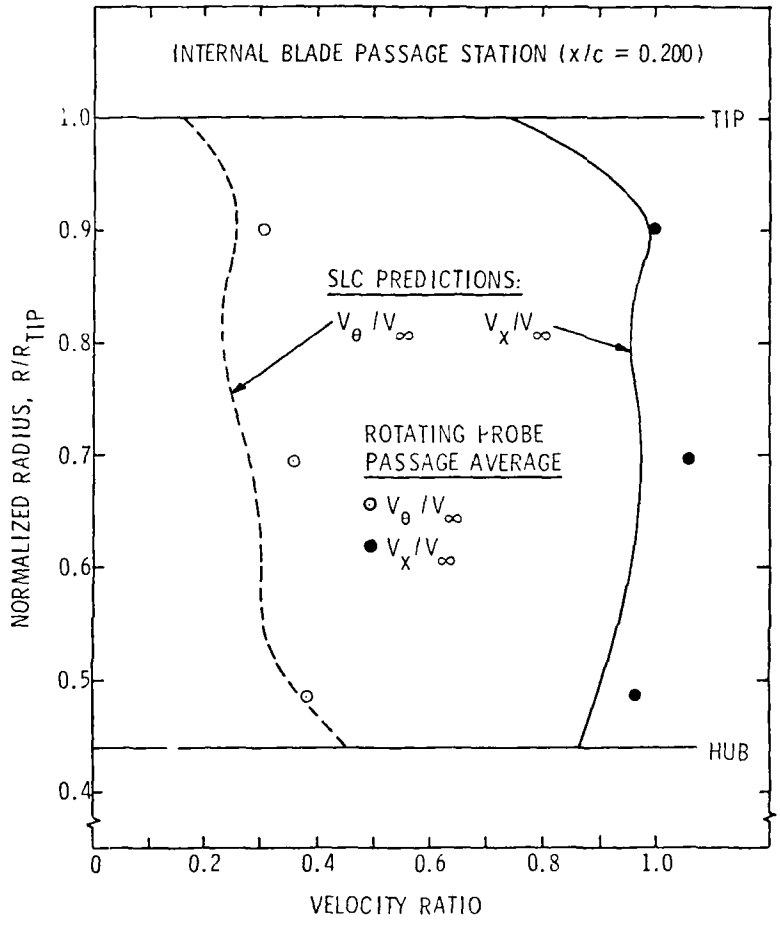

Figure 93. Comparison of Streamline Curvature (SLC) Prediction and Measured Flow Field Survey for Internal Blade Station No. 9

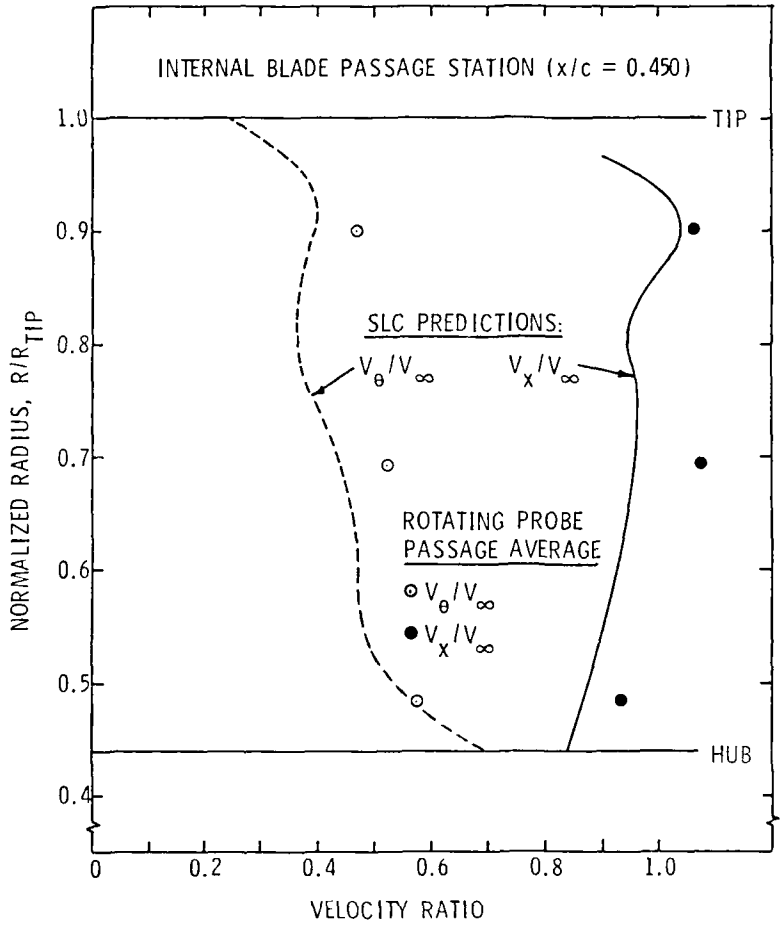

Figure 94. Comparison of Streamline Curvature (SLC) Prediction and Measured Flow Field Survey for Internal Blade Station No. 10

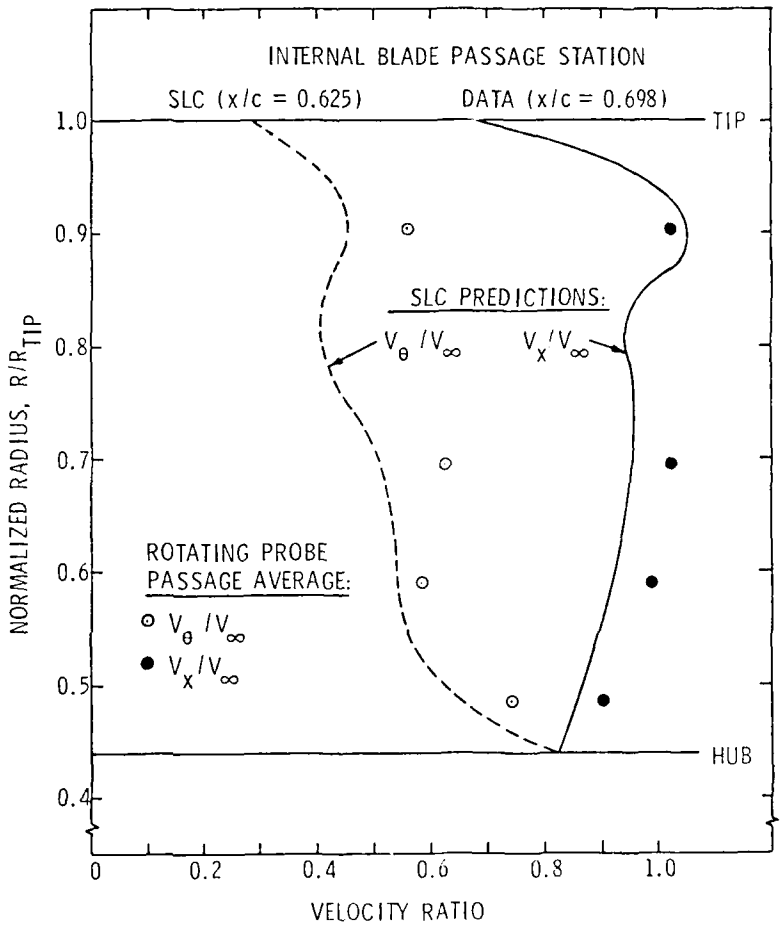

Figure 95. Comparison of Streamline Curvature (SLC) Prediction and Measured Flow Field Surve for Internal Blade Station No. 11

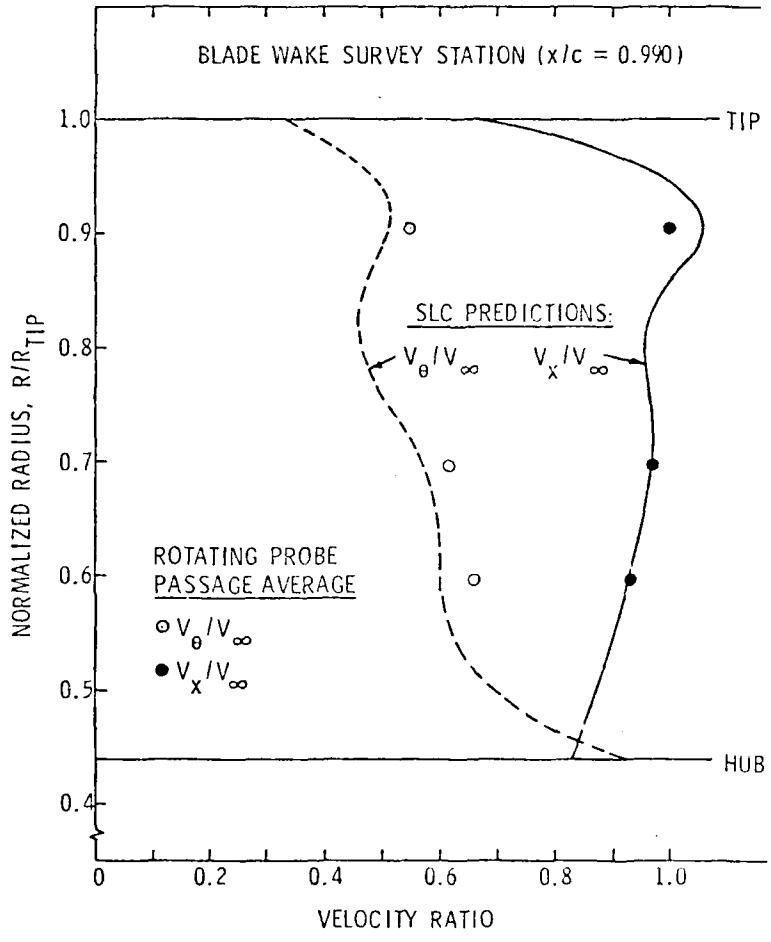

Figure 96. Comparison of Streamline Curvature (SI
Prediction and Measured Flow Field Su
for Wake Station No. 13

AD-A094 422 PENNSYLVANIA STATE UNIV UNIVERSITY PARK APPLIED RESE--ETC F/G 20/4
EXPERIMENTAL VERIFICATION OF THE STREAMLINE CURVATURE NUMERICAL--ETC(U)
MAY 80 M J PIERZGA N00024-79-C-6043
UNCLASSIFIED ARL/PSU/TM-80-181 NL

3 OF 3
AD A094422

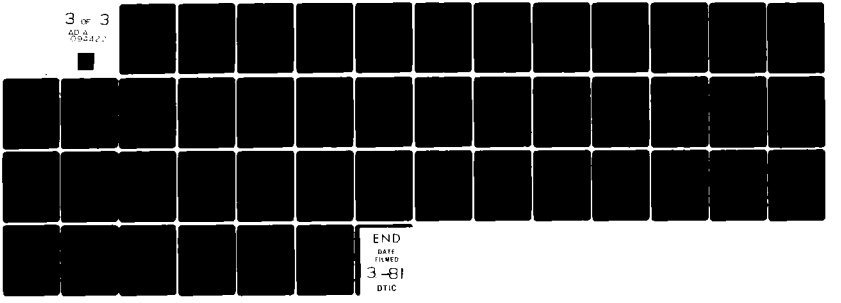

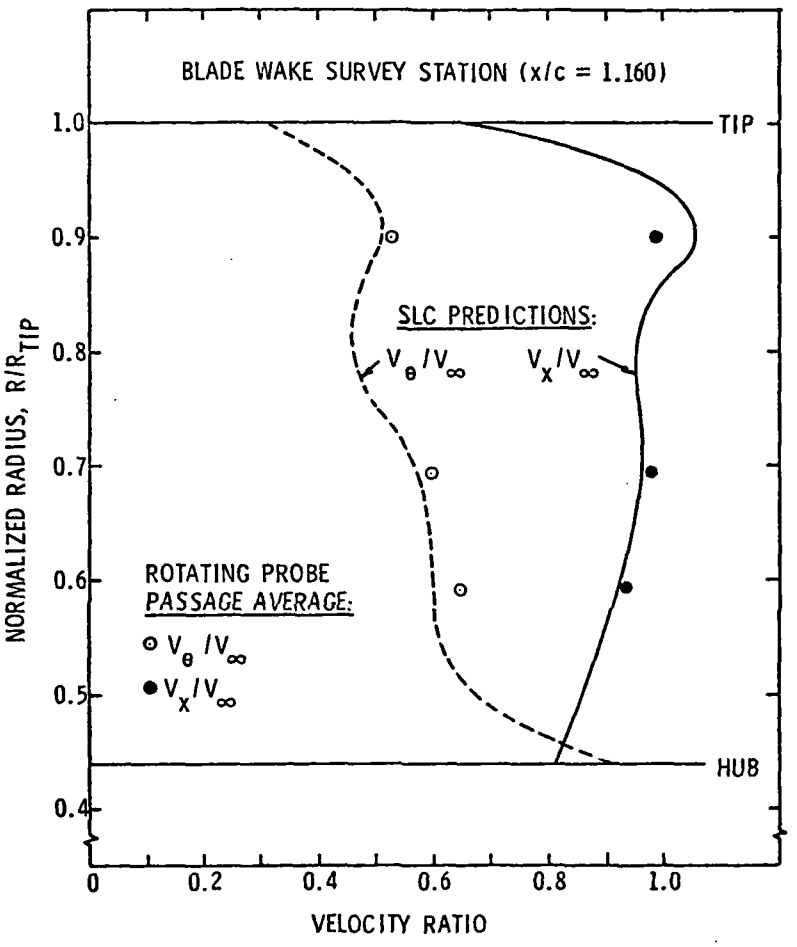

Figure 97. Comparison of Streamline Curvature (SLC) Prediction and Measured Flow Field Survey for Wake Station No. 14

Figures 93 through 95 represent the three stations inside the blade row at which experimental data have been collected. The first two stations represent the correct axial locations of the internal flow field surveys, while the third calculating station had to be moved upstream to avoid intersecting with the meridional projection of the rotor trailing-edge. Comparing the measured and predicted values for each of these stations, it is obvious that portions of a given profile may agree quite well while other portions do not. This trend indicates that the chordwise loading distribution must also vary in the radial direction as well. At the present time, there is no provision in the SLC analysis method to include radial variations of intra-blade loading. It must be pointed out, however, that the internal blade row calculations can only be as accurate as the outlet flow field predictions.

Figures 96 and 97 are comparison plots at the two downstream wake survey stations of the measured axial and tangential velocity profiles and the SLC predicted axial and tangential velocity profiles. The SLC velocity profiles shown in Figures 96 and 97 are very similar since the inviscid analysis possesses no mechanism to change the energy along a streamline in the blade-free regions of the flow. The measured profiles, on the other hand, are changing and moving closer to the predicted profiles. The measured profiles are decaying with axial distance from the rotor trailing-edge due to the viscous forces which are present in the real flow. This phenomenon was noted previously in Figures 85 and 86. This trend is very interesting and suggests that the accuracy of the analytic predictions depends somewhat on the axial position of the measuring station.

Figure 98 shows the measured and predicted values of the relative outlet flow angle as a function of radius for the AFRF test rotor. The relatively good agreement at the hub and mid-sections reflects the agreement shown previously in the velocity profiles. The deviation between measured flow angle and predicted values near the rotor tip indicates that this is a region in which the SLC technique could be improved. Overall, the agreement shown in Figure 98 indicates that the SLC analysis method can predict the outlet flow angles very well for this rotor.

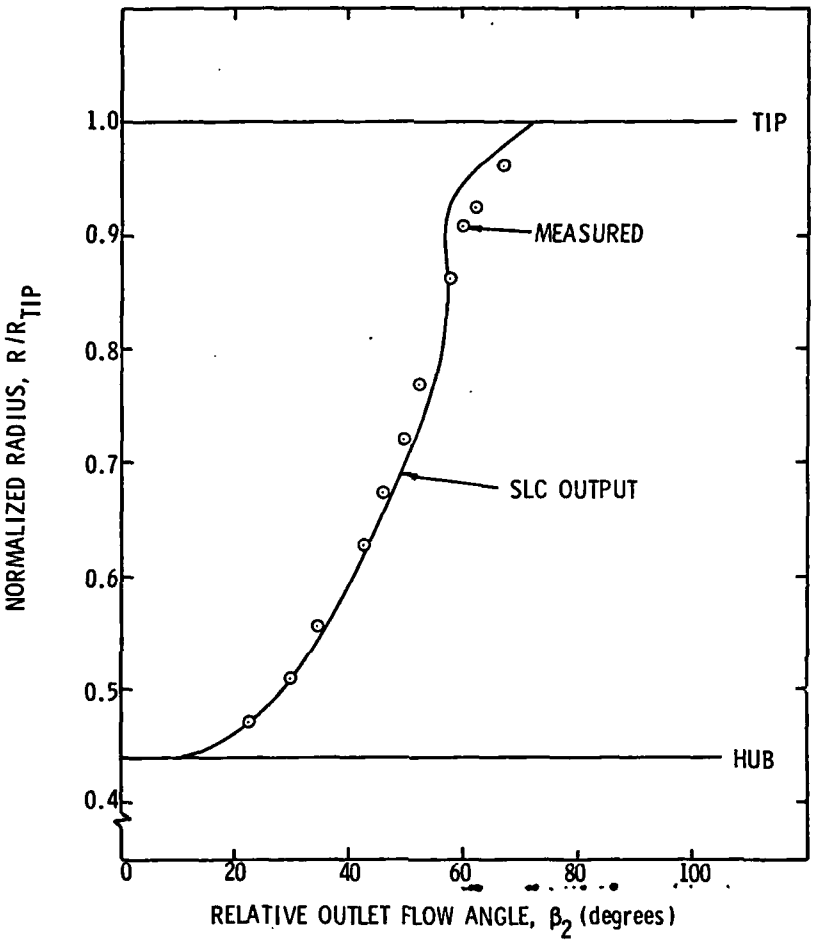

Figure 98. Comparison of Streamline Curvature (SLC) Prediction and Measured Relative Outlet Flow Angles

7. UNCERTAINTY OF DATA

As with any experimental investigation, great importance has been placed on the determination of the quality of the survey data. In this experimental study, every survey was checked for the precision of the measurement, as well as the repeatability of each data point within a survey. To improve the precision of the experimental data, four separate surveys, which may each consist of as many as 60 data points, were conducted at each measurement location. Each data point was then statistically analyzed to find the mean value of the four readings, as well as the 90 percent confidence level using Student's t-distribution [26] for small samples. After analyzing all of the data, the 90 percent confidence level calculations indicate that all of the data was within ±1 percent of the particular survey point's calculated mean value. It is this mean value which is assumed to be the true and accurate value used in the calculations. These mean values were then used in the data reduction procedure to yield the final velocity and pressure fields.

The repeatability of a particular survey was determined by a calculation similar to the one already described. In this case, however, the particular survey data points were compared to the average of the data points obtained to that point. If the new survey points were within ±1 percent of the mean values, then the new survey was accepted. If the new survey falls outside of this acceptable range, the data were retaken and, if necessary, a complete system check was performed.

8. CONCLUSIONS AND RECOMMENDATIONS FOR FUTURE RESEARCH

8.1 Conclusions

The purpose of this investigation has been to verify the accuracy of the streamline curvature (SLC) numerical analysis method using the AFRF free-vortex, cambered test rotor. To obtain detailed flow field measurements with which SLC predictions can be compared, a circumferential traversing mechanism capable of conducting internal blade row flow field surveys was designed and built. Since the complete verification of an analysis method requires more time than is possible in this study, the flow field measurements and code verification are restricted to operation at the design point of the test rotor.

The results presented in this investigation clearly indicate that the inviscid, incompressible streamline curvature method is capable of accurately predicting the overall design performance of the AFRF blade row. This statement of accuracy is, of course, limited to the test case which has been investigated and any extension of the analysis method to other rotor configurations and flow conditions can only be surmised. However, if other rotor configurations and flow conditions are compatible with the empirical loss model correlations used in this study, one could expect to observe results very similar to those presented.

In addition to investigating the ability of the streamline curvature method to predict the inlet and exit flow conditions of the AFRF test rotor, investigations to determine its ability to calculate the correct internal blade row flow were also conducted. Prior to this investigation, attempts at computing the internal flow field

required some estimation of the fluid turning through the blade row. This estimation may take many forms ranging from simple linear approximations from the leading- to the trailing-edges of the blade, to more complex schemes that follow some mean line path. The limiting factor in such an approach is that these somewhat arbitrary distributions possess little or no experimental data base.

In order to compare the numerical prediction with the experimental results of this complex internal flow region, it is necessary to obtain some reasonable estimation of the turning distribution through the test rotor. Since there is no way to calculate this turning distribution and there exist no empirical correlations that can be used, the only alternative is to use the experimental data. The results that have been obtained using this approach reveal that the streamline curvature method could, with some minor code modifications, predict the internal flow field to within an acceptable degree of accuracy. This assumption, however, is conditional on future work to obtain reliable empirical correlations for the actual distribution of turning through a rotating blade row.

The ability of the Douglas-Neumann cascade source code to correctly predict the inviscid pressure distributions on the blade surfaces has been demonstrated. These distributions are very important in the prediction of separation, blade forces, and mechanical and aerodynamic stresses for a particular hardware configuration. All these factors play a major role in the overall feasibility evaluation of a particular design and thus should be as accurate as possible.

The potential use of the SLC method in predicting the flow field on the blade-to-blade stream surface has also been demonstrated.

Although the procedure has not proved useful in its present state, the results obtained in this investigation indicate that only minor adjustments may be necessary to produce a usable code. The usefulness of a numerical method which can compute both the hub-to-tip turbomachinery solution, as well as the blade-to-blade solution, to within the accuracy range demonstrated by this investigation is indeed a valuable tool to the turbomachinery design engineer.

8.2. Recommendations for Future Research

This investigation has provided only the preliminary groundwork necessary for the complete SLC verification procedure. The experimental hardware has been developed which can be used to obtain detailed flow field information for any rotor operating in the AFRF facility. To completely verify the streamline curvature analysis technique, further work is needed in the area of off-design performance predictions. These additional investigations are straightforward extensions of the work started in this study in which one could devote more time to the verification process and less time to hardware development.

One of the areas in which future investigations would be beneficial is in the collection of data within the blade row. At the present time, only three radial positions of survey probes are possible. Future work should increase the radial density of survey points so that more resolution of the profiles is obtained. This would more accurately define the radial distributions of velocity through the blade row and would more clearly map regions of flow separations and tip leakage flows. Along with the more detailed flow field surveys inside the blade row, the SLC blade-to-blade analysis is also worth further study.

With more detailed flow information, the blade-to-blade analysis of the flow field is increasingly important to the overall analysis.

Further work is also needed in the calculation of deviation angle at the tip. The tip leakage flow correction is a weak link in the present analysis and should be studied in more detail. Perhaps a different model might be used for the effects of this secondary flow phenomenon.

REFERENCES

1. Horlock, J. H., Actuator Disk Theory--Discontinuities in Thermo-Fluid Dynamics, McGraw-Hill International Book Company, 1978.

2. Wu, C. H., "A General Theory of Three-Dimensional Flow in Subsonic and Supersonic Turbomachines of Axial, Radial, and Mixed-Flow Types," NACA TN-2604, 1952.

3. Marsh, H., "A Digital Computer Program for the Through-Flow Fluid Mechanics in an Arbitrary Turbomachine Using a Matrix Method," Aero. Res. Council, R&M 3509, 1968.

4. Smith, D. J. S. and Frost, D. H., "Calculation of the Flow Past Turbomachine Blades," Proceedings of the Institute of Mechanical Engineers, Vol. 184, Paper 27, 1970.

5. Davis, W. R., "A General Finite-Difference Technique for the Compressible Flow in the Meridional Plane of Centrifugal Turbomachinery," ASME Paper 75-GT-121, Gas Turbine Conference and Products Show, Houston, Texas, March 2-6, 1975.

6. Novak, R. A., "Streamline Curvature Computing Procedures for Fluid-Flow Problems," ASME Paper 66-WA/GT-3, 1966, Winter Annual Meeting, New York, New York, November 27 - December 1, 1966.

7. Smith, L. H., "The Radial Equilibrium Equation of Turbomachinery," Trans. ASME, Series A, Vol. 88, 1966.

8. Silvester, M. E. and Hetherington, R., "Three-Dimensional Compressible Flow Through Axial Flow Turbomachines," Numerical Analysis--An Introduction, Academic Press, 1966.

9. Davis, W. R. and Millar, D. A. J., "A Comparison of the Matrix and Streamline Curvature Methods of Axial Flow Turbomachinery Analysis, From a User's Point of View," ASME Paper 74-WA/GT-4, 1974, Winter Annual Meeting, New York, New York, November 17-22, 1974.

10. Marsh, H., "Through-Flow Calculations in Turbomachinery: A Technical Point of View," AGARD CP-195, 1976.

11. McBride, M. W., "A Streamline Curvature Method of Analyzing Axisymmetric Axial, Mixed, and Radial Flow Turbomachinery," Applied Research Laboratory, Technical Memorandum, File No. 77-219, July 21, 1977.

12. Giesing, J. P., "Extension of the Douglas-Neumann Program to Problems of Lifting, Infinite Cascades," U.S. Department of Commerce Report No. LB 31653, 1964.

13. Horlock, J. H., "Two-Dimensional Cascades: Experimental Work," Axial Flow Compressors, Robert E. Krieger, New York, 1973, pp. 55-60.

14. Constant, H., "Performance of Cascades of Aerofoils," R.A.E. Note No. E 3696; ARC Rep. No. 4155, 1939.

15. Lakshminarayana, B., A Discussion of Wilson, Mani, and Acosta's "A Note on the Influence of Axial Velocity Ratios on Cascade Performance," NASA SP-304, Part I, 1974, pp. 127-133.

16. Scholz, N., Aerodynamik der Schaufelgitler, Band I, Verlag G. Braun, p. 165.

17. Lieblein, S., "Experimental Flow in Two-Dimensional Cascades," NASA SP-36, 1965, pp. 209-222.

18. Billet, M. L., "Secondary Flow Related Vortex Cavitation," Ph.D. Thesis, The Pennsylvania State University, Department of Aerospace Engineering, 1978.

19. Lakshminarayana, B., "Methods of Predicting the Tip Clearance Effects in Axial Flow Turbomachinery," Journal of Basic Engineering, Vol. 92, Series D, No. 3, September 1979, pp. 467-482.

20. Gliebe, P. R., "Coupled Inviscid/Boundary Layer Flow Field Predictions for Transonic Turbomachinery Cascades," Transonic Flow Problems in Turbomachinery, Hemisphere Publishing Corp., 1977.

21. Bruce, E. P., "The ARL Axial Flow Research Fan--A New Facility for the Investigation of Time-Dependent Turbomachinery Flows," Presented at Combined Canadian Soc. for M.E. and ASME FED Conference, Quebec, Canada, May 1974, ASME Paper No. 74-FE-27.

22. Yocum, A. M., "The Effects of Design and Operating Variables on the Response of an Axial Flow Fan to Inlet Flow Distortions," M.S. Thesis, The Pennsylvania State University, Department of Mechanical Engineering, 1978.

23. Milne, W. E., Numerical Calculus--Approximations, Interpolations, Finite Differences, Numerical Integration, and Curve Fitting, Princeton University Press, 1949, pp. 242-290.

24. Hirsch, C. H. and Kool, P., "Measurement of the Three-Dimensional Flow Field Behind an Axial Compressor Stage," ASME Paper No. 76-GT-18, Gas Turbine Conference and Products Show, New Orleans, La., March 21-26, 1976.

25. Raj, R. and Lakshminarayana, B., "Three Dimensional Characteristics of Turbulent Wakes Behind Rotors of Axial Flow Turbomachinery," ASME Paper No. 75-GT-1, Gas Turbine Conference and Products Show, Houston, Texas, March 2-6, 1975.

26. Walker, H. M. and Lev, J., Elementary Statistical Methods, Holt, Rinehart, and Winston, New York, N.Y., 1958, pp. 202-225.

27. Treaster, A. L. and Yocum, A. M., "The Calibration and Application of Five-Hole Probes," Applied Research Laboratory, Technical Memorandum File No. 78-10, January 18, 1978.

APPENDIX A

DERIVATION OF HOWELL'S DEVIATION EQUATION

Given the following relationships from Reference [12], the derivation of Equation (13) is shown.

$$\delta^* = m\theta_c (S/C)^{1/2} \tag{A1}$$

$$m = 0.23 (2a/c)^2 + \frac{0.1}{50} \alpha_2^* \tag{A2}$$

$$\alpha_2^* = \alpha_2 + m\theta_c (S/C)^{1/2} \tag{A3}$$

When Equation (A1) is rearranged

$$m = \frac{\delta^*}{\theta_c (S/C)^{1/2}} \quad . \tag{A4}$$

Substituting Equation (A4) into Equation (A2) yields

$$\frac{\delta^*}{\theta_c (S/C)^{1/2}} = 0.23 (2a/c)^2 + \frac{0.1}{50} \alpha_2^* \quad . \tag{A5}$$

Substituting Equation (A3) into Equation (A5) yields

$$\frac{\delta^*}{\theta_c (S/C)^{1/2}} = 0.23 (2a/c)^2 + \frac{0.1}{50} (\alpha_2 + m\theta_c (S/C)^{1/2}) \quad . \tag{A6}$$

When Equation (A6) is rearranged

$$\frac{\delta^*}{\theta_c (S/C)^{1/2}} - \frac{0.1}{50} \alpha_2 - \frac{0.1}{50} m\theta_c (S/C)^{1/2} = 0.23 (2a/c)^2 \tag{A7}$$

or

$$\delta^* - \frac{0.1}{50} \theta_c (S/C)^{1/2} \alpha_2 - \frac{0.1}{50} \theta_c (S/C)^{1/2} \delta^* = 0.23 \theta_c (S/C)^{1/2} (2a/c)^2, \tag{A8}$$

thus,

$$-\frac{0.1}{50}\theta_c\,(S/C)^{1/2}\,\alpha_2 + \delta^*\left[1 - \frac{0.1}{50}\,\theta_c\,(S/C)^{1/2}\right] = 0.23\,\theta_c\,(S/C)^{1/2}(2a/c)^2\,. \tag{A9}$$

When α_2 is added to both sides of Equation (A9),

$$\alpha_2 - \frac{0.1}{50}\,\theta_c\,(S/C)^{1/2}\,\alpha_2 + \delta^*\left[1 - \frac{0.1}{50}\,\theta_c\,(S/C)^{1/2}\right] =$$

$$\alpha_2 + 0.23\,\theta_c\,(S/C)^{1/2}\,(2a/c)^2 \tag{A10}$$

or

$$\alpha_2\left[1 - \frac{0.1}{50}\,\theta_c\,(S/C)^{1/2}\right] + \delta^*\left[1 - \frac{0.1}{50}\,\theta_c\,(S/C)^{1/2}\right] =$$

$$\alpha_2 + 0.23\,\theta_c\,(S/C)^{1/2}\,(2a/c)^2\,. \tag{A11}$$

When Equation (A11) is simplified,

$$\alpha_2 + \delta^* = \frac{\alpha_2 + 0.23\,\theta_c\,(S/C)^{1/2}\,(2a/c)^2}{1 - \frac{0.1}{50}\,\theta_c\,(S/C)^{1/2}} \tag{A12}$$

or, finally,

$$\delta^* = \frac{\alpha_2 + 0.23\;\theta_c\,(S/C)^{1/2}\,(2a/c)^2}{1 - \frac{0.1}{50}\,\theta_c\,(S/C)^{1/2}} - \alpha_2 \tag{A13}$$

where $\delta^* = \delta_H$ in Equation (A13).

APPENDIX B

AXIAL FLOW RESEARCH FAN (AFRF) TEST ROTOR PERFORMANCE EVALUATION

Introduction

The results of a test program to determine the performance characteristics of the Axial Flow Research Fan (AFRF) Nine-Bladed Cambered Rotor are presented. The test program consisted of conducting radial flow surveys upstream and downstream of the rotor for several different mass flows. Flow configurations included the design mass flow and values greater and less than design. In addition to the performance data, flow measurements were made at the blade mean radius at various axial positions upstream and downstream of the rotor at the design mass flow. A detailed description of the AFRF can be found in Reference [21].

Instrumentation

Radial flow surveys were obtained using two standard prism-type five-hole pressure probes. These probes were used in the non-nulling mode as described by Treaster and Yocum [27]. Both probes were previously calibrated for flow angles of ±30 degrees in both the yaw and pitch planes [22]. These probes were also calibrated for the effects of Reynolds number and wall interference. All data were reduced using standard data reduction programs which included the corrections due to wall proximity and variations in probe Reynolds number.

A schematic of the AFRF is shown in Figures B1 and B2. Both probes were positioned approximately 30 degrees from the vertical as indicated in Figure B1. These positions were necessary to avoid any interaction with the wakes of the three support vanes located near the inlet of

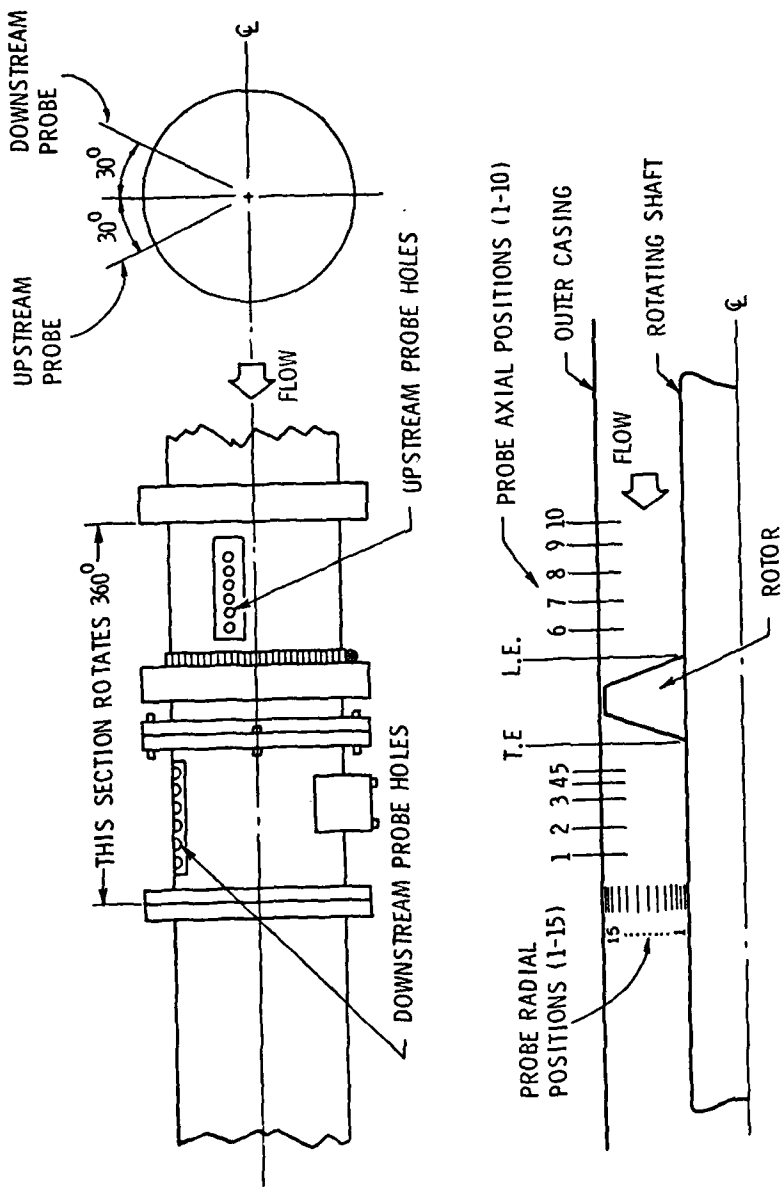

Figure B1. Schematic of Probe Positions and Test Facility

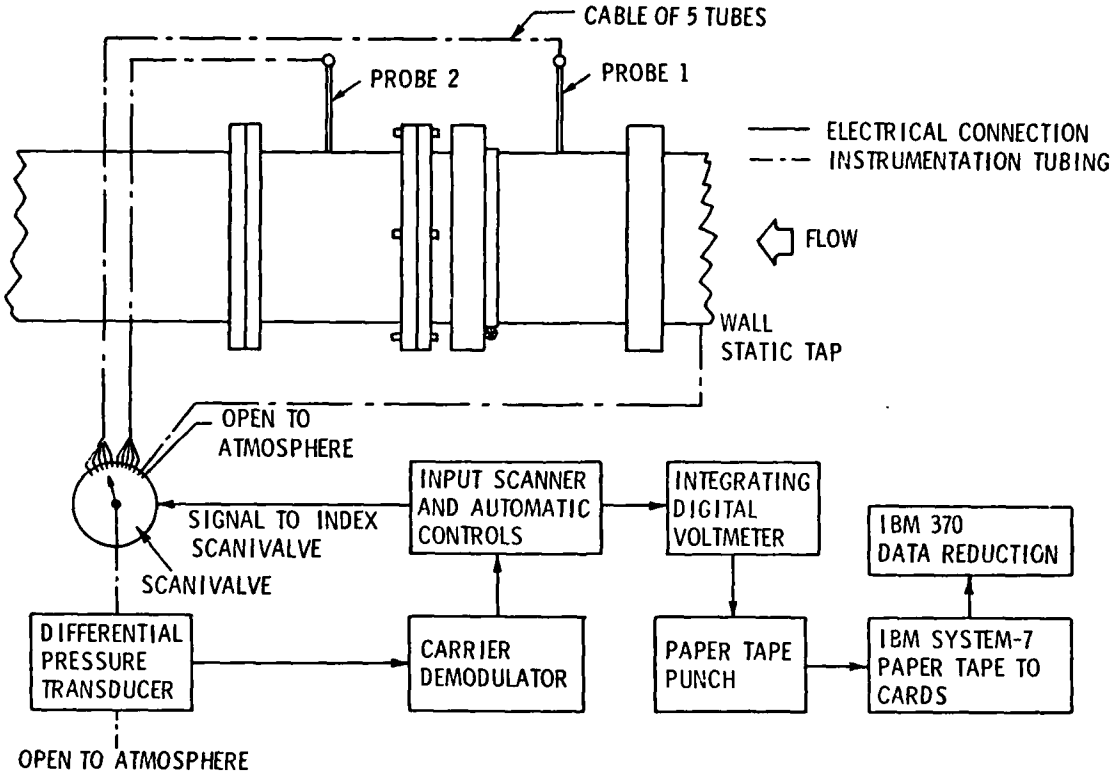

Figure B2. Schematic of Test Instrumentation

the AFRF. Figure B1 also shows the 10 axial positions and 15 radial positions used in the test. Tables B1 and B2 provide the dimensions for all these measurement stations.

The use of two probes made it possible to obtain the upstream and downstream data simultaneously. This reduced any error which might have occurred due to changes in the run conditions. The use of the same radial position for both probes simplified the data reduction procedure; thus, identical radial positions were used throughout the program.

As the schematic in Figure B2 indicates, the pressure tubes from the two five-hole probes were connected to a scanivalve which was used to index the individual pressure signals. These pressures were transmitted to a ±1.0 psi Validyne Model DP15 differential pressure transducer in which the reference port was open to atmospheric pressure. The electrical signal from the transducer was transmitted to a data acquisition unit which included an integrating digital voltmeter and a paper tape punch. All ten pressures from the two probes were measured and recorded on paper tape in the form of voltages. In addition, readings from an upstream static pressure wall tap and a reference atmospheric tap were recorded. The atmospheric tap reading allowed for the zero shift of the transducer power supply to be measured and subtracted from the other readings. The wall tap was calibrated using a pitot-static tube positioned at the mid-channel radius so that a given output voltage from the wall tap corresponded to a particular free-stream velocity (V_∞). In the reduction of the data, the free-stream velocity was calculated from this static pressure reading and was used to non-dimensionalize the velocity components.

Table B1. Axial Distance to Rotor Leading Edge for Each Axial Probe Position

Probe Position No.	Axial Distance to Rotor Leading Edge
1	39.88 cm (15.70 in)
2	34.80 cm (13.70 in)
3	29.72 cm (11.70 in)
4	25.91 cm (10.20 in)
5	23.37 cm (9.20 in)
6	5.84 cm (2.30 in)
7	8.38 cm (3.30 in)
8	10.92 cm (4.30 in)
9	16.00 cm (6.30 in)
10	19.81 cm (7.80 in)

Table B2. Radial Distance from Rotor Hub for Each Radial Probe Position

Probe Position No.	Radial Distance from Rotor Hub
1	0.762 cm (0.30 in)
2	1.270 cm (0.50 in)
3	1.778 cm (0.70 in)
4	2.286 cm (0.90 in)
5	3.048 cm (1.20 in)
6	5.080 cm (2.00 in)
7	6.350 cm (2.50 in)
8	7.620 cm (3.00 in)
9	8.890 cm (3.50 in)
10	11.430 cm (4.50 in)
11	12.700 cm (5.00 in)
12	13.208 cm (5.20 in)
13	13.716 cm (5.40 in)
14	14.224 cm (5.60 in)
15	14.665 cm (5.75 in)

The Test Rotor

The AFRF Nine-Bladed Cambered Rotor was designed using procedures outlined by Lieblein [16]. The rotor consists of nine circular-arc camberline blades with a maximum thickness-to-chord ratio of 10 percent. The blades were designed with a free vortex radial loading distribution. The loading level as described by Bruce [21] is

$$RV_\theta = 2.32 \text{ m /sec } (25.0 \text{ ft /sec}) \quad , \tag{B1}$$

where

$$V_\infty = 24.28 \text{ m/sec } (80.0 \text{ ft/sec}) \quad . \tag{B2}$$

In the design of the rotor, a uniform inlet velocity profile was assumed and the design variables for each of the seven cylindrical sections were calculated using the equations and empirical data from Lieblein [16]. The calculated design parameters are given in Table B3.

Test Procedures and Results

Since the actual flow field through the cambered rotor was not entirely known beforehand, it was necessary to make some preliminary surveys to become familiar with the magnitudes of the flow angles and velocities which might be encountered. These preliminary surveys were conducted at five different axial positions upstream and downstream of the rotor. At a through-flow velocity of 19.81 m/sec (65.0 ft/sec) and a rotational speed of 1604 RPM, five radial velocity surveys were conducted with both probes aligned in the axial direction. These flow conditions represented the design flow coefficient defined as

$$\phi = \frac{V_\infty}{U_m} \quad , \tag{B3}$$

Table B3. Design Data for Nine-Bladed Cambered Test Rotor

R	β_1	β_2	$\Delta\beta$	σ	$(i_0)_{10}-(\delta_0^0)_{10}$	1-m+n	$\bar{K}t \cdot Ksh \cdot [(i_0)_{10}-(\delta_0^0)_{10}]$	ϕ	m
(cm)	(deg.)	(deg.)	(deg.)	(c/s)	Fig. 178 (deg.)	Fig. 179-b	(deg.)	(deg.)	Fig. 168
12.065	45.66	13.21	32.45	1.81	4.97	0.757	5.467	35.64	0.176
13.589	49.06	24.35	24.71	1.61	4.52	0.702	4.972	28.12	0.200
16.637	54.68	40.01	14.67	1.31	3.75	0.590	4.125	17.87	0.248
19.685	57.08	47.87	9.21	1.11	3.12	0.492	3.432	11.74	0.291
22.733	62.59	58.48	6.11	0.96	2.64	0.400	2.904	8.01	0.330
25.781	65.43	61.18	4.24	0.85	2.21	0.317	2.431	5.71	0.365
27.305	66.65	63.06	3.59	0.80	2.03	0.282	2.233	4.80	0.380

R	δ_0^0	δ^0	$(\delta_0^0)_{10}$	$(i_0)_{10}$	i_0	n	i	λ(or γ°)	V_θ/V_∞	α_2
	Eq.(271)	Eq.(268)	Fig. 161	Fig. 137	Eq.(262)	Fig. 138	Eq.(261)	(Eq.272)		$\tan^{-1}(V_\theta/V_\infty)$
(cm)	(deg.)	(deg.)	(deg.)	(deg.)	(deg.)		(deg.)	(deg.)		(deg.)
12.065	1.67	7.94	1.52	6.51	7.16	-0.069	4.70	23.14	0.789	38.26
13.589	1.83	7.45	1.66	6.20	6.82	-0.101	3.98	31.02	0.700	34.99
16.637	2.02	6.46	1.84	5.62	6.18	-0.161	3.30	42.44	0.572	29.76
19.685	2.08	5.48	1.89	5.00	5.50	-0.218	2.94	50.28	0.483	25.80
22.733	2.07	4.71	1.88	4.52	4.97	-0.271	2.80	55.78	0.418	22.71
25.781	2.06	4.14	1.87	4.11	4.52	-0.315	2.72	59.85	0.367	20.26
27.305	2.05	3.87	1.86	3.90	4.29	-0.340	2.66	61.59	0.348	19.21

Kt = 1.0
Ksh = 1.1
V_∞ = 37.556 m/sec
$V_{\theta inlet}^\infty$ = 0.0

V_x/V_∞ = 1.0
R_{tip} = 27.305 cm
R_{hub} = 12.065 cm
Chord = 15.240 cm

For figures and equations see Reference [16].

where V_∞ is the axial through-flow velocity, and U_m is the rotor rotational velocity at the mean radius.

For each radial position, the five-hole probe yields the total and static pressure plus the three components of total velocity in the axial and radial directions. Positive values of the tangential and radial velocity components indicate flow in the direction of rotation in the absolute reference frame and outward toward the casing, respectively.

The preliminary test surveys indicated very large absolute flow angles in the region downstream of the rotor. These flow angles were well outside the probe calibration range when the probe was aligned in the axial direction. Thus, the downstream probe was rotated 20 degrees in the yaw plane so that it was more closely aligned with the oncoming absolute velocity vector. This procedure enabled the existing calibration data to be used.

Another problem which presented itself during these preliminary tests was the apparent existence of radial flow near the rotor tip. A plot of the radial component of velocity is shown in Figure B3. This figure shows that the inlet profile exhibits small radial velocities until a distance is reached of approximately one inch from the outer casing. From continuity considerations, it is assumed that there can be no flow normal to the casing wall. By physically plugging the spaces around the probes, it was further assumed that there was no flow out through the casing wall. Since the highly three-dimensional downstream flow field is not well defined with its tip leakage flows, vortex development, and wake structures, it is not possible to deal directly with the downstream profile. However, the upstream flow should not

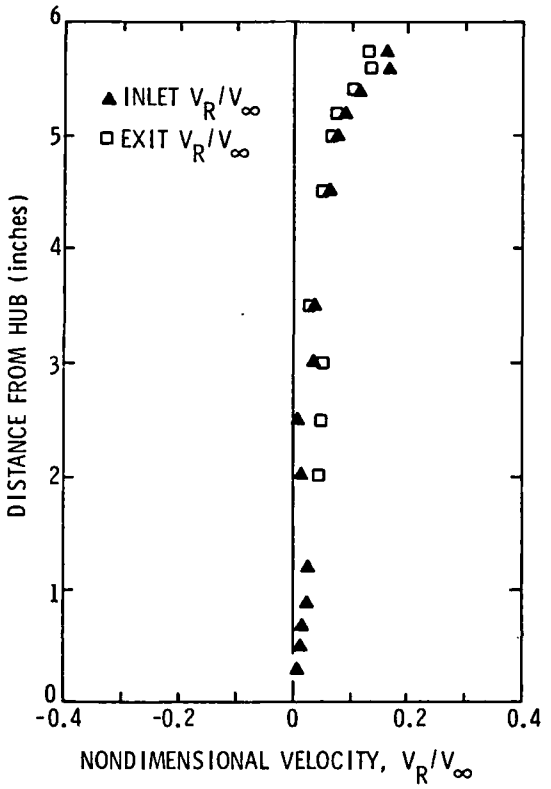

Figure B3. Radial Velocity Profile Uncorrected for Shear

exhibit this radial flow phenomenon in the tip region. Thus, it may be possible to correct for this radial flow in the upstream profile and then apply the same correction to the flow downstream of the rotor.

The five-hole probes that were used in these surveys were calibrated for the effects of wall proximity and Reynolds number, but not for the effects of a shear layer. The problem becomes one of a difference in velocity and, thus, pressure being sensed by the probe's two pitch-plane holes. These holes, numbered 4 and 5, are shown in Figure B4. To reduce the data collected from the five-hole probe, a static pressure is calculated from an arithmetic mean of the two yaw holes (holes 2 and 3) and the two pitch holes (holes 4 and 5). The wall correction routine corrects this static pressure reading based on calibration data, but it does not correct the calculation of a pitch angle due to the shear layer. This pitch angle is based on the difference between the readings of the pitch holes. It is the lack of such a correction which was thought to be the cause of the indicated radial flows.

Since the yaw holes are at the same radial location as the total pressure hole (hole 1 in Figure B4), there is no need for a correction in the yaw plane. The pitch holes, however, are located at 0.0762 cm (0.03 inch) above and below the total pressure hole. The boundary layer at the wall causes the hole closest to the wall to see a lower velocity than the hole further away from the wall and thereby indicating a pressure difference and a radial flow. To correct for the shear layer, the voltage from each pitch hole is plotted against the actual radial distance to that respective pitch-plane hole for an entire radial traverse. These plots are then used to obtain an interpolated

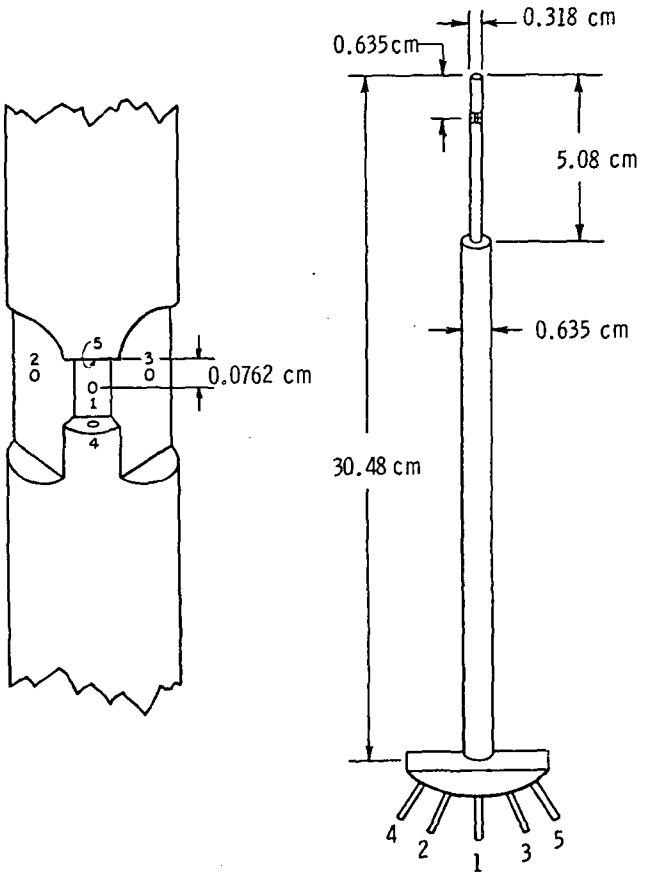

Figure B4. Five-Hole Prism Probe - United Sensor Type DA-125-12-F-10-CD

value of voltage for each pitch hole at the radial position of the total pressure and yaw holes. In this manner, all five values of pressure are obtained at the same radial position. These new voltages are then used in the reduction programs.

This procedure was used on the survey shown in Figure B3 and the results of the shear layer correction method applied to both the upstream and downstream profiles are shown in Figure B5. Figure B5 shows a definite decrease in radial flows at the rotor tip for the inlet profile. The corrected inlet p file in Figure 5 indicates that while the radial velocity does go to zero at the wall, there still seems to be a rather large radial flow in that region. At this point continuity has been satisfied in that there is no real flow normal to the casing wall. A subsequent study has revealed that the small aluminum plugs used to cover the unused upstream probe access holes were protruding below the surface of the casing wall. With these plugs removed and the holes covered with adhesive tape, the inlet radial velocity component assumed its expected insignificant role in the upstream profile. The downstream profile was unchanged in this case, probably due to the large amounts of mixing and turning which the flow experiences upon passing through the rotor.

With the information obtained from the preliminary investigation, a single axial location upstream and downstream of the rotor was selected to make the performance measurements. Axial positions from the rotor leading-edge of 0.717 c and 1.617 c were chosen for the respective upstream and downstream stations. It was desirable to have the downstream station at least one-half a chord length downstream of the trailing-edge so that the wake structure would have time to develop.

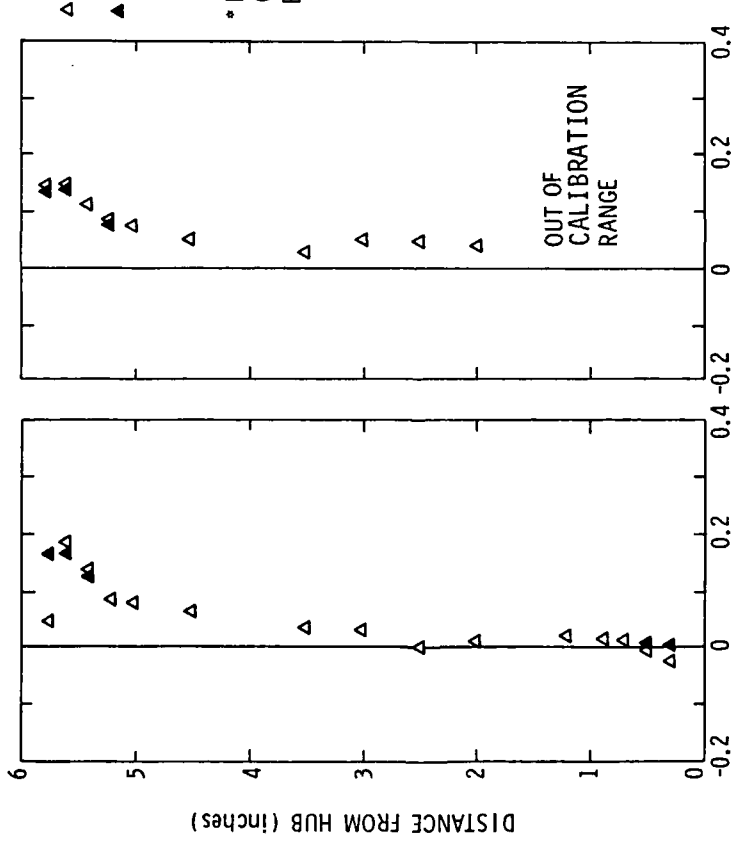

Figure B5. Effects of Shear Layer Correction on Radial Velocity

The plots of measured inlet and exit velocity profiles are shown in Figures B6 through B12. Each plot represents a different mass flowrate condition. Flow conditions representing a flow coefficient that was 10 percent below the design value of a flow coefficient that was 75 percent above the design value were used.

From each velocity survey, a mass-averaged pressure rise coefficient (ψ) was calculated. Figure B13 represents the performance characteristic of this rotor in a ϕ versus ψ plot. The large uncertainty in the first point on the plot is due to stall which occurred and produced large separated regions in which the ±30 degree calibration range of the five-hole probes was exceeded. At best, this point represents an average of those points which were able to be recorded. The placement of the rotor design point indicates that the measured pressure rise is very close to the design pressure rise for the design mass flowrate.

In addition to the performance data, the measured incidence angles are compared to the design incidence angles in Figure B13. It can be seen that large differences occur near the hub and tip regions. These differences are caused by the existence of a boundary layer on both surfaces. Since small variations in the velocity vector can cause large variations in incidence angle, the differences become smaller as the points approach mid-channel. It can be seen that even though the design incidence angles are quite different from the measured angles near the two surfaces, the design pressure rise was still observed (Figure B13).

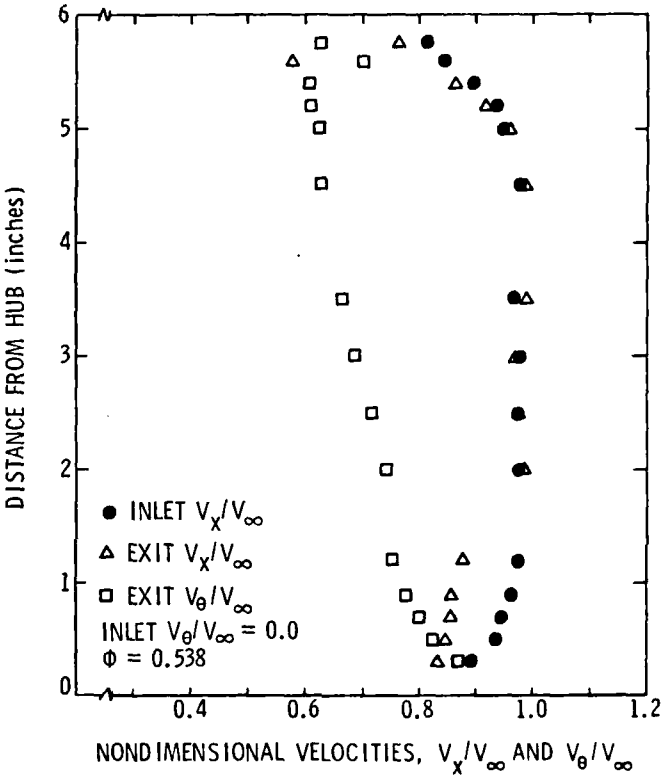

Figure B6. Velocity Profiles (10% low ϕ)

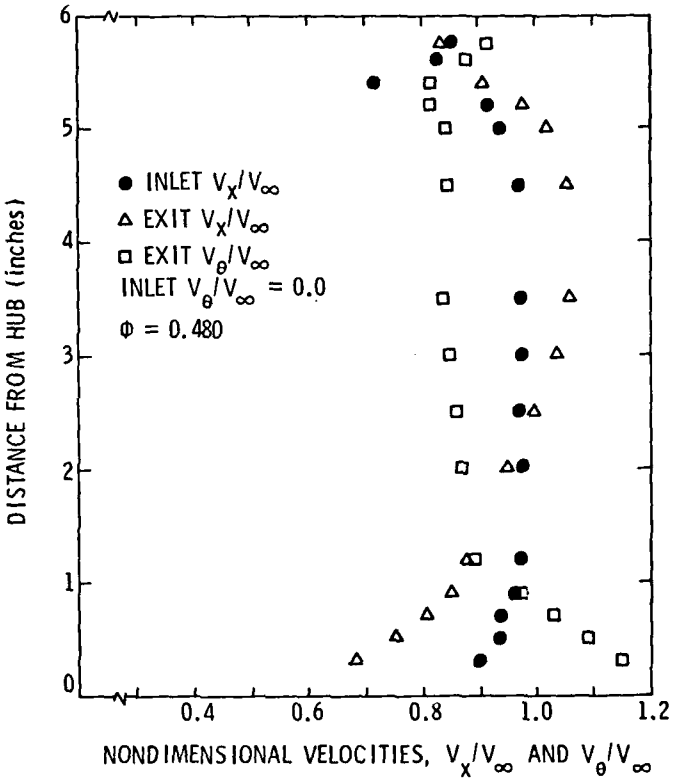

Figure B7. Velocity Profiles (20% low ϕ)

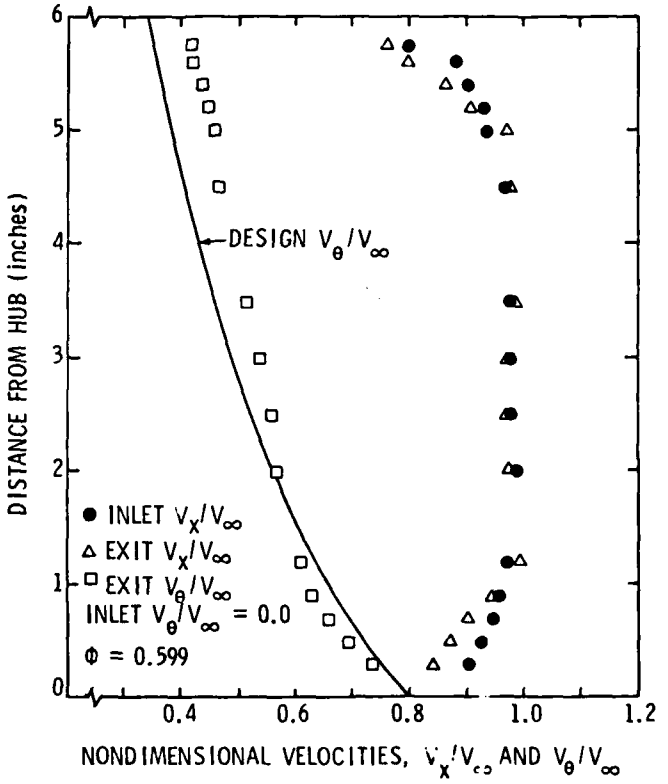

Figure B8. Velocity Profiles (Design ϕ)

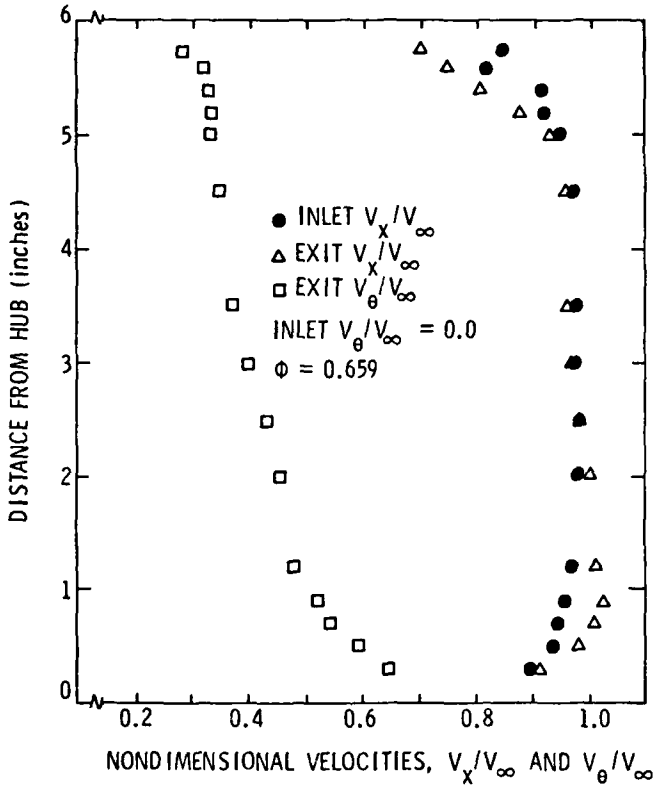

Figure B9. Velocity Profiles (10% high ϕ)

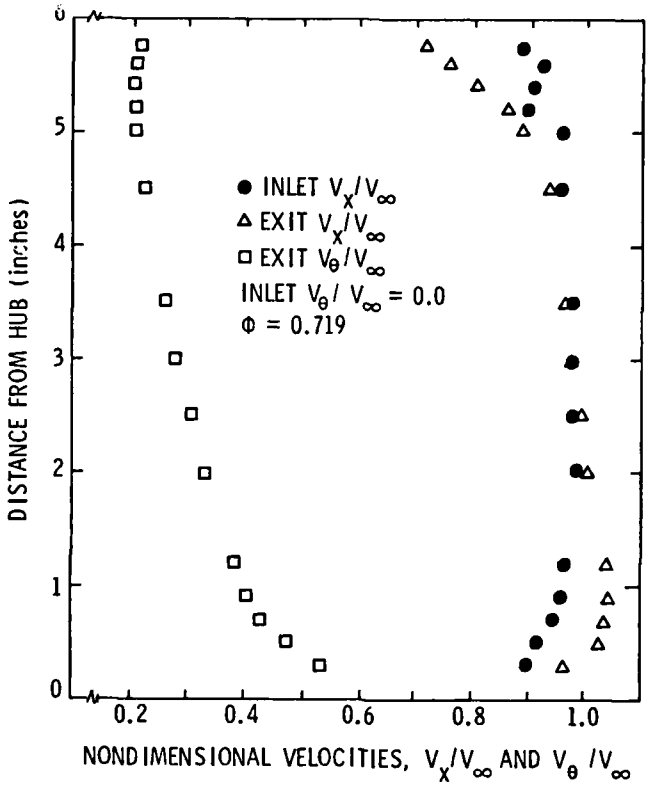

Figure B10. Velocity Profiles (20% high ϕ)

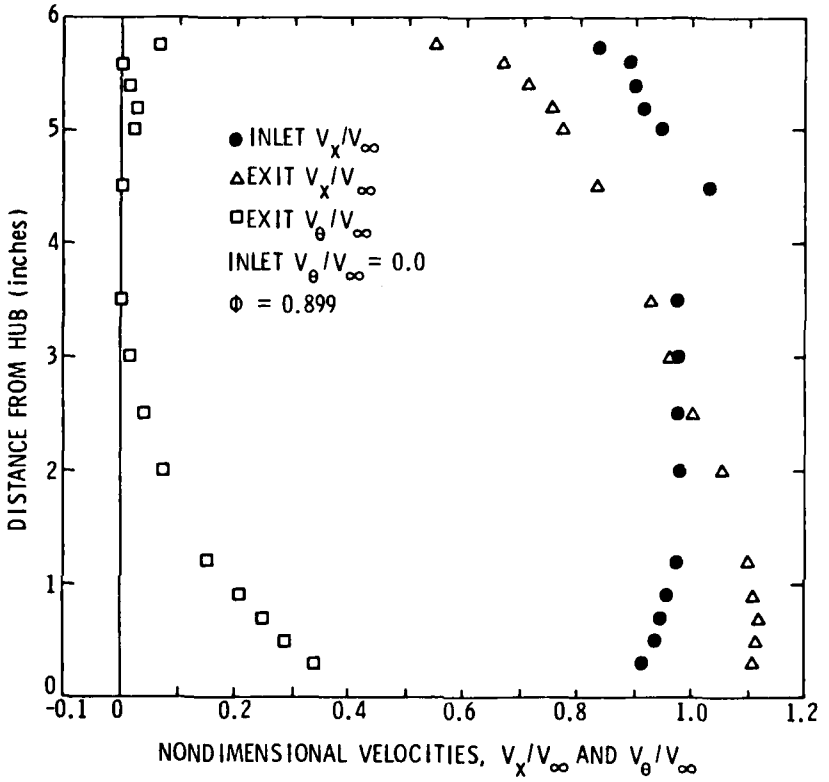

Figure B11. Velocity Profiles (50% high ϕ)

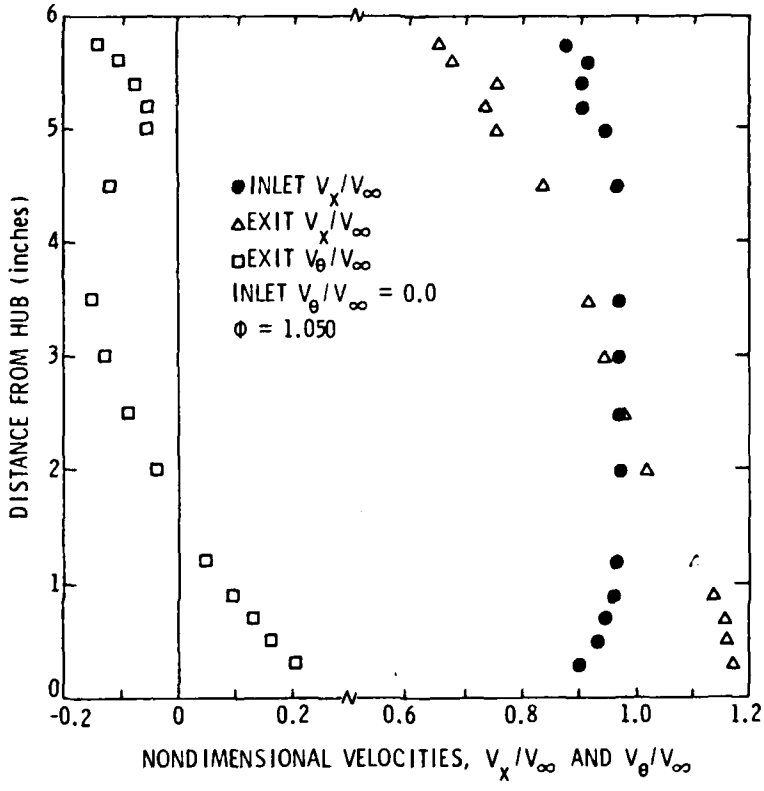

Figure B12. Velocity Profiles (75% high ϕ)

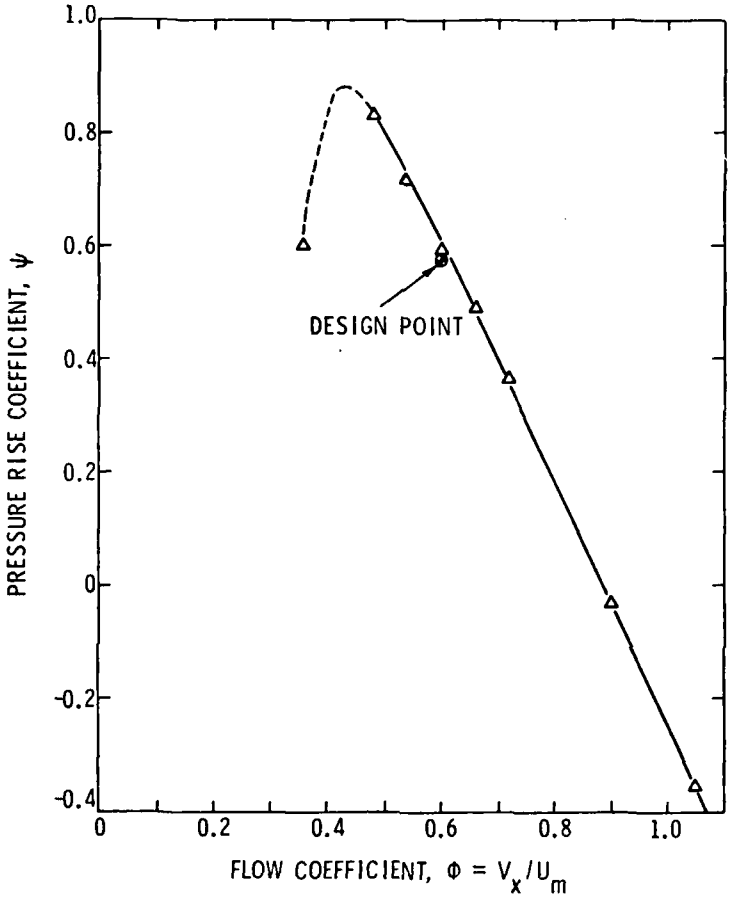

Figure B13. Performance Characteristic of AFRF Nine-Bladed Cambered Rotor

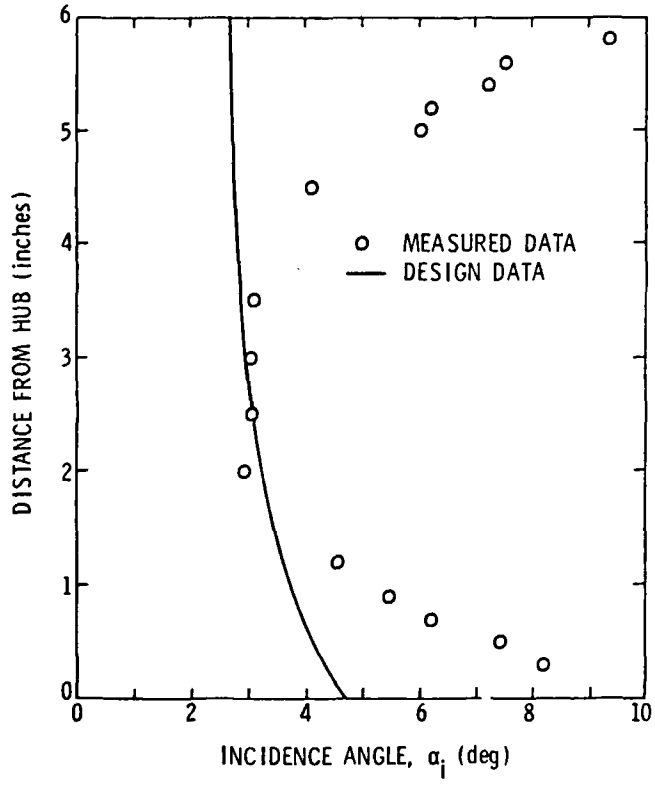

Figure B14. Comparison of Measured and Design Incidence Angles at Design ϕ

Uncertainty of Data

To improve the precision of the experimental data, four separate readings were recorded at each survey location. Each data point was measured four times, then statistically analyzed to find the mean value of the four readings as well as the 90 percent confidence level using Student's t-distribution [26]. After analyzing all the data, the 90 percent confidence level calculations indicated that all the data was within ±1 percent of the calculated mean value. It is this mean value that is assumed to be the true and accurate reading. The mean value readings were then used in the data reduction procedure which yields the final velocity and pressure field.

APPENDIX C

DERIVATION OF ROTATIONAL EFFECTS CORRECTION OF SURFACE STATIC PRESSURE DATA

The manner in which the static pressures are obtained on the blade surfaces requires the added correction due to rotational effects. The surface pressures are obtained by allowing the surface pressure taps to bleed into a hollow chamber within the rotor blade. This chamber, which is really a piece of hypodermic tubing, transfers the pressure reading to the rotational axis where it is transmitted through a slip-ring unit to a differential pressure transducer. The mere fact that the column of air in the hollow chamber is being rotated produces additional pressure forces which if unaccounted for would lead to erroneous measurements.

The rotating column of fluid shown in Figure C1 represents an arbitrary piece of tubing from the instrumented rotor blades. The force on this column can be represented by the radial equilibrium equation:

$$\frac{1}{\rho}\frac{dP}{dR} = \frac{U^2}{R} \quad , \tag{C1}$$

where $U = \omega R$. The integration of Equation (C1) yields

$$\int_{P_1}^{P_2} dP = \rho \int_{R_1}^{R_2} \frac{U^2}{R}\, dR \tag{C2}$$

or

$$P_2 - P_1 = \frac{1}{2}\rho\,\omega^2\,(R_2^2 - R_1^2) \quad . \tag{C3}$$

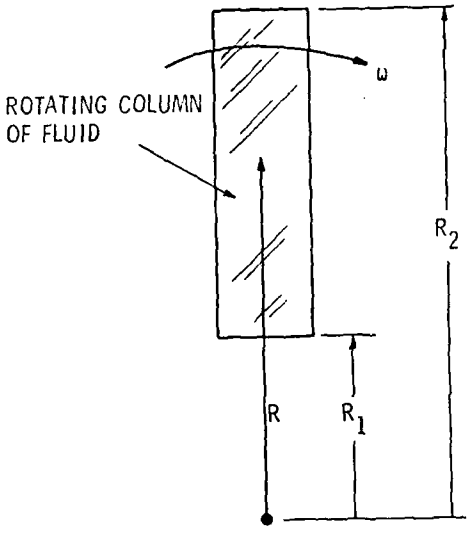

Figure C1. Rotating Column of Fluid

As long as the pressure tubing is transferred out of the rotating reference frame along the rotational axis, Equation (C3) can be reduced to the final form:

$$P_{ROTATION} = \frac{1}{2} \rho \omega^2 R_2^2 \quad . \tag{C4}$$

Since this pressure term due to rotation always acts to increase the absolute value of the measured static pressure, the true pressure is computed from

$$P_{TRUE} = P_{MEAS} - P_{ROTATION} \quad . \tag{C5}$$

For each radial location of static pressure taps, a pressure correction term is calculated and shown in Table 1C.

Table C1. Pressure Correction Terms for Surface Static Pressure Measurements

Radial Position (cm)	$P_{ROTATION}$ (psi)	$P_{ROTATION}$ (in. of H_2O)
23.2913	0.1285	3.557
19.5504	0.0905	2.505
15.8097	0.0592	1.639

DISTRIBUTION LIST FOR ARL UNCLASSIFIED TM 80-181 by M. J. Pierzga dated May 28, 1980.

Commander
Naval Sea Systems Command
Department of the Navy
Washington, DC 20362
Attn: Library
Code NSEA 09G32
(Copy Nos. 1 and 2)

Naval Sea Systems Command
Attn: Code NSEA 0342
(Copy Nos. 3 and 4)

Naval Sea Systems Command
Attn: T. E. Peirce
Code NSEA 63R3
(Copy No. 5)

Naval Sea Systems Command
Attn: A. R. Paladino
Code NSEA 05H1
(Copy No. 6)

Naval Sea Systems Command
Attn: F. Peterson
Code NSEA 52P
(Copy No. 7)

Defense Technical Information Center
5010 Duke Street
Cameron Station
Alexandria, VA 22314
(Copy Nos. 8 through 19)

Commanding Officer
Naval Underwater Systems Center
Newport, RI 02840
Attn: Library
Code 54
(Copy No. 20)

Commanding Officer
Naval Ocean Systems Center
San Diego, CA 92152
Attn: Library
(Copy No. 21)

Commanding Officer & Director
David W. Taylor Naval Ship R&D Center
Department of the Navy
Bethesda, MD 20084
Attn: W. B. Morgan
Code 15
(Copy No. 22)

David W. Taylor Naval Ship R&D Center
Attn: J. H. McCarthy
Code 154
(Copy No. 23)

David W. Taylor Naval Ship R&D Center
Attn: M. M. Sevik
Code 19
(Copy No. 24)

David W. Taylor Naval Ship R&D Center
Attn: W. K. Blake
Code 1942
(Copy No. 25)

David W. Taylor Naval Ship R&D Center
Attn: F. S. Archibald
Code 1942
(Copy No. 26)

Commanding Officer & Director
David W. Taylor Naval Ship R&D Center
Department of the Navy
Annapolis Laboratory
Annapolis, MD 21402
Attn: J. G. Stricker
Code 2721
(Copy No. 27)

David W. Taylor Naval Ship R&D Center
Attn: Y-F Wang
Code 2740
(Copy No. 28)

United Technologies Research Center
400 Main Street
East Hartford, CT 06108
Attn: Mr. Franklin O. Carta
(Copy No. 29)

Massachusetts Institute of Technology
77 Massachusetts Avenue
Cambridge, MA 02139
Attn: Dr. E. M. Greitzer
(Copy No. 30)

Stevens Institute of Technology
Department of Mechanical Engineering
Castle Point Station
Hoboken, NJ 07030
Attn: Professor F. Sisto
(Copy No. 31)

DISTRIBUTION LIST FOR ARL UNCLASSIFIED TM 80-181 by M. J. Pierzga dated May 28, 1980.

ONERA
Energie and Propulsion
29 Avenue de la Division Leclure
92 Chatillon sous Bagneux, France
Attn: Mr. J. Fabri
(Copy No. 32)

Virginia Polytechnic Institute and
State University
Mechanical Engineering Department
Blacksburg, VA 24601
Attn: Dr. Walter F. O'Brien, Jr.
(Copy No. 33)

Purdue University
School of Aeronautics and Astronautics
Chaffee Hall
West Lafayette, IN 47907
Attn: Dr. S. Fleeter
(Copy No. 34)

University of Salford
Salford, M5 4WT
ENGLAND
Attn: Dr. John H. Horlock
Vice Chancellor
(Copy No. 35)

Netherlands Ship Model Basin
P.O. Box 28
6700 AA Wageningen
THE NETHERLANDS
Attn: Dr. P. van Oossanen
(Copy No. 36)

Mut-Munchen Gmblt
8 Munchen 50
Postfach 50 06 40
GERMANY
Attn: Dr. Hans Mokelke
(Copy No. 37)

Forschungsbeauftrager für Hydroakustik
8012 Ottobrunn B Munchen
Waldparkstr. 41
Munich
GERMANY
Attn: Dr. rer. nat. Horst Aerbt
(Copy No. 38)

Admiralty Marine Technology Establishment
Teddington, Middlesex
ENGLAND
Attn: Dr. Allen Moore
(Copy No. 39)

Whittle Turbomachine Laboratory
Madingley Road
Cambridge
ENGLAND
Attn: Dr. D. S. Whitehead
(Copy No. 40)

Whittle Turbomachine Laboratory
Attn: Library
(Copy No. 41)

Von-Karman Institute for Fluid Dynamics
Turbomachinery Laboratory
Rhode-Saint-Genese
BELGUIM
Attn: Library
(Copy No. 42)

Turbine Research Department
Rolls Royce Ltd.
P.O. Box 31
Derby
ENGLAND
Attn: Dr. D. S. Thompson
(Copy No. 43)

NASA Lewis Research Center
21000 Brookpark Road
Cleveland, Ohio 44135
Attn: C. Ball
(Copy No. 44)

NASA Lewis Research Center
Attn: W. M. McNally
MS 5-9
(Copy No. 45)

Cranfield Institute of Technology
School of Mechanical Engineering
Cranfield, Bedford MK430AL
ENGLAND
Attn: Professor R. E. Peacock
(Copy No. 46)

DISTRIBUTION LIST FOR ARL UNCLASSIFIED TM 80-181 by M. J. Pierzga dated May 28, 1980.

Iowa State University
Mechanical Engineering Department
Ames, IA 50010
Attn: Dr. T. H. Okiishi
(Copy No. 47)

NASA Ames Research Center
Moffett Field, CA 94085
Attn: Dr. S. Bodapati
MA 227-9
(Copy No. 48)

Allis-Chalmers Corporation
Hydro-Turbine Division
Box 712
York, PA 17405
Attn: R. K. Fisher
(Copy No. 49)

NSW Institute of Technology
School of Mechanical Engineering
Broadway
Sidney
AUSTRALIA
Attn: Professor J. P. Gostelow
(Copy No. 50)

Naval Post Graduate School
Department of Aeronautics
Monterey, CA 93940
Attn: Dr. M. F. Platzer
(Copy No. 51)

Institute for Turbomachines
Technical University
Templergraben 55
D-5100 Aachen
Federal Republic of Germany
Attn: Dr. H. Gallus
(Copy No. 52)

HSVA Gmblt
Bramfelder Strasse 164
200 Hamburg 60
Postfach 600 929
Federal Republic of Germany
Attn: Dr. E. Weitendorf
(Copy No. 53)

J. M. Voith Gmblt
Hydraulic Department
Postfach 1940
D-7920 Heidenheim
Federal Republic of Germany
Attn: Mr. Eichler
(Copy No. 54)

HRA
7900 Inverness Ridge Road
Potomac, MD 20854
Attn: B. Cox
(Copy No. 55)

Applied Research Laboratory
The Pennsylvania State University
Post Office Box 30
State College, PA 16801
Attn: W. S. Gearhart
(Copy No. 56)

Applied Research Laboratory
Attn: M. W. McBride
(Copy No. 57)

Applied Research Laboratory
Attn: M. C. Brophy
(Copy No. 58)

Applied Research Laboratory
Attn: R. E. Henderson
(Copy No. 59)

Applied Research Laboratory
Attn: M. L. Billet
(Copy No. 60)

Applied Research Laboratory
Attn: B. L. Narayana
(Copy No. 61)


DAT
FILM